Photoactive Nanofibers Embedded with Lanthanide Nanoparticles for Wound Dressing

Ho Ying Huang

A Thesis
in
The Department
of
Biochemistry and Chemistry

Presented in Partial Fulfillment of the Requirements
for the Degree of Master of Science (Chemistry) at
Concordia University
Montreal, Quebec, Canada

May 2020

CONCORDIA UNIVERSITY
School of Graduate Studies

This is to certify that the thesis prepared

By: Ho Ying Huang

Entitled: Photoactive Nanofibers Doped with Lanthanide Ions for Wound Dressing

and submitted in partial fulfillment of the requirements for the degree of

Master of Science (Chemistry)

complies with the regulations of the University and meets the accepted standards with respect to originality and quality.
Signed by the final Examining Committee:

_____ Chair
Dr. Ashlee Howarth

_____ Examiner
Dr. Cameron Skinner

_____ Examiner
Dr. Rafik Naccache

_____ Supervisor
Dr. Louis Cuccia & Dr. John Oh

Approved by _____
Dr. Yves Gélinas

_____2020 _____
André Roy

Abstract

Photoactive Nanofibers Doped with Lanthanide Ions for Wound Dressing

Ho Ying Huang

Chronic wounds are difficult to treat, require frequent changing of dressings and are slow to heal. Inflammatory status persists in chronic wounds because they are associated with fluids that impair cell growth. Electrospun poly(vinyl alcohol) (PVA) fibers are proven effective at absorbing excess fluid from wounds. Appropriate drugs can also be embedded in such fibers for release into wounds *via* diffusion to accelerate wound healing. However, to better control the release of anti-inflammatory drugs into wounds, controlled drug delivery mechanisms are required.

The goal of this project is to use the unique properties of upconverting nanoparticles (UCNPs) to trigger drug release from electrospun fibers. These nanoparticles absorb near-infrared radiation and emit UV-radiation *via* an upconversion process. Since the UCNPs are born to have oleates on their surface, a variety of hydrophilic coatings have been screened to stabilize the UCNPs in an aqueous environment. Furthermore, our triggering mechanism relies on the sensitivity of *o*-nitrobenzyl (ONB) linkages towards the UV light emitted by the UCNPs. Poly(ethylene glycol) (PEG) was were conjugated through the photo-labile ONB molecules with levofloxacin, an antimicrobial drug whose release can be controlled *via* exposure of the UCNPs to infrared light. Preliminary drug release tests have shown that the drug conjugated ONB molecules can be cleaved by UV light and by the emission of UCNPs upon excitation with near-infrared light. The photo-labile conjugated drug (hvL-PEG) and UCNPs were embedded in electrospun and crosslinked PVA fibers as a model system for a wound healing dressing. The UCNP/hvL-PEG electrospun fibers show high antibacterial activity against the Gram-positive bacteria *Staphylococcus aureus* and Gram-negative bacteria *Escherichia coli*.

Acknowledgements

This project was supervised by Dr. Louis Cuccia, Dr. John Oh and Dr. Fiorenzo Vetrone. Committee members were Dr. Rafik Naccache and Dr. Cameron Skinner. I thank them all for their guidance throughout this project. The McGill Facility for Electron Microscopy Research (FEMR) is thanked for assistance with TEM images. Anti-bacterial tests were performed with the help of Dr. Brandon Findlay and his student Liana Zaroubi. My family is thanked for their love and emotional support. NSERC, the FQRNT-supported multiuniversity Québec Centre for Advanced Materials (QCAM) and Concordia University are thanked for their financial support during my M.Sc. studies.

I would like to thank Dr. Oh and Dr. Cuccia's lab members. They helped me when I had difficulties in synthesis and drug release studies. They are patient and experienced. Artiom Skripka from the Vetrone lab is an outstanding researcher who can solve any problem related to upconverting nanoparticles. He provided me with nanoparticles, characterized them and gave me insight on how to stabilize them in an aqueous environment.

Contribution of Authors

Most of the experiments were conducted by myself, except for synthesis of UCNPs and XRD analyses that were performed by Artiom Skripka. The antimicrobial tests were performed by Liana Zaroubi with the help of Dr. Brandon Findlay and the electrospinning setup was built with help from Dr. Cameron Skinner.

Table of Contents

Chapter 3 Methods

Chapter 4 Synthesis, drug delivery and antimicrobial evaluation of PVA fibers

Chapter 5 Conclusions and future possible directions

List of Figures

List of Tables

List of Schemes

List of Abbreviations

ATCC	American Type Culture Collection
API	Active Pharmaceutical Ingredient
ATRP	Atom Transfer Radical Polymerization
BHMT	Bis(hexamethylene)triamine
CLSI	Clinical & Laboratory Standards Institute
CRP	Controlled Radical Polymerization
DCM	Dichloromethane
DLS	Dynamic Light Scattering
DMAP	4-dimethylaminopyridine
DMF	Dimethylformamide
Dox	Doxorubicin
E. coli	*Escherichia coli*
EDC	1-Ethyl-3-(3-dimethylaminopropyl)carbodiimide
ESA	Excited-State Absorption
ETU	Energy-Transfer Upconversion
FITC-BSA	Fluorescein Isothiocyanate-Bovine Serum Albumin
GA	Glutaraldehyde
GO	Graphene Oxide
GPC	Gel Permeation Chromatography
HCl	Hydrochloric acid
HEMA	2-hydroxyethyl methacrylate
HMEC	Human Mammary Epithelial Cells
HPLC	High Performance Liquid Chromatography
hvL-PEG	Levofloxacin conjugated PEG-photocleavable molecules
LA	Lipoic acid
MDBC	Multidentate Block Copolymer
MHA	Mueller Hinton Agar
MHB	Mueller Hinton Broth
MIC	Minimum Inhibitory Concentration

MTA	[2-(methacryloyloxy)ethyl]trimethylammonium
MWCO	Molecular Weight Cut-Off
NIR	Near-Inrared
NMR	Nuclear Magnetic Resonance
NPs	Nanoparticles
OA	Oleic Acid
ODE	Octadecene
OEOMA	Oligo(ethylene oxide) monomethyl ether methacrylate
OM	Oleylamine
ONB	*O*-nitrobenzyl
PA	Photoavalanche
PBS	Phosphate Buffer Saline
PCL	Polycaprolactone
PCPA	Pentachlorophenyl acrylate
PEO	Poly(ethylene oxide)
PNIPAAm	Poly(N-isopropylacrylamide)
PLLA	Polylactic Acid
PMAO	Poly(maleic anhydride-alt-1-octadecene)
PVA	Poly(vinyl alcohol)
PVP	Poly(vinyl phenol)
RAFT	Reversible Addition-Fragmentation Chain Transfer
S. aureus	*Staphylococcus aureus*
SD	Standard Deviation
SEM	Scanning Electron Microscopy
TEM	Transmission Electron Microscopy
TGA	Thermogravimetric Analysis
UCNP	Upconverting Nanoparticles
UV	Ultra-Violet
XPS	X-Ray Photoelectron Spectroscopy
XRD	X-Ray Diffraction
XRPD	X-ray powder diffraction

ZOI	Zone of Inhibition
4VP	4-Vinyl Pyridine

Chapter 1 Introduction

1.1 Brief overview of research and goals

Chronic wounds have long been a concern in healthcare given their severity and slow healing nature. Millions of people suffer from non-healing chronic wounds as a result of bacterial infections, peripheral arterial disease, or diabetes, for example. Inflammation occurs within a day of ulcer formation, originating from enzymes secreted from inflammatory cells (*e.g.* macrophages, T-lymphocytes, fibroblasts), and results in redness, swelling and pain. Excess wound fluid can increase the risk of bacterial infections and impair cell growth.[1] Many wound dressings have been developed to address this clinical challenge, but methods for rapid healing that integrate the elements of drug delivery and wound fluid absorption are lacking for rapid healing.[2] Improving the treatment of chronic wounds can greatly reduce the associated healthcare costs and risks associated with infections.[3]

An ideal wound dressing should not only act as a physical barrier to prevent pathogens from entering the wound, but it should also be able to accelerate the healing process. Many kinds of wound dressings have been developed, including hydrogels,[4] films[5] and electrospun polymeric fibers.[6] Among these, electrospun fibers have great potential for wound dressing materials as they have better fluid uptake ability when compared to gauze that is commonly used.[7] At the same time, they can be easily produced in large scale at low cost. In fact, the use of electrospun nanofibers for wound dressings have been widely reported.[2, 8-10] Herein, polyvinyl alcohol (PVA) has been chosen for fabricating electrospun polymeric fibers due to its non-toxicity, biocompatibility and low cost.[11] The water solubility of PVA is a drawback for certain biomedical applications. However, reacting PVA fibers with glutaraldehyde is a common method for creating crosslinked fibers, which reduces the solubility of PVA fibers while still allowing them to swell and absorb excess wound fluid.[12]

1.2 Smart drug delivery systems

To address infections in chronic wounds, antimicrobial drugs can be incorporated into wound dressing fibers. Many compounds have been incorporated into polymeric fibers such as silver nanoparticles and antimicrobial drugs.[13] But simple incorporation cannot be used in controlled

drug delivery because the drug release occurs *via* diffusion only. In some cases, uncontrolled drug release can lead to overdose of the antimicrobial drugs.[14] Therefore, there is a need to generate controlled release of drugs in wound dressings. To control the drug release process, as a means to improve wound healing, stimuli-responsive materials can be introduced. For example, a stimuli-responsive material can be conjugated to drug molecules to be released by triggering with external stimuli.

Stimuli-responsive compounds have been widely used in drug delivery, where the stimuli are based on pH, temperature or light, for example.[15-16-17] Using light as the stimulus is often preferred, due to its non-invasive nature and ease of tuning the radiation power and exposure time. UV light is known to be the source for activating several photo-sensitive molecules including the o-nitrobenzyl (ONB) group, the azobenzene group and triphenylmethane.[18-21] Herein, the ONB functionality has been chosen because of the ease of conjugation and its stability under ambient light. The ONB group can be cleaved upon exposure to 365 nm UV irradiation.[22-23]

Trigging drug release in wound dressings with near-infrared (NIR) light is advantageous in comparison to UV light, since it has more penetration depth and exposure to UV light can be carcinogenic to living cells. As such, a means to convert infrared light to UV light is required. Upconverting nanoparticles (UCNPs) can convert NIR radiation to the UV, visible or IR region of the spectrum (anti-Stokes shift). It is based on the fact that lanthanide ions have a ladder-like energy level arrangement coupled with metastable excited states with long lifetimes. Depending on the types of lanthanide ions doped in the nanocrystals, f-f orbital transitions typically occur through mainly energy-transfer upconversion or excited-state absorption. These mechanisms involve the absorption of two or more lower energy photons by long-lived energy states. Upconversion can subsequently occur as a result of the increased population of higher energy states.[24]

1.3 Scope of my thesis

In this thesis, to achieve controlled drug release using NIR light, $LiYbF_4$: Tm^{3+}/$LiYF_4$ nanoparticles and drug conjugated ONB molecules were incorporated into electrospun PVA nanofibers. As a broad-spectrum antibiotic that has anti-microbial and anti-inflammatory properties, levofloxacin was chosen to be the model drug to incorporate into this system.

Levofloxacin is an FDA approved active pharmaceutical ingredient (API); at the same time, it can be detected easily by UV-vis spectroscopy. First, the as-synthesized ethyl 4-(4-hydroxyl-2-methoxy-5-nitrophenoxy)butanoic acid was covalently bonded to polyethylene glycol (PEG)-diamine by amide coupling to provide hydrophilicity. Levofloxacin was then covalently attached with the PEG conjugate to create a photo-sensitive prodrug (Figure 1).[22]

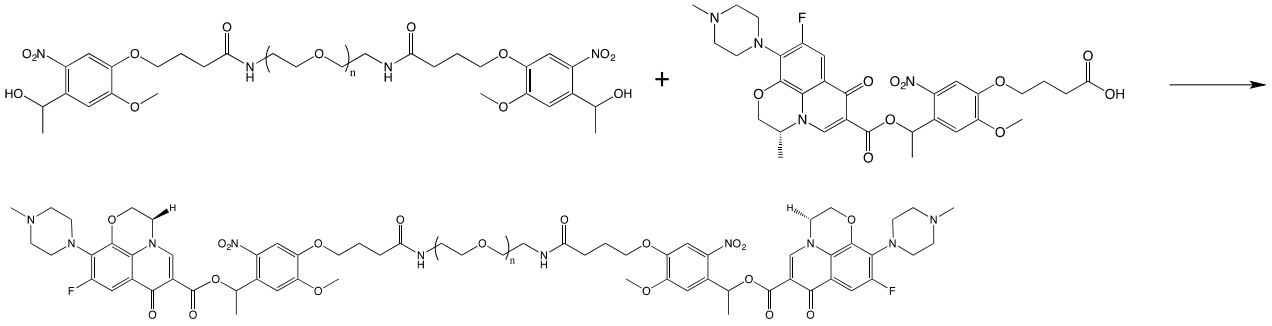

Figure 1. The reaction scheme to covalently attach levofloxacin to the PEG conjugate.[22]

UCNPs were synthesized and shelled *via* the thermal decomposition method. The drug conjugate and UCNPs were then embedded into the PVA nanofibers during electrospinning (Figure 2). Levofloxacin can be released gradually out of the fiber under NIR excitation at 980 nm, and the drug release behaviour and anti-microbial properties were investigated.

Chapter 2 Overview of wound dressing, electrospinning and upconversion

2.1 Wound dressing materials

Chronic non-healing wounds caused by different kinds of ulcers usually exhibit a delayed healing process. The microenvironment of a chronic wound is sophisticated and inflammatory status persists.[1, 25] To prevent infiltration of pathogens, originating from the external environment or surrounding skin, chronic wounds are treated with a broad variety of dressings. The simplest form, such as gauzes and bandages, can provide protection of the wound from bacterial infiltration while also allowing for gaseous and fluid exchange.[2] They can also be used as a support for more sophisticated 'smart' systems. Ideal wound dressings can prevent infections, improve healing progress, and ultimately restore the condition of the underlying healthy skin.

2.1.1 Traditional wound dressing materials

Sterile gauzes used for absorbing excess fluid in an open wound typically require frequent changing to protect against maceration of the skin surface.[3, 26] These dressings are less effective as they become moistened and adhere to the wound making it very painful during removal. Bandages made from natural cotton wool and cellulose perform different functions. Cotton bandages are used for small wounds, while high compression bandages and short stretch compression bandages give a certain level of pressure to venous ulcers.[27-28] Tulle dressings such as Bactigras™, Jelonet™, and Paratulle™ are suitable for superficial clean wounds. In general, these traditional dressings are for the clean and dry wounds with mild exudate levels.[29] Since traditional dressings often fail to provide a suitable environment for wound healing, they have been replaced by modern dressings with more advanced formulations.[2, 30] Modern wound dressings are able to prevent wound dehydration and are usually made of synthetic polymers.

Current wound dressing materials can be divided into four categories: passive, interactive, advanced and bioactive.[2] Passive dressings are dry and provide protection to wounds (e.g. gauze, lint and tulle). They have limited usage for more serious wounds. Also available are modified pads covered with a perforated plastic film to prevent the dressing from sticking to the wound (*e.g.* Band-Aid®).[31] Interactive dressings are fabricated with polymeric films which are permeable to

water and oxygen and can alter the wound environment to improve healing.[32] Advanced dressings are capable of providing a moist environment to improve wound healing processes.[3] Bioactive dressings are those capable of drug delivery which play an active role in the healing process.[33] Most recently, smart wound dressings have been developed that enable one to detect changes in a wounds environment (*e.g.* pH, temperature, oxygen, moisture and enzymes).[14, 34] These biomarkers allow the evaluation of wound status, the probability of infection or other abnormalities. Different types of dressings increase the effectiveness of therapies and improve patient comfort. However, there is always room to engineer more advanced platforms to improve wound healing.

2.1.2 Anti-microbial wound dressing materials

In view of preventing inflammatory responses in wounds, anti-microbial drugs or nanoparticles can be incorporated into wound dressing materials. Some organisms are naturally more resistant to antimicrobials; for example, gram-negative bacteria which have thin layers of peptidoglycan cell walls.[35] Therefore, different classes of antimicrobials with different modes of action are employed.

I. Incorporation of cationic NPs

Metals are known to have antimicrobial properties, with silver being the most powerful agent among all the metals.[35] For example, silver nanoparticle (AgNP)-based dressings are abundant.[36] AgNPs have been used for preparing ointments for burns, pressure ulcer wound dressings and medical devices to avoid infections. Under *in vivo* conditions, the acidic environment promotes the oxidation of AgNPs to Ag^+ ions. AgNPs themselves do not have any biological function but the generated Ag^+ ions are responsible for anti-bacterial activity by damaging bacterial cell walls.[36] One research group incorporated AgNPs into electrospun gelatin fiber mats for use in wound dressings.[37] The release of Ag^+ ions from crosslinked gelatin fibers increased abruptly during the first 60 mins and released more slowly afterwards. From the antimicrobial test, the sample fibers had the greatest activity towards *Pseudomonas aeruginosa*, followed by *Staphylococcus aureus*, *Escherichia coli*, and *methicillin-resistant S. aureus*. Another research group embedded silver nanoparticles in electrospun silk fibers using a simple dipping method.[38] This created yet another variety of wound dressing material with anti-microbial properties.

Due to their biocompatibility, gold nanoparticles (AuNPs) are widely used in tissue generation and wound healing. They are typically combined with other biomolecules for biomedical applications.[36] For example, a gold/chitosan film scaffold has been investigated which can improve the proliferation of newborn mice keratinocytes.[39] Their biological activity is maintained during rapid growth, which is attractive for wound dressings for skin tissue engineering. On the other hand, gold nanorods were covalently linked to primary antibodies to selectively destroy gram-negative bacterium – *Pseudonmonas aeruginosa*.[40] With the nanorod attaching to the bacteria cell surface, exposure to NIR resulted in a significant reduction in bacterial cell viability.

II. Incorporation of cationic polymers

Some polymeric materials can also be used for this purpose, for example, polymers embedded with antimicrobial agents that are released over time or polymers containing metal ions.[35] Most of these polymers are cationic and amphiphilic. Huang *et al.* developed bilayered antimicrobial nanofibers *via* electrospinning.[41] Quaternary ammonium salts ([2-(methacryloyloxy)ethyl]trimethylammonium, MTA) were polymerized and crosslinked in the presence of polycaprolactone (PCL) to fabricate a PCL/PMTA composite. The PCL inner layer was designed to be in direct contact with the wound, while the outer PCL-PMTA layer could defend against exogenous bacteria. The fibers showed strong antibacterial properties while being non-toxic to cells. Poly(vinylphenol) (PVP) can also be modified and electrospun.[42] The modification was performed on PVP by sulfonation with fuming sulfuric acid or *via* formation of the lithium salt of sulfonated PVP. They found that the antibacterial properties of their self-sterilizing material increased with increasing molecular weight. This demonstrates the property of being a self-sterilizing material. In another example, Qun *et al.* prepared block copolymers of 4-vinylpyridine (4VP) and pentachlorophenylacrylate (PCPA) by reversible addition-fragmentation chain transfer (RAFT) polymerization.[43] Quaternary ammonium salts were subsequently attached by N-alkylation of the pyridyl groups of P4VP and chloroaromatic compounds of the PCPA block. These self-quaternized fibers exhibited high antibacterial efficacy.

Besides the incorporation of cation-based small molecules into polymers, Guo *et al*. investigated the antibacterial activity of cationic polymers themselves.[44] Cationic polymers are attractive because of their relatively low toxicity and high antibacterial efficiency.[45-47] They

investigated side-chain polymers and main-chain polymers. For the results, all the small molecule cationic compounds, side-chain cationic polymers with relatively high molecular weight and main-chain cationic polymers showed effective inhibition of *E. coli* and *S. aureus*. For the side-chain cationic polymers, higher molecular weight polymers showed higher antibacterial activities. However, the antibacterial activities of main-chain cationic polymers were higher than those of the corresponding side-chain cationic polymers with similar or even higher molecular weight. Therefore, main-chain cationic polymers offer the greatest antibacterial properties among side-chain and small molecule cationic compounds while having low hemolytic activities. They clearly have potential applications in wound dressing materials.

2.2 Electrospinning

Versatile wound dressings that are able to protect chronic wounds while reducing the risk of bacterial infections are much sought after.[31] One of the principal research areas in wound care development are nanofibrous meshes, prepared *via* electrospinning.[48,8] These scaffolds are made of non-woven, ultra-fine electrospun fibers. Due to the random distribution of the small pores in the nanofiber mesh, the structure is similar to the extracellular matrix, which is the non-cellular component present within all tissues.[2] Nanofibrous meshes can act as a scaffold for physically supporting cells and can provide ideal conditions for cell attachment, proliferation and migration. Having a large surface area for wound fluid absorption is also crucial for enhanced drug delivery. Different chemical compositions of electrospun fibers can be applied under different conditions, while ideal fibers should have nanometer dimensions so as to prevent bacterial filtration.

2.2.1 Introduction to electrospinning

In its simplest form, the electrospinning process consists of a syringe primed with the polymer solution, a syringe pump, two electrodes, one being the syringe tip, and a DC voltage supply (15-30kV) (Figure 2).[49] The polymer solution is electrospun into a fiber due to the high voltage, causing the extruded polymer jet to charge electrically, bending the polymeric fiber as it moves towards and is collected at the grounded target. The more the polymeric fibers 'spin', the thinner the fibers become.[49]

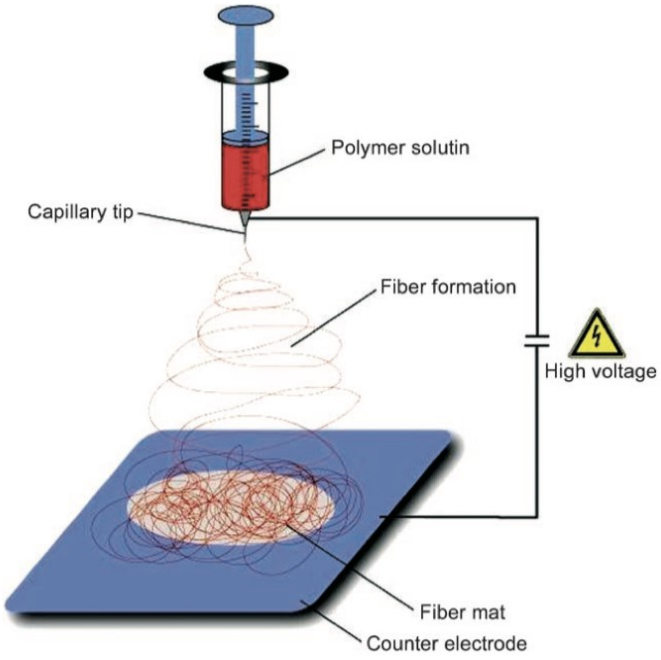

Figure 2. A schematic diagram of the electrospinning process.[49]

2.2.2 Effect of solution parameters

I. Concentration

If the solution concentration is very low, the viscosity decreases and the surface tension increases. In this case, the solution will 'electrospray' rather than 'electrospin'. As the concentration increases, beads and fibers will form simultaneously until a critical concentration is achieved. In this ideal concentration range, uniform fibers can form. If the concentration is too high, electrospinning will not occur and sometimes helix-shaped micro-ribbons will be observed. In general, the diameter of the electrospun fibers increases as the polymer solution concentration increases (Figure 3).[50]

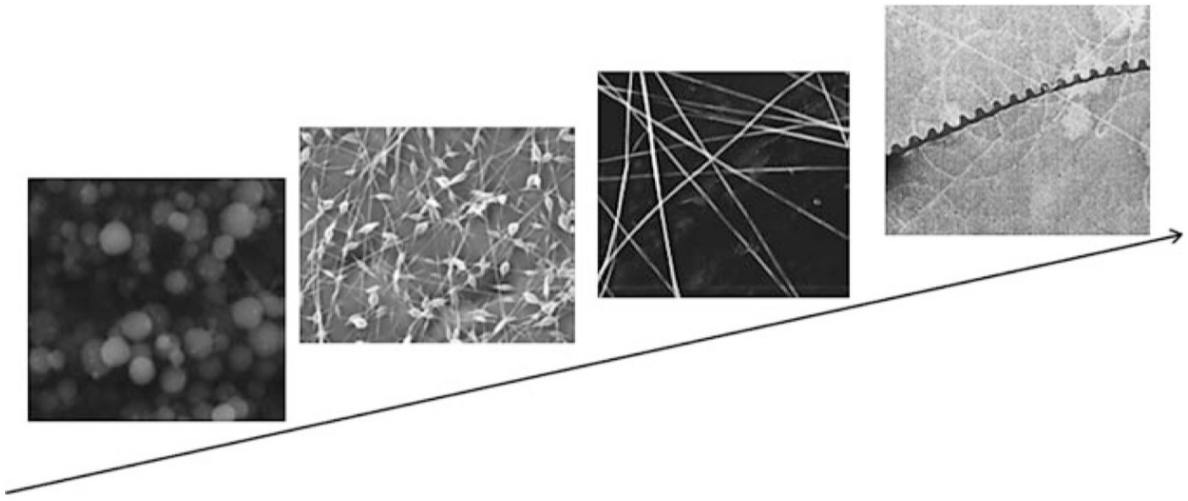

Figure 3. SEM images of the electrospinning products of poly(ethylene oxide) (PEO) ranging from low to high solution concentration (0.01 – 0.045 g/mL).[50]

II. Molecular weight

Molecular weight controls the entanglement of polymer chains in solution, which relates to the solution viscosity. Lowering molecular weight tends to favor the formation of beads rather than fibers, while increasing molecular weight is more amenable to the formation of smooth uniform fibers. If the molecular weight is too high, micro-ribbons can be obtained. Sometimes molecular weight is not as important, especially if intermolecular interactions are sufficiently strong. [50]

III. Viscosity

Solutions with very low viscosities cannot be used to produce smooth electrospun fibers, while solutions with very high viscosities are difficult to eject. Fortunately, the viscosity can be tuned by adjusting the polymer concentration, molecular weight and/or concentration.[50]

IV. Surface tension

Yang *et al.* reported the dependence of surface tension on the morphology of electrospun polyvinylpyrrolidone fibers with solvents having different surface tensions.[51] Beaded fibers can be turned into smooth fibers by changing the mass ratio of solvents.

V. Conductivity

Conductivity is determined by type of polymer, solvent and salt additive used. In general, natural polymers are polyelectrolytic, which means the amount of charge that can be accommodated by the polymer jet increases, which leads to smooth fiber formation. Electrical conductivity can be controlled with salts or organic acids in order to control fiber diameter. All in all, increasing conductivity tends to result in the formation of thinner fibers.[52]

2.2.3 Effect of working parameters

I. Voltage

Applied voltage is a crucial factor for the electrospinning process to go smoothly, where high voltages will induce charges in the solution. As a result of this external electric field, the electrospinning will occur once the electrostatic force overcomes the surface tension of the solution. When the voltage is higher than a threshold voltage that is required to stretch the polymeric solution to become charged jets, a Taylor cone will form, and the jets eject to deposit fibers on the collector plate.[49]

II. Feed rate

There is a suitable feed rate for a stable Taylor cone to be formed at a constant voltage. In general, lower solution flow rates are recommended because the polymer solution has a longer time for polarization. If a high flow rate is used, large diameter beads can form due to insufficient time for the fiber to dry prior to reaching the collector.[53]

III. Collectors

The collectors are usually grounded conducting materials (*e.g.* aluminium foil) to allow for the deposition of charged fibers. Other kinds of collectors have been developed, and include wire mesh, grids and rotating rods.[53]

IV. Distance between the collector plate and syringe tip

If the distance between the collector plate and syringe tip is too small, the fiber will not have enough time to dry and solidify before reaching the collector. On the other hand, distances that are too long can lead to beaded fibers. An optimal distance can help to create thin uniform fibers.[53]

V. Humidity

Mituppatham *et al.* have shown that thinner fibers can be formed at higher temperatures as this favors solvent evaporation and reduces solution viscosity.[54] With a lower viscosity, the columbic forces impart a larger stretching force to the solution resulting in thinner fibers. Low humidity can increase the rate of solvent evaporation and help to dry the fibers thoroughly. In contrast, high humidity can lead to thick fibers because the charge on the jet tends towards being neutralized and the stretching force diminishes.[53]

2.2.4 Electrospinning and drug delivery

Various delivery systems have been investigated to improve therapeutic processes.[55] Electrospinning has been recognized as a simple and versatile method to produce polymeric nanofibers for drug delivery. For example, PVA/Chitosan composite nanofibers loaded with the sodium salt of ampicillin was produced by electrospinning.[9] The PVA/Chitosan composite nanofibers were crosslinked with glutaraldehyde (GA). Drug release studies revealed that this crosslinked network structure could effectively reduce the drug release rate and the burst effect of ampicillin from PVA/Chitosan composite nanofibers. The incorporation of antibiotics into electrospun membranes based on chitosan, PVA and graphene oxide (GO) have also been reported.[56] The antibiotic ciprofloxacin was effectively loaded into composite nanofibers, where incorporation of the drug in GO nanosheets prevents the initial burst release of antibiotic, while still demonstrating significant antibacterial activity. In another example, cerium oxide nanoparticles (CeO_2 NPs) can be incorporated into electrospun poly(3-hydroxybutyrate-co-3-hydroxyvalerate) membranes, which induced cell proliferation, angiogenesis and wound healing.[57] The human mammary epithelial cells (HMEC) adhered to fibers, while blood vessel formation was enhanced in response to CeO_2 NPs. Yuan *et al.* investigated the functionalization of doxorubicin (DOX) loaded polylactic acid (PLLA) nanofibers using polydopamine.[58] In this case, an implantable patch was used for breast cancer therapy. *In vivo* studies were performed in mice, and cancer cell dysfunction was observed in PLLA-DOX fiber treated groups. On the other hand, poly(N-isopropylacrylamide) (PNIPAAm) nanofibers were fabricated by Salehi *et al.* for temperature responsive delivery of DOX.[59] Here, the researchers crosslinked PNIPAAm with

hydrophobic polymers so that the fibers would not be soluble in water. Excellent encapsulation of drug was demonstrated by observing sustained drug release for over 30 days.

2.3 Potential of poly(vinyl alcohol)

I. Types of polymers used for electrospinning

Different polymers have been used for electrospinning (Scheme 1).[60] Nylon 6,6 can be electrospun into a very fine membrane mat with extremely small pore sizes that are much smaller than the average fiber diameter.[61] These mats can be used in protective coatings. An example of electrospun polylactic acid was reported by Caruso *et al.*[62] The sol gel coating of poly(L-lactide) fibers by electrospinning has been used to make hollow metal-oxide fibers. The coating technique results in thin walled, less than 200 nm tubes with diameters ranging from hundreds of nanometers to a few micrometers.

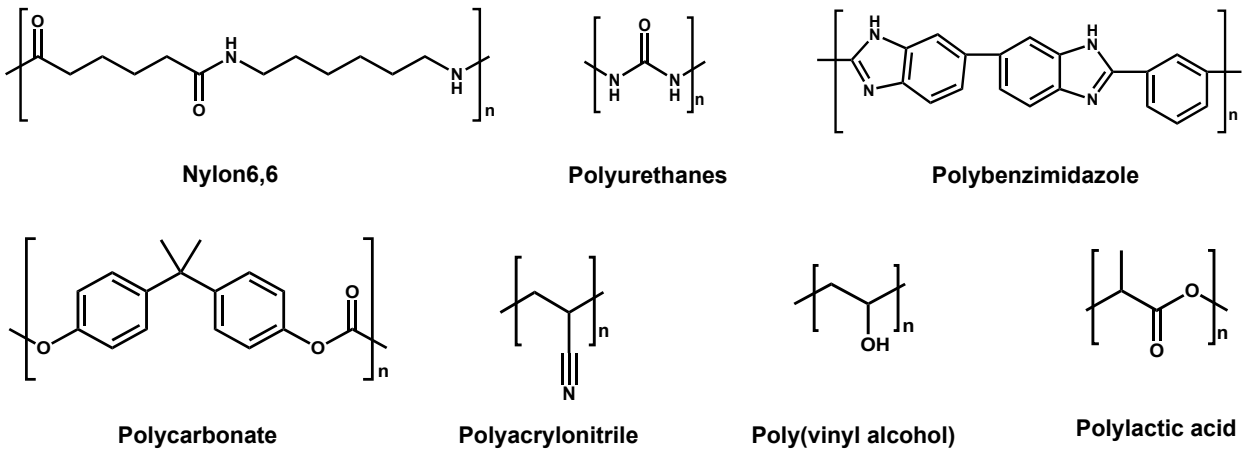

Scheme 1. Examples of polymers that have been used in electrospinning.[60]

II. Characteristics of PVA fibers as wound dressing materials

PVA is one of the most frequently used synthetic polymers employed in wound dressing materials[56], drug delivery systems[63], artificial organs[64], and contact lenses.[65] It is nontoxic, non-carcinogenic, biocompatible and has a high degree of swelling in aqueous solutions.[66] Novel carboxyl-modified PVA-crosslinked chitosan hydrogel films have been created for wound dressing materials.[67] The swelling ratio was greatly improved such that the films can maintain a moist environment over the wound. Furthermore, they showed no cytotoxicity or hemolytic

potential. Gentamicin sulfate-loaded crosslinked hydrogel films showed sustained drug release over time to suppress bacterial proliferation. Another group used chitosan derivatives with quaternary ammonium groups to supress the growth of bacteria and fungi.[68] In this case, the chitosan derivatives were mixed with PVA and crosslinked by incorporation of photo-crosslinking additives with UV irradiation. The fibers showed high antibacterial activity against both gram-positive and gram-negative bacteria. PVA can also be used to produce hydrogels. PVA and carboxymethylated chitosan were made into hydrogels by electron beam irradiation at room temperature. The hydrogels were active against *E. coli* even when the concentration of carboxymethylated chitosan was only 3%. These results strongly support the potential of PVA as an attractive candidate for wound dressing materials.

.

2.4 Overview of stimuli-responsive degradation platforms

Different stimuli can be used for triggering drug release in wound dressing materials and they are associated with their own advantages and limitations (Table 1).[69]

Table 1. Advantages and limitations of different kinds of stimuli for drug delivery.[69]

Stimulus	Advantage(s)	Limitation(s)
Biomarker	High target specificity	Stability, potential leakage and possible immunogenicity of enzymes or antibodies used in the delivery system
pH	Small changes in pH can result in significant chemical and physical changes in drug carrier	Limited to the clinical conditions that alter local pH
Heat	Cancer cells are sensitive to hyperthermia (i.e., apoptosis, increased sensitivity to radiation and chemotherapeutics) Thermally responsive drug-delivery systems are in clinical trials	Risk of superficial tissue damage from external heating source needed for deep tissue penetration (attenuation of stimulus)
Light	Ability to sequentially trigger multiple payloads High degree of spatiotemporal precision	Questionable safety and/or biodegradability of materials Safety risks and low tissue penetration for UV-Vis light

Comparing the pros and cons in Table 1, light is a most suitable stimulus as it allows for precise temporal and spatial control. Light is non-invasive,[70] it has high spatial resolution and temporal control[69] and is easy to implement. Because of this, light has been widely utilized in the biomedical field, including photochemically triggered release, photoisomerization and photothermal release. Photochemical triggering involves covalent bond cleavage initiated by light irradiation, where the encapsulated drug can be released as a result of bond cleavage.[69] The ONB moiety can be cleaved irreversibly by UV light to release free carboxylic acid and *o*-nitrosobenzaldehyde.[71] Coumarin-[72] and pyrene-[73] derivatives are also commonly used for UV-activated photocleavage reactions (Figure 4).[73]

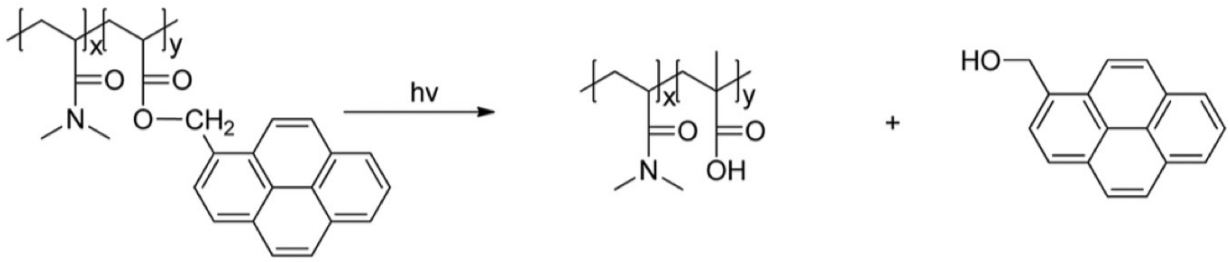

Figure 4. Illustration of the photolysis of a pyrene-linked copolymer.[73]

UV and high-energy visible light are often used for breaking covalent bonds as they have high energy. Photoisomerization involves reversible conformational changes within a molecule induced by light. Azobenzenes are popular for photoisomerization reactions, where the two phenyl groups linked by an N=N bond enables the transition from *trans* to *cis* with UV irradiation and from *cis* to *trans* with blue irradiation.[74] Drug release can be triggered when the molecule changes to *cis* form. With blue irradiation, the molecule reverts back into the *trans* form, which closes the opening and the drugs are once again trapped (Figure 5). In the end, drug release can be turned on and off by using different wavelengths of light so that on-site drug delivery is achieved.[75]

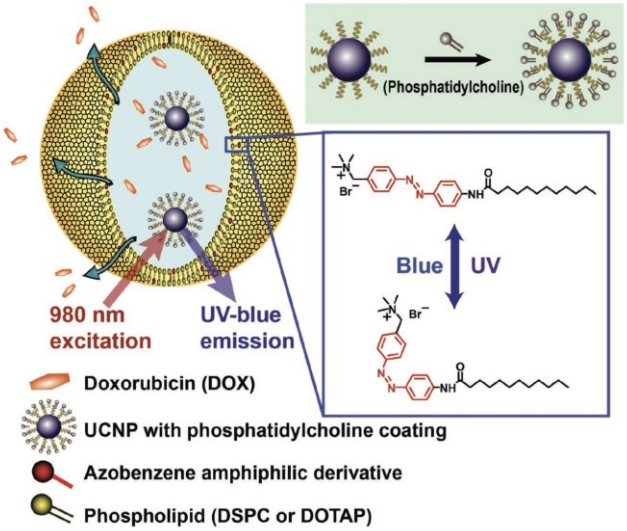

Figure 5. Schematic illustration of NIR-triggered azobenzene-liposome/upconverting nanoparticle hybrid vesicles for controlled drug delivery.[75]

Photothermal systems involve the irradiation of light on heat-generating elements and the heat can be transferred to local heat sensitive components in order to achieve drug delivery. A full system includes a chromophore that is able to convert light energy into heat and a thermal-responsive material that responds to temperature change in a specific fashion. Gold nanoparticles are inert and generally non-toxic, depending on their morphologies.[76] They have tailorable properties including the absorption of NIR irradiation.[77] Poly(N-isopropylacrylamide-acrylamide-vinylpyrrolidone) (PNIPAAm) is widely used for thermal triggered release systems as it undergoes a reversible temperature-induced change in hydrophobicity at its lower critical solution temperature.[59] PNIPAAm was electrospun to prepare stimuli-responsive nanofibers loaded with doxorubicin. The nanofibers are promising materials for cancer treatment and offer the potential of smart drug delivery due to their large surface area and porosity.

2.4.1 *O*-nitrobenzyl molecules and their applications

Photocleavable units are prominent in organic synthesis and have found many applications in biomedicine. The ONB moiety is one of the most used photolabile protecting groups among all the photolabile units that have been studied.[23] The mechanism has been investigated in detail and

involves intramolecular H-atom transfer affording *aci*-nitro (nitronic acid) tautomers that are readily detected by their strong absorption at *ca.* 400 nm (Figure 6).[71] The photo-deprotection of the ONB moiety produces *o*-nitrosobenzaldehyde and free carboxylic acids.

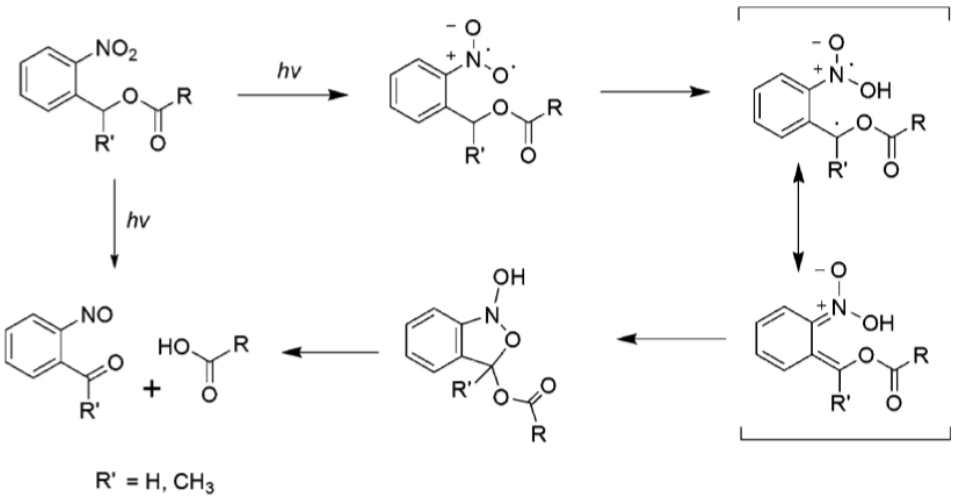

Figure 6. Photoisomerization mechanism of ONB alcohol derivatives.[71]

One example of hydrogels for live cell encapsulation and release using the ONB group was reported in 2012.[78] In this case, photodegradation allowed for external real-time control over the degradation of hydrogels with concomitant cell release. In another example, ONB linked methotrexate was covalently conjugated with a poly(amidoamine) dendrimer carrier for a drug release study.[79] Using UV/vis spectroscopy, ^{1}H-NMR spectrometry, and analytical HPLC, the authors showed that the photochemical mechanism is active under neutral and acidic conditions. Several factors, including wavelength, exposure time, substitution pattern of the ONB group and pH of the media, were shown to affect drug release kinetics. Light-activated approaches are suitable for many types of anticancer drugs and therapeutic and diagnostic applications that require non-invasive activation.

2.5 Upconverting Nanoparticles

The discovery of the lanthanides has to date back to the 18th century. Their unique properties originate from their 4f orbitals that possess effective spin-orbit coupling and shielding of 4f orbitals

by 5s and 5p shells. [80, 81, 82] The magnetic moments, susceptibilities, and electronic relaxation times of lanthanides are determined by their 4f electronic configurations.[81]

2.5.1 Introduction to upconverting nanoparticles

Upconversion refers to the process whereby two or more lower energy photons are absorbed, leading to the emission of a photon of higher energy. This kind of anti-Stokes emission is a nonlinear optical process, meaning that the intensity of incident light can affect the optical properties of the nanoparticles. The upconversion process is achieved by several mechanisms, namely: (*i*) Energy-Transfer Upconversion (ETU), (*ii*) Excited-State Absorption (ESA) and (*iii*) Photon Avalanche (PA).[24] In ETU, successive energies are transferred from singly excited ions, which refers to the sensitizers, to activator ions which give emissions. To further explain, the excitation of the activator ions will be followed by sequential excitation from sensitizers until the final emission state. At least two ions need to be involved in ETU. In ESA, at least two photons are absorbed by the ion and this leads to the population of a higher excited state (Figure 7).[24] It is possible only when an electron has already been excited to a excited state. ESA is more likely to be observed for ions with multiple electronic levels, e.g. Er^{3+} and Tm^{3+}, whereas it is impossible in Yb^{3+}. In PA, the incident photon energy is only resonant to higher excited states but not the ground state. PA requires a threshold energy that is strong enough to populate the higher excited states.[84] For example, a $LaCl_3$ crystal doped with Pr^{3+} was exposed to a continuous wave laser pump radiation which its frequency matches the ESA transition, $^3H_5 \rightarrow {}^3P_1$. When this radiation was slightly higher than the threshold energy, fluorescence originating from $^3P_1 \rightarrow {}^3P_0$ relaxation increased by orders of magnitude.[84]

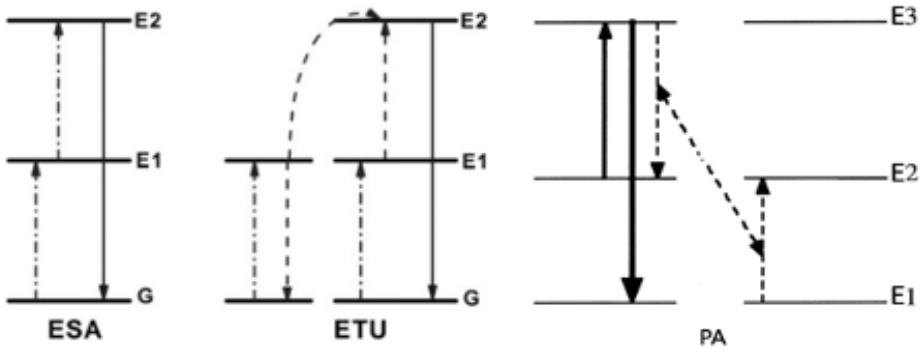

Figure 7. Processes that generate upconversion emission: excited-state absorption (ESA), energy-transfer upconversion (ETU) and photo avalanche (PA).[24]

To achieve upconversion, the ions need to have metastable excited states with long lifetimes and a ladder-like arrangement of the energy levels with similar spacings. A common efficient upconversion phosphor is $NaYF_4$ doped with Yb^{3+} and Er^{3+}.[85] Due to their outstanding properties, they are used in many different applications, such as solar cells, for displays and optical devices.[81] As compared to other luminescent particles and organic dyes, lanthanide nanoparticles are resistant to photobleaching, photo-blinking and autofluorescence from organisms.[85] Using near infrared excitation allows deep penetration into tissue which makes UCNPs better candidates for biological applications.

2.5.2 Mechanism of upconverting nanoparticles synthesis

I. Nucleation

In the 1940s, LaMer and coworkers implemented the concept of 'burst of nucleation' during the synthesis of aerosols and hydrosols.[86] In this case, many nuclei are generated at the same time and proceed to grow without any additional nucleation. This feature makes it possible to control the size distribution of crystals during synthesis. If not, the nanocrystals differ vastly in size due to continuous nucleation. Therefore, it is of utmost importance to induce only one burst of nucleation events during synthesis and to inhibit additional nucleation events. In essence, this method separates nucleation and growth. In homogenous nucleation, nuclei appear without any pre-introduced seed nuclei, where the energy barrier to form a nucleus is very high since the system needs to spontaneously change from a homogenous to a heterogenous phase. To visualize the energy barrier for 'burst of nucleation', the LaMer plot is constructed as shown in Figure 8.[84] In stage I, the concentration of the monomer increases with time gradually. In stage II, when the degree of supersaturation is high enough to overcome the energy barrier, stable nuclei will accumulate and form. The concentration of monomer decreases because the rate of consumption is higher than the rate of supply. It will eventually reach a level at which the number of nuclei formed per unit time is zero. The system subsequently enters stage III. At this stage no more nucleation occurs and the crystals continue to grow until the solution is no longer supersaturated. Finally, the system enters stage IV, Ostwald ripening. Sacrificial dissolution of smaller higher surface energy particles occurs allowing for the growth of more stable larger particles.

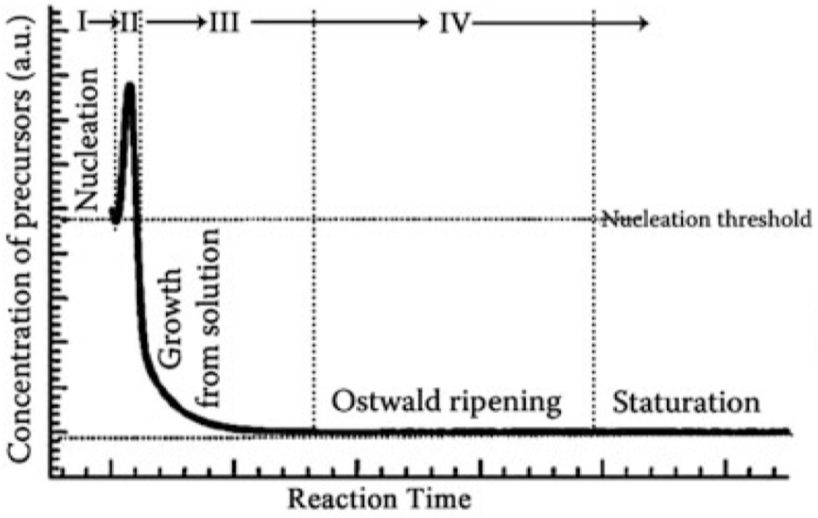

Figure 8. LaMer plot showing the relationship between precursor concentrations and reaction time.[84]

II. Growth

Talapin *et al.* propose two underlying mechanisms for the size distribution behavior when there is no additional nucleation during the growth process: (*i*) The "focusing" effect is a kinetically driven process which continuously reduces the variance of the particle size.[87] It works when the growth process is diffusion controlled and there is a high degree of supersaturation. (*ii*) Ostwald ripening occurs when the degree of supersaturation is low. Alivisatos and coworkers reported that the degree of supersaturation is inextricably related to the size distribution of the nanocrystals.[88] They observed that during the initial period of the growth process in the hot-injection method (Figure 9), average particle sizes increase rapidly, and the size distribution narrows simultaneously. After this stage, the growth rate decreases, and the size distribution broadens. This result illustrates the relationship between the degree of supersaturation and the size focusing by growth, which supports the "focusing" mechanism.

2.5.3 Typical Synthetic Process

I. Thermolysis

Organometallic compounds (*e.g.* metallic trifluoroacetate salts) act as precursors which decompose at high temperature in high boiling point solvents and surfactants.[84] Oleic acid (OA),

oleylamine and 1-octadecene (ODE) are common surfactants which contain functional groups able to coordinate to the nanoparticle surface. They have a long carbon chains to prevent the nanocrystals from aggregating. Varying the concentration of metal precursors, reaction time, temperature and the composition of solvent can lead to nanocrystals with different crystallinity, size distribution and optical properties. It is also important to note that thermolysis can produce toxic fluorinated and oxyfluorinated byproduct, as such, thermolysis should be carried out in a well-ventilated hood.

In the one-pot hot-injection method, the precursors are mixed at a low temperature and brought to a very high temperature where the decomposition of precursors occurs quickly to achieve supersaturation.[84] Supersaturation leads to a burst nucleation event, then the temperature is kept constant to prevent more nucleation. Monomers are subsequently added to the active nuclei resulting in a monodisperse population of uniform nanoparticles.[24, 84] For the synthesis of core/shell nanoparticles, the precursors are metal trifluoroacetate. They are dissolved in OA/ODE and injected into the solution of core nanoparticles under high temperatures (Figure 9).[89]

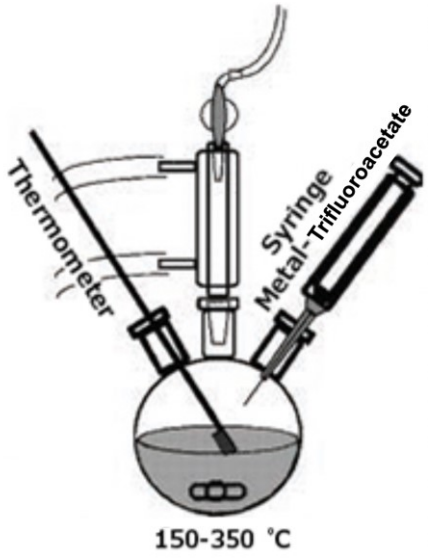

Figure 9. Schematic illustration of nanoparticle synthesis.[89]

II. Hydrothermal Synthesis

Hydrothermal refers to any heterogeneous reaction in the presence of solvents under high temperature and pressure to dissolve and recrystallize materials that are originally insoluble under normal conditions.[85] Polyethylenimine, ethylenediaminetetraacetic acid and OA are suitable surfactants to control the size, morphology and crystalline phase. The metallic precursors, solvents and surfactants are mixed and heated in an autoclave which provides high temperature and pressure for the prolonged reaction.

2.5.4 Selection of dopants and host lattice

The upconverting nanoparticles consist of optically transparent and chemically stable crystalline host and optically active dopants. The distance between the dopants is very important, as it determines energy transfer dynamics among ions, which affects luminescence color and intensity to maximize luminescence intensity. Highly efficient upconversion requires optimization of the host lattice, dopant ions and their concentration.[24]

I. Choice of Host Lattice

The host lattice determines the distance between dopant ions, their relative spatial separation, their coordination numbers and the type of anions surrounding the dopant. In the ETU mechanism, for $NaYF_4$:Yb^{3+}, Er^{3+} nanoparticles, Er^{3+} is excited into the $^4F_{7/2}$ state in two steps by Yb^{3+}, which is the ion that absorbs NIR radiation (Figure 10).[24] The $^2H_{11/2}$ state and the $^4S_{3/2}$ state are populated by nonradiative multiphonon relaxation steps. The ion may return to the $^4I_{15/2}$ state or populate the $^4F_{9/2}$ state by an additional nonradiative multiphonon relaxation steps. Fluoride crystals are preferred due to the low phonon energies of the crystal lattice which benefits (*i.e.* populates) the long $^4I_{11/2}$ lifetime and finally intense upconversion is achieved. Metal oxides, on the other hand, have high chemical stability but the phonon energies are high.

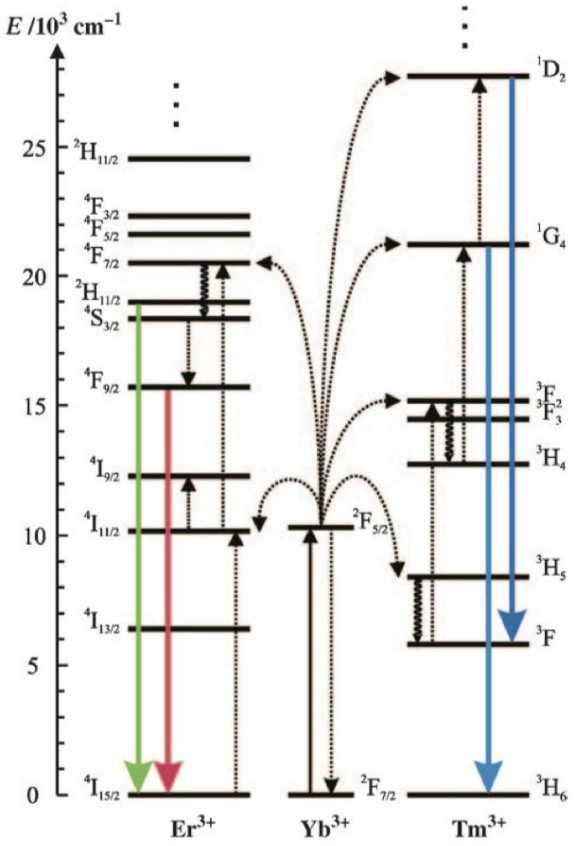

Figure 10. Energy-level diagram, upconversion excitation and visible emission of Yb^{3+} sensitized Er^{3+} and Tm^{3+}. Arrows indicate radiative and nonradiative energy transfer and multi-phonon relaxation processes.[24]

Li^{+} ions are commonly introduced in the upconverting nanoparticles due to their small ionic radius, the mismatch of ionic radius with lanthanide ions creates lattice stress. Lattice stress is actually preferred for increasing emission intensity because it helps 4f intermixing with higher orbitals and increases the probability for f-f transitions.[90] The hexagonal crystal polymorphs have ten times higher upconversion efficiencies when compared to their cubic counterparts.[91] The high luminescence emission is due to the lower symmetry which allows f-f transitions.[24]

II. Single Dopant

For Er^{3+}, Tm^{3+} and Ho^{3+}, the gaps between energy levels are very similar. Sequential excitations to a high energy level are possible using a monochromatic light source.[90] Increasing the dopant concentration can enhance the absorption, but non-radiative deactivation and cross-relaxation limits the dopant concentration, unless more sophisticated core-shell strategies are

involved in upconverting nanoparticles' engineering.[92] The concentration limit depends on the exact distance between the lanthanide ions and the type of ions. In general, Er^{3+} doping does not exceed 3% and Tm^{3+} doping does not exceed 0.5%.[24] These concentrations are not optimal for light absorption, therefore, the crystals are sometimes co-doped with strong absorbing ions called sensitizers.

III. Codoping

The most common sensitizer for Er^{3+} and Tm^{3+} is Yb^{3+}. The energy state separations of Yb^{3+} are very similar to that of Er^{3+} which allows an efficient energy transfer process between the two ions. Yb^{3+} is often codoped in the lattice at high concentrations. Yb^{3+} can also attain efficient energy transfer with Tm^{3+}. The energy of 980 nm photons from Yb^{3+}, ranging from one to five photons, are transferred to one Tm^{3+} ion. Depending on the number of photons transferred, the upconversion emission will be different. These two couples show the highest efficiency when doped into the hexagonal phase of $NaYF_4$. Yb^{3+} can also be co-doped with Ho^{3+} and Pr^{3+} ions.[24]

2.5.5 The Core-Shell Strategy

Due to the use of surfactants during the synthetic process, the nanoparticles bear oleic acid coating.[93] The OH groups have high energy vibrational modes which can lead to quenching *via* multiphonon relaxation processes. Shelling can be carried out to reduce energy loss at the nanoparticle surface. An ideal shell should prevent energy transfer from the core to the outer surface.

I. Passive Shelling

The most straightforward shell material is the pure, undoped host material of the core lattice. Using the same material from the core crystal gives no lattice mismatch and therefore is the best choice. The successful deposition of the undoped material on the core surface can be deduced from an increase in average particle size determined by TEM together with an increase in luminescence efficiency.[24]

II. Active Shelling

Other than optically inactive shells, optically active shells can also be used to achieve different outcomes such as increased luminescence and tuning the upconversion fluorescence. For example, J. Zhang *et al.* reported hexagonal $NaYF_4:Yb^{3+}$, Tm^{3+}/β-$NaYF_4:Yb^{3+}$, Er^{3+} (core-shell AB) and $NaYF_4:Yb^{3+}$, Tm^{3+}/β-$NaYF_4:Yb^{3+}$, $Er^{3+}/NaYF_4:Yb^{3+}$, Tm^{3+} (core-shell-shell ABA) nanocrystals (Figure 11).[94]

Figure 11. The core-shell-shell ABA strategy.[94]

Core-shell-shell ABA nanocrystals show a great enhancement of Er^{3+} fluorescence (Figure 12) and can achieve multi-color fluorescence which displays no quenching of the Tm^{3+} emission.[94]

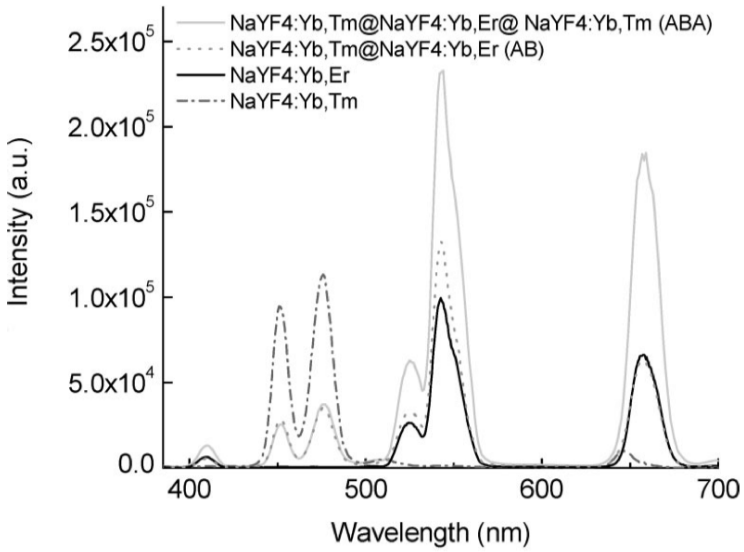

Figure 12. Fluorescence spectra of core-shell $NaYF_4:Yb,Tm@NaYF_4$: $Yb,Er@NaYF_4:Yb,Tm$ (ABA), $NaYF_4:Yb,Tm@NaYF_4$:Yb,Er (AB), $NaYF_4:Yb,Er$, and NaYF4:Yb,Tm nanocrystals.[94]

III. Silica Shelling

Shelling amorphous silica on the nanoparticle surface can be achieved by Stöber type reactions, based on the hydrolysis of tetra-alkoxy silanes. Silica shells are chemically inert and offer an ideal platform for subsequent attachment of different functional groups on the surface, especially useful for the conjugation of biomolecules.

2.5.6 Organic coatings for upconverting nanoparticles

Surface ligands can affect the colloidal stability of UCNPs, especially when switching from an organic to an aqueous environment. Modification relies on deposition of additional layer coatings or ligand exchange, as discussed below.

Deposition of the amphiphilic layer retains the initial oleic acid layer on the surface of UCNPs. In other words, the oleic acid layer has been shelled to allow dispersion in an aqueous environment. Examples include poly(isobutylene-alt-maleic anhydride)[95], silica[96] and 1,2-distearoyl-sn-glycero-3-phospho-ethanolamine-N-[methoxy(poly-ethylene glycol)-2000] (ammonium salt)[97]. The ligand interaction is driven by van der Waals interactions between the hydrophobic alkyl chains of the oleic acid and the amphiphilic ligands.

Ligand exchange involves the complete exchange of the initial oleic acid ligands by hydrophilic ligands.[97] Examples include citrate[98] and $NOBF_4$.[99] A complete exchange can be ensured by higher temperatures, excess of the new ligands and a suitable solvent.[100] The choice of solvent depends on the dynamic solvability of the hydrophobic and the new surface ligand. For example, multidentate ligands are preferred over monodentate ligands and carboxylate groups are preferred over amines due to a higher coordination ability.[100] This technique is based on pH changes and renders water dispersible UCNPs due to the positively charged nanoparticle surface.[101-102]

2.5.7 Upconverting nanoparticle-based drug delivery systems

UCNPs are very versatile due to their NIR-excitation nature, which can then be used in drug delivery for high tissue penetration depth. Xiang *et al.* reported a new approach to encapsulate

charged cargo molecules into a nanocarrier constructed with negatively charged UCNP@silica and positively charged UV-labile polyelectrolyte bearing pendants of poly(ethylene glycol) and ONB moieties through electrostatic interaction-driven complexation.[103] Another study is that charged fluorescein, a drug surrogate, was loaded by co-complexation of fluorescein and polyelectrolyte onto UCNPs. Under NIR 980 nm excitation, the UCNPs emitted UV light to excite the photosensitive ONB group and carboxylic acid groups were formed. The polyelectrolyte layer changed from positively charged to negatively charged which disturbed the equilibrium of the UCNP@SiO_2 surface and polyelectrolyte. Ultimately, fluorescein molecules were released (Figure 13).[103]

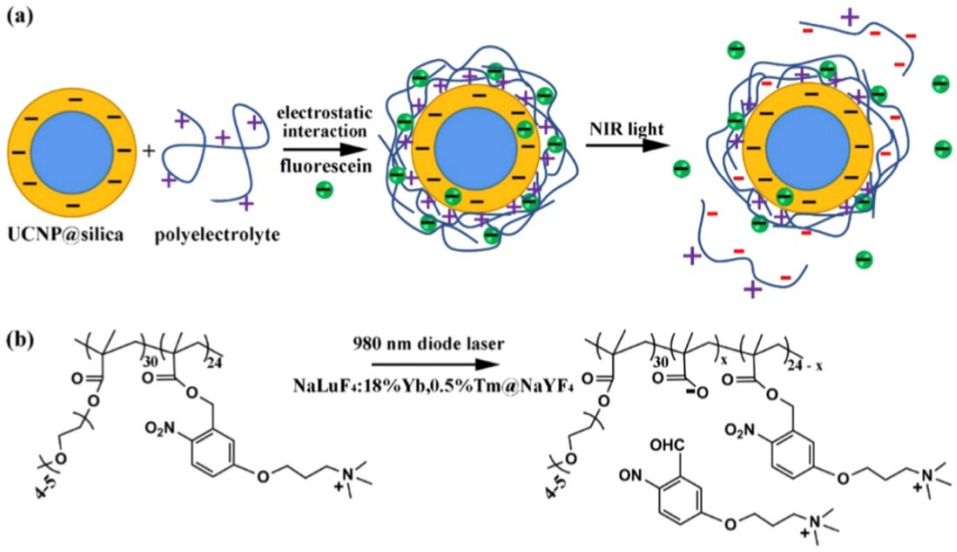

Figure 13. (a) Schematic illustration of NIR light-triggered polymer layer disruption and drug release from the UCNP@silica@polyelectrolyte self-assembled through electrostatic interactions. (b) Polymer chemical structure, UCNP ($NaLuF_4$:18%Yb,0.5% Tm@$NaYF_4$), and the NIR light-triggered photocleavage reaction of the photolabile polyelectrolyte.[103]

Controllable "on" and "off" drug release was reported in another example. Yao *et al.* demonstrated novel near-infrared-triggered liposome drug delivery system based on an upconverting nanoparticle encapsulated azobenzene liposome nanostructure.[75] By infrared radiation, the azobenzene molecules associated with the UCNPs convert from *trans* to *cis* under UV radiation and convert from the *cis* to the *trans* under blue radiation. This configurational change disrupts the liposome membrane and leads to controlled drug release. Jalani *et al.* reported

the development of $LiYF_4:Yb^{3+}/Tm^{3+}@SiO_2$ coated with a layer of chitosan hydrogel cross-linked with an ONB photocleavable crosslinker.[104] The chitosan layer encapsulated fluorescein isothiocyanate-bovine serum albumin (FITC-BSA) inside the gel. Under 980 nm excitation, the upconverted UV emission cleaves the crosslinked bonds and instantaneously liberates the FITC-BSA under as much as 2 cm thick tissue. The release is immediately arrested if the excitation source is switched off. While Dcona *et al.* demonstrated a fast release of Dox from UCNPs by loading a photocaged Dox directly onto the surface of the UCNP *via* an ONB photocleavable linkage. This system or the systems' derivatives should be compatible with release of Dox into cells in response to tissue penetrating NIR light (Figure 14).[105]

In conclusion, by reviewing the literatures of UCNPs in drug delivery, its non-invasive and high penetration nature has attracted great interest in developing a wide variety of promising drug delivery vehicle and systems.

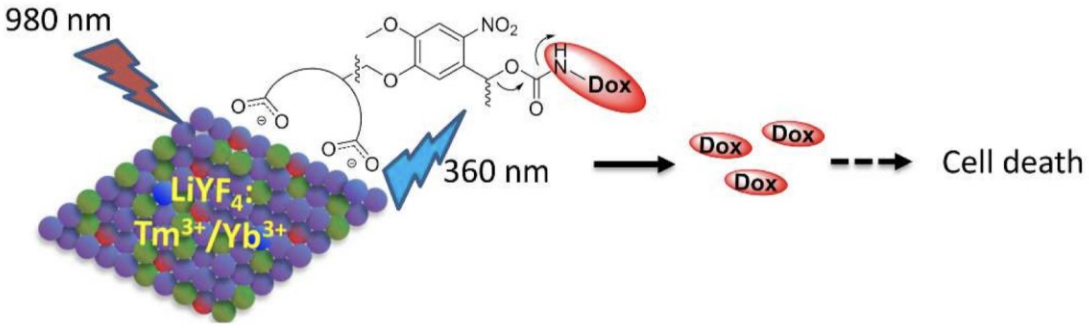

Figure 14. Schematic illustration of drug releasing system of UCNP and Dox conjugates. The incoming NIR excite the UCNP and the UV emission of UCNP leads to photocleavage and finally the release of drug.[105]

Chapter 3 Methods

3.1 Materials and instrumentation

3.1.1 Materials. Y_2O_3 (REacton 99.999%), Yb_2O_3 (REacton, 99.998%), Tm_2O_3 (REacton, 99.997%), 1-octadecene (ODE, 90%), and oleic acid (OA, 90%) from Alfa Aesar (USA); sodium borohydride from Anachemia; 1-ethyl-3-(3-dimethylaminopropyl)carbodiimide (EDC) from Matrix Innovation; and phosphate-buffered saline (PBS) tablets, sodium hydroxide (NaOH), sodium sulphate, nitric acid (70%), potassium carbonate, lithium trifluoroacetate (98%), oleylamine (OM, 70%), acetovanillone, dichloromethane (DCM), dimethylformamide (DMF), ethyl-4-bromobutyrate, hydrochloric acid (HCl), trifluoroacetic acid (TFA, 99%), molecular sieves (pore size = 3Å), 4-dimethylaminopyridine (DMAP), bis(hexamethylene)triamine (BHMT, 95%), levofloxacin, poly(ethylene glycol)-diamine (Mn = 3000 g/mol), PVA (Mw = 89 000 to 98 000 g/mol, 99.9% hydrolyzed) and poly(maleic anhydride-alt-1-octadecene) (PMAO, average Mn = 30,000-50,000) were purchased from Sigma-Aldrich and used as received. DCM and DMF were dried over molecular sieves (pore size = 3Å).

3.1.2 Instrumentation. The crystal phase of the UCNPs was determined *via* X-ray powder diffraction (XRPD) analysis on a Bruker D8 Advance Diffractometer (Germany) using Cu Kα radiation. Rietveld refinements were performed on the PXRD patterns of selected samples using Maud software.

The morphology and size distribution of colloidal UCNPs were investigated by transmission electron microscopy (TEM) analysis. TEM was performed using 200-mesh Cu TEM grids. The grids were imaged with the FEI Tecnai G2 F20 TEM equipped with the Gatan Ultrascan 4000 CCD camera Model 895 in bright field at 200 keV. The proprietary Digital Micrograph 16-bit images (DM3) were converted to unsigned 8-bit TIFF. ImageJ software was used to determine the average diameters and their distributions with minimum 200 nanoparticles per sample.[106]

The sizes and their distributions in hydrodynamic diameters of UCNPs in dispersions were measured by dynamic light scattering (DLS) at a fixed scattering angle of 175° at 25 °C with a Malvern Instruments Nano S ZEN1600 equipped with a 633 nm He−Ne gas laser. Upconversion emission spectra on an Avaspec-ULS2048L spectrometer (Avantes, The Netherlands) were recorded using at 980 nm continuous-wave laser diode excitation (BWT, China) with 435 mW

laser power and 346 W/cm^2 of power density. The upconversion emission was collected using a lens at a 90° angle from the excitation beam and upconversion emission was corrected to the number of UCNPs per unit volume, which varies for different sized UCNPs in the same m/v concentration. The number of UCNPs was estimated considering their crystalline phase, physical dimensions and material density properties. Absorption spectra were recorded on a Lambda 750 UV/Vis/NIR spectrometer (PerkinElmer, USA).[107] UV/vis spectra on an Agilent Cary 60 UV/vis spectrometer were recorded using a 1 cm wide quartz cuvette. Thermogravimetric analysis (TGA) was carried out using a TA instrument Q50 analyzer. Typically, dried samples were placed in a platinum pan inside a programmable furnace. They were then heated from 25 to 800 ℃ at a heating rate of 10 ℃/min under nitrogen flow. Mass loss was then calculated. ^{1}H NMR spectra were recorded using a 500 MHz Varian spectrometer. The residual $CHCl_3$ singlet at 7.26 ppm was selected as the reference standard.

3.1.3 Synthesis and surface modification of $LiYbF_4:Tm^{3+}$ (0.5%)/$LiYF_4$ UCNPs

I. Preparation of precursor solution. Core precursor solution was synthesized as follows. Yb_2O_3 (1.24 mmol), Tm_2O_3 (6.25 x 10^{-3} mmol) were added into a three-neck 50 mL flask. Distilled water (5 mL) and trifluoroacetic acid (5 mL) were added into the flask. The cloudy solution was stirred under reflux at 80 °C until it becomes clear. Solvent was evaporated at 60 °C for 24 hrs. To synthesize shell precursors, Y_2O_3 (2.5 mmol) was added into a three-neck 50 mL flask. Distilled water (5 mL) and trifluoroacetic acid (5 mL) were added into the flask. The cloudy solution was stirred under reflux at 80 °C until it became clear. Solvent was evaporated at 60 °C for 24 hrs. After the synthesis of core and shell precursors, the nanoparticles were prepared by thermal decomposition method. The core precursors were mixed with CF_3COOLi (2.5 mmol), oleic acid (5.25 mL), oleylamine (2.25 mL) and 1-octadecene (7.5 mL). The resulting mixture was heated to 125 °C with constant stirring under vacuum. In another 3 neck 100 mL flask, oleic acid (8.75 mL), 1-octadecene (12.5 mL) and oleylamine (3.75 mL) were mixed and degassed under vacuum at 150 °C. After 30 min, the temperature of the mixture was slowly increased to 330 °C under Ar flow. The solution with degassed precursors were then injected into the mixture of solvents at a rate of 1 mL min-1. The mixture was stirred for 1 hr at 330 °C, after which it was allowed to cool to room temperature under Ar flow.

II. Shelling of $LiYbF_4$: Tm^{3+} with $LiYF_4$. The shell precursors were mixed with CF_3COOLi (5 mmol), oleic acid (10 mL) and 1-octadecene (10 mL). The resulting mixture was heated to 125 °C with constant stirring under vacuum. In another three-neck 100 mL flask, the core solution (14.4 mL; equivalent to 1 mmol) was mixed with oleic acid (3 mL) and 1-octadecene (3 mL) and degassed under vacuum at 150 ^oC. After 30 min, the temperature of the mixture was slowly increased to 290 °C under Ar flow. The solution with shell precursor was injected into the core solution at a rate of 0.75 mL min^{-1} in three steps of even volume addition and allowed to react for 45 minutes after each step. The mixture was stirred for 1 hr at 330 °C, after which it was cooled to room temperature under Ar flow prior to precipitation with acetone. The nanocrystals were then separated *via* centrifugation (10000 rpm on Sorvall LYNX 4000 Superspeed Centrifuge) and further purified by precipitation from a 1/4 v/v hexane/acetone and following a 1/4 v/v hexane/ethanol mixtures upon centrifugation.

3.1.4 Fabrication of PMAO-crosslinked UCNPs colloids. A dispersion of OA-UCNPs (50 mg) in hexane (1 mL) was redispersed in chloroform (14 mL) and mixed with PMAO (0.21 g, 3 mL in chloroform) under stirring for 1 hr. After the addition of BHMT (0.4 mg, 100 μL), the resulting mixture was sonicated for 30 mins (Branson M1800 Ultrasonic Cleaner). The solvent was evaporated under vacuum by rotatory evaporation and then the residue was dispersed in water containing 1M NaOH (2 mL) and then sonicated for an additional 1 hr. The dispersion was subjected to filtration with a disk-type 0.45 μm pore-sized filter. The resulting PMAO-crosslinked UCNP colloids were isolated by centrifugation (10,000 rpm x 25 min at room temperature, Sorvall LYNX 4000 Superspeed Centrifuge, diameter = 80.5 cm). Their aliquots were ready to prepare stable dispersions in PBS solutions.

3.1.5 Synthesis of photo-cleavable levofloxacin-conjugated PEG (hvL-PEG)

Ethyl 4-(4-acetyl-2-methoxyphenoxy)butanoate (A1). An organic solution of acetovanillone (10 g, 60 mmol) and K_2CO_3 (16.6 g, 120 mmol) dissolved in DMF (100 mL) was mixed with ethyl-4-bromobutyrate (17.6 g, 90 mmol) and purged with N_2 for 20 mins in a 20 mL vial with magnetic stirring for 16 hrs. The reaction mixture was precipitated from water (1 L) for 2 hrs at room temperature and then placed at 4 °C for 16 hrs to promote more precipitation. The precipitate was filtered, lyophilized, and isolated as a white powder: Yield = 15.3 g (91%). ^1H

NMR (500 MHz, $CDCl_3$) δ 7.54 (m, 2H), 6.89 (d, J = 8.2 Hz, 1H), 4.20 – 4.09 (m, 4H), 3.91 (s, 3H), 2.60 – 2.48 (m, 5H), 2.18 (p, J = 6.8 Hz, 2H), 1.26 (t, J = 7.1 Hz, 3H).

Ethyl 4-(4-acetyl-2-methoxy-5-nitrophenoxy)butanoate (A2). The purified, dried A1 (10 g, 35 mmol) was slowly poured into 70% aqueous nitric acid solution (40 mL) in an ice bath under stirring for 3 hrs. The reaction mixture was precipitated from water (1 L) and placed at 4 °C overnight to promote precipitation. After the precipitate was filtered and dried, the product was recrystallized in ethanol, and then isolated as a yellow crystalline solid: Yield = 7.1 g (61%). ^{1}H NMR (500 MHz, $CDCl_3$) δ 7.60 (s, 1H), 6.74 (s, 1H), 4.20 – 4.117 (m, 4H), 3.95 (s, 3H), 2.54 (t, J = 7.2 Hz, 2H), 2.49 (s, 3H), 2.19 (p, J = 6.7 Hz, 2H), 1.26 (t, J = 7.1 Hz, 3H).

Ethyl 4-(4-hydroxyl-2-methoxy-5-nitrophenoxy)butanoate (A3). The purified, dried A2 (6 g, 18.4 mmol) and sodium borohydride (2.08 g, 55 mmol) were mixed in ethanol (100 mL) with molecular sieves (pore size= 3 Å). The reaction mixture was subsequently purged with nitrogen for 1 hr and then left for 16 hrs at 60 °C. The molecular sieves were filtered and the reaction mixture was washed with brine twice and water once. The organic phase was evaporated under vacuum using a rotatory evaporator. The product was dried *in vacuo* and isolated as a yellow solid: Yield = 3.6 g (60%). ^{1}H NMR (500 MHz, DMSO) δ 7.53 (s, 1H), 7.36 (s, 1H), 5.48 (d, J = 4.4 Hz, 1H), 5.33 – 5.19 (m, 1H), 4.17 –3.99 (m, 4H), 3.91 (s, 3H), 2.48 (m, 2H), 1.99 (p, J = 6.8 Hz, 2H), 1.37 (d, J = 6.2 Hz, 3H), 1.19 (t, J = 7.1 Hz, 3H).

Ethyl 4-(4-hydroxyl-2-methoxy-5-nitrophenoxy)butanoic acid (A4). The purified, dried A3 (1 g, 3.1 mmol) was dissolved into water (20 mL). A solution of TFA (4.7 mL, 61.1 mmol) was added slowly into the reaction mixture. The reaction mixture was stirred for 16 hrs at 90 °C. Thin Layer Chromatography (TLC; silica plate; hexane:ethyl acetate = 1:1) was carried out to ensure reaction completion. The black solid was filtered immediately and the filtrate was allowed to cool down to room temperature. The filtrate was cooled in an ice-bath to promote precipitation. The combined precipitates were then dissolved in a minimum amount of 1M NaOH (10 mL) and acidified to pH 1 by dropwise addition of conc. HCl. The product was filtered and dried *in vacuo* and isolated as a yellow brown solid: Yield = 0.61 g, (67%). ^{1}H NMR (500 MHz, DMSO) δ 12.18 (s, 1H), 7.55 (s, 1H), 7.37 (s, 1H), 5.50 (m, 1H), 5.27 (m, 1H), 4.07 (t, J = 6.5 Hz, 2H), 3.92 (s, 3H), 2.40 (t, J = 7.3 Hz, 2H), 1.96 (m, 2H), 1.37 (d, J = 6.2 Hz, 3H). These spectral data matched those previously reported.[70]

A photo-cleavable ONB-PEG (A5). The purified, dried A4 (0.3 g, 0.9 mmol), DMAP (0.03 g, 0.2 mmol) and PEG-diamine (1.2 g, 0.3 mmol) were dissolved in a minimum amount of DMF (5 mL) and DCM (15 mL) in an ice-bath. A solution of EDC (0.4 g, 2.2 mmol) in DCM (5 mL) was added dropwise into the reaction mixture under stirring for 10 mins and stirring was continued for 16 hrs at room temperature. The reaction mixture was washed with brine solution three times and dried over sodium sulfate. The reaction mixture was concentrated under vacuum by rotatory evaporation and precipitated in diethyl ether (600 mL). The product was filtered and isolated as a brown solid: Yield = 1.2 g (72%). Conjugation efficiency = 86%. (Section 4.2) ^{1}H NMR (500 MHz, DMSO) δ 7.89 (t, 1H), 7.55 (s, 1H), 7.37 (s, 1H), 5.50 (m, 1H), 5.27 (m, 1H), 4.07 (t, J = 6.5 Hz, 2H), 3.92 (s, 3H), 3.62 – 3.40 (s, 4H), 2.40 (t, J = 7.3 Hz, 2H), 1.96 (m, 2H), 1.37 (d, J = 6.2 Hz, 3H).

Levofloxacin conjugated PEG-photocleavable molecules (hvL-PEG). Levofloxacin (1.2 g, 3 mmol) was pre-activated by EDC (1.6 g, 8 mmol) and DMAP (0.9 g, 7 mmol) in anhydrous DCM (20 mL) under purging with nitrogen. The purified, dried A5 (0.2 g, 0.05 mmol) was dissolved in anhydrous DMF (5 mL) purged with nitrogen and injected into the EDC reaction mixture under stirring. The stirring continued for 3 days at room temperature in the dark. The mixture was washed with brine three times and distilled water once. After it was dried over sodium sulphate and concentrated by rotatory evaporation, the product was precipitated from diethyl ether. The product was filtered as pale brown solid: Yield = 0.15 g (60%). Conjugation efficiency = 91%. (Section 4.2)

3.1.6. Fabrication of electrospun fibers

General procedure for electrospinning to fabricate nanofibers. The electrospinning process was carried out by applying a voltage of 23 kV to the precursor polymer solution at a feed rate of 0.6 mL/hr (LEGATO® 110 syringe pump from KD Scientific, U.S.A.), using a 2 mL glass syringe (Becton Dickinson and Co., U.S.A.) and a 21 gauge syringe needle. In general, a given amount of PVA was dissolved in water (2 mL) under stirring at 90 °C for two hours. The formed PVA solution was transferred to a 2 mL glass syringe (Becton Dickinson and Co., U.S.A.) equipped with a 21 gauge syringe needle for electrospinning. The electrospun nanofibers were collected on an aluminium foil-wrapped plastic stand placed 8 cm from the syringe tip. The collected fibrous mat was rinsed with methanol and dried in an oven at 50 °C for 16 hrs.

3.1.7 Fabrication of crosslinked PMAO-x/UCNP-embedded crosslinked PVA fibers (UCNP/hvL-PEG fibers). A home-made electrospinning set-up is shown in Figure 15. A similar procedure described in Section 3.1.6 was used to prepare PMAO-x/UCNP-embedded fibers from a clear solution composed of an aqueous PMAO-x/UCNP colloids (0.5 mL) dispersed in a 12 wt% aqueous PVA solution (2 mL). For crosslinking, the formed electrospun fibers were immersed in acetone (20 mL) were mixed with a trace amount of conc. HCl and GA (10 mol% HCl with respect to GA; CHO:OH mol eq. ratio = 4:1) for 30 min. The fibers were then washed with methanol (10 mL) three times and dried in an oven at room temperature for 16 hrs.[108-109]

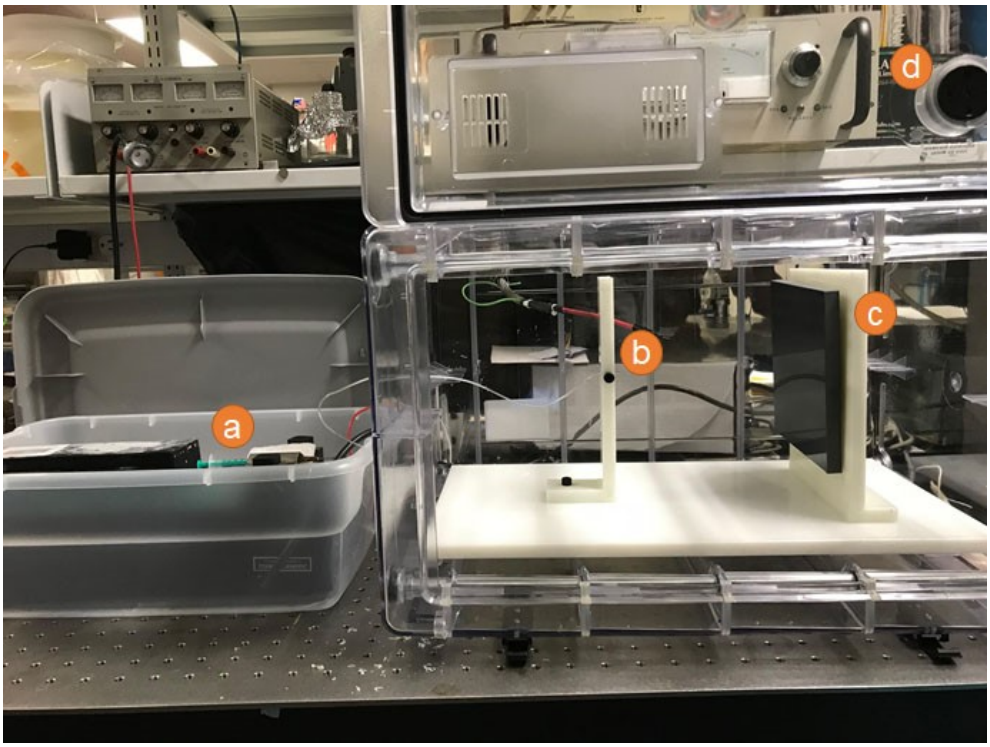

Figure 15. A digital image of our home-made electrospinning set-up with (a) syringe pump, (b) syringe tip, (c) plastic stand and (d) high voltage source.

3.2. Characterization and evaluation

3.2.1 Swelling ratio. Pieces of dried PVA fibers (100 mg) were immersed into Phosphate Buffer Saline (PBS) solution (40 mL) at room temperature. After 24 hrs, they were wrapped with a Kimwipe™ to remove residual solution from the fibers. The swelling ratio was determined by the weight ratio wet to dry fibers.

3.2.2 *In vitro* drug release. For solution samples, levofloxacin (2 mg) was dissolved in water (2 mL) in a dialysis tube (MWCO = 1.0 kDa), and hvL-PEG (2mg) in water (2 mL) in a dialysis tube. For fiber samples, various PVA fibers were fabricated using the standard procedure (as described in section 3.1.7) by electrospinning from a series of 12 wt% aqueous PVA solutions (2 mL) mixed with levofloxacin (2 mg) for levofloxacin-loaded fibers, hvL-PEG (2 mg) for hvL-PEG-loaded fibers, and both PMAO-x/UCNP (25 mg) and hvL-PEG (2 mg) for PMAO-x/UCNP-hvL-PEG-embedded fibers. The formed fibers were subjected to GA-induced crosslinking. Pieces of the formed fibers (100 mg) were mixed with PBS solution (40 mL) and placed in a dialysis tube (MWCO = 1.0 kDa). For solution samples, aqueous solutions of levofloxacin (2 mg) dissolved in water (2 mL) or hvL-PEG (2 mg) dissolved in water (2 mL) were placed in a dialysis tube (MWCO = 1.0 kDa). All drug release tests were carried out in triplicate.

For samples of levofloxacin solutions and levofloxacin-embedded fibers, our release experiments started immediately after the samples were placed in dialysis tubing in PBS solution (40 mL). Fiber samples containing light-cleavable ONB linkages were stored in solution in the dark for 24 hrs before release experiments. hvL-PEG-embeded fiber samples were subjected to irradiation with UV light at 365 nm (4W). PMAO-x/UCNPembedded PVA fibers were irradiated with 980 nm NIR (1W) laser. Aliquots of outer PBS solutions (4 mL) were taken periodically to record the UV-vis spectrum and replaced with the same volume of fresh PBS solutions to maintain sink condition. Sink condition is defined as the volume of dissolution medium, with or without a solubiliser, needed to provide complete dissolution of the expected amount of drug present in the product. [22, 110-111]

To calculate the accumulative drug released from the sample, the absorbance at different times were first converted to concentration (mol L^{-1}) and then converted to amount (μg). The amount (μg) were multiplied by ten (amt. x10) because 4 mL of solution was removed from the 40 mL PBS solution each time. The accumulative drug release was calculated by the sum of the amt. x10 at that time and the amount in μg of all the previous time points. In this way, the concentration of the discarded PBS solutions was also accounted for.

3.2.3 Bacterial cultivations. *Escherichia coli* (*E. coli*, ATCC 25922) and *Staphylococcus aureus* (*S. aureus*, ATCC 29213) were acquired from the American Type Culture Collection (ATCC). The disk diffusion method was adapted from the Clinical & Laboratory Standards

Institute (CLSI) standard protocol.[112] Briefly, bacteria were grown in Mueller Hinton Broth (MHB) media at 37 ℃ rotating at 225 rpm. Bacterial isolates were resuspended in MHB media and streaked on 1.5% Mueller Hinton Agar (MHA) plates and placed at 37 °C for 18-24 hrs prior to each experiment. Following CLSI guidelines, for broth microdilution and direct colony suspension testing, bacterial cultures were transferred to MHB (*E. coli*) and adjusted to a final turbidity equivalent to a 0.5 McFarland standard (1 X 10^6 CFU/mL). Bacteria were spread on MHA plates using sterile cotton swabs before adding the nanofibers mats (10 mm in diameter) using a sterile spatula. The plates were then incubated at 37 ℃ for 16-20 hrs. Zones of inhibition (ZOI) were measured in mm using a ruler.

3.2.4 Statistical analysis. Data were recorded as mean ± standard deviation (SD). The average diameters of the nanofibers and inhibition zones in disc diffusion assays were measured using ruler.

Chapter 4 Synthesis, drug delivery and antimicrobial evaluation of PVA fibers

4.1 Fabrication of aqueous PMAO-crosslinked UCNP colloids

Well-defined colloidal UCNPs with the chemical composition of $LiYbF_4:Tm^{3+}$ (0.5%)/$LiYF_4$ stabilized with oleic acid (OA-UCNPs) in hexane were synthesized by a thermal decomposition method at 330 °C. The detailed procedure with the use of oleic acid (a coordinating ligand), 1-octadecene (a noncoordinating ligand), and oleylamine as a solvent is described in section 3.1.3.[113] Passive shelling was performed on core lanthanides because the optically inactive shell can reduce the energy loss from the core to the surrounding solvent molecules. Transmission electron microscopy (TEM) analysis confirmed that the resulting core/shell nanocrystals were diamond-shaped, with a diameter of 46.4 ± 3.5 nm (Figure 16b), which is larger than that of 29.2 ± 3.1 nm for $LiYbF_4:Tm^{3+}$ core nanocrystals (Figure 17a). Dynamic light scattering (DLS) analysis gave a diameter of 69.1 nm in a monomodal distribution (Figure 16c). Upon excitation with 980 nm NIR laser light, the dispersion of nanocrystals exhibited strong upconversion emission spanning the UV, visible and IR regions. Figure 17b shows the emission spectrum of the UCNP colloids with peak assignments corresponding to energy level transitions. The two upconverted UV emissions at *ca.* 350 nm are assigned to the $^1I_6 \rightarrow {}^3H_6$ and $^1D_2 \rightarrow {}^3H_6$ transitions, the three blue emissions at *ca.* 500 nm are assigned to the $^1D_2 \rightarrow {}^3F_4$, $^1G_4 \rightarrow {}^3H_6$ and $^1D_2 \rightarrow {}^3H_5$ transitions, the red emission at *ca.* 650 nm is assigned to the $^1G_4 \rightarrow {}^3F_4$ transition. The infrared emission at *ca.* 800 nm is assigned to the $^3H_4 \rightarrow {}^3H_6$ transition.[113] The X-ray diffraction (XRD) pattern of the nanocrystals (Figure 18) indicates the formation of the tetragonal phase and is indexed to the corresponding hkl planes.[114] The dopant ions, Tm^{3+} and Yb^{3+}, are situated in the crystal lattice with S_4 point symmetry.[115]

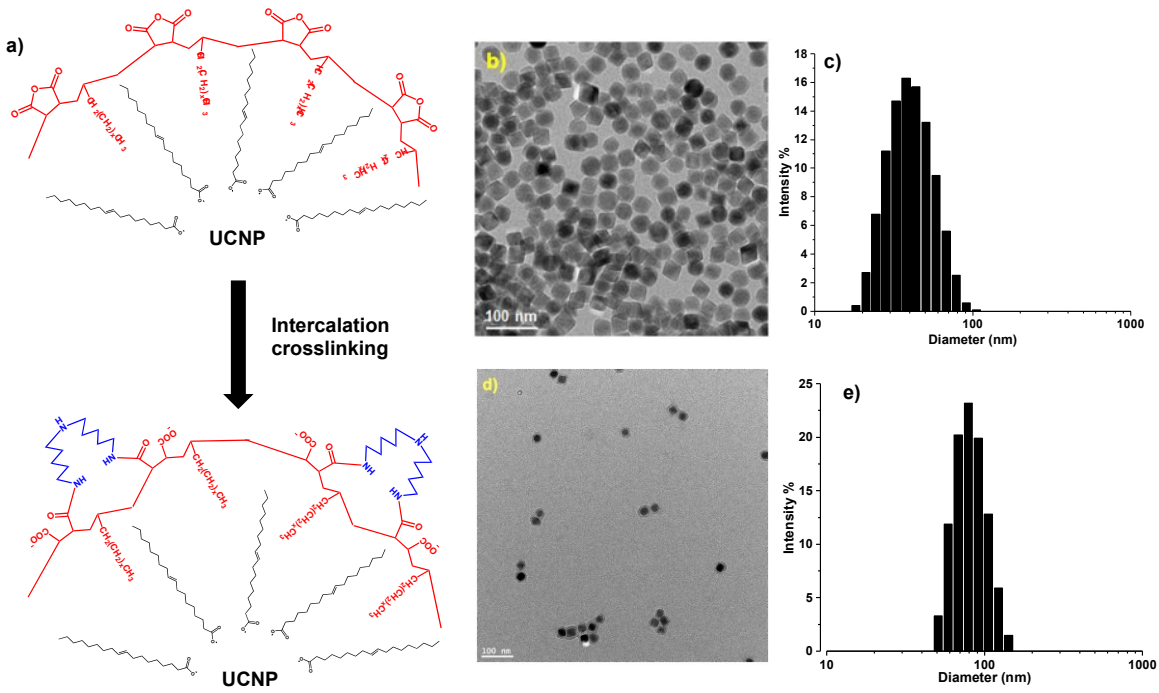

Figure 16. (a) Schematic illustration to fabricate aqueous PMAO-x/UCNP colloids through intercalation and following crosslinking. (b) TEM image and (c) DLS diagram of organic OA-UCNP colloids and (d) TEM image and (e) DLS diagram of PMAO-x/UCNP colloids.

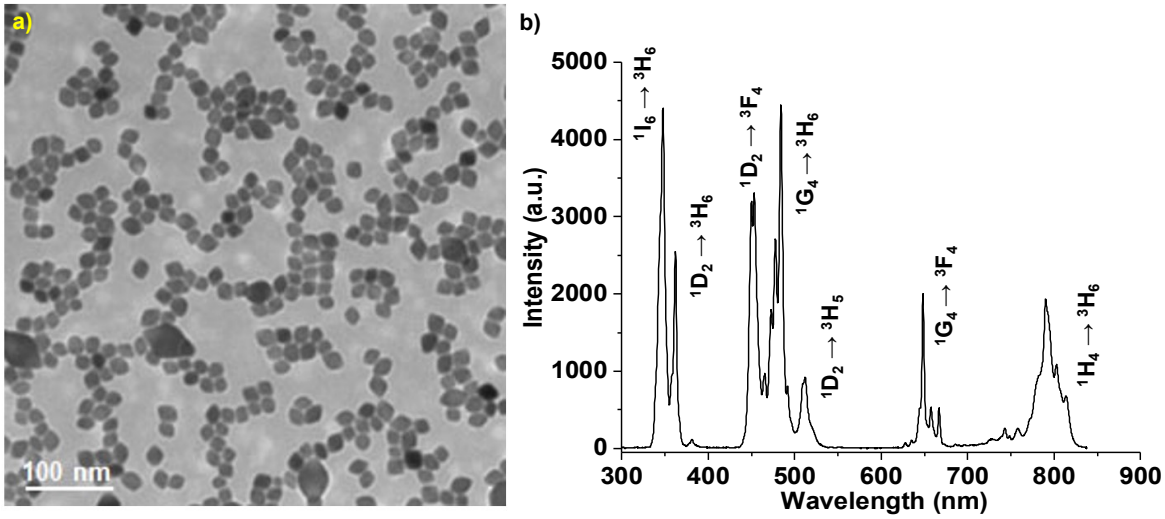

Figure 17. (a) TEM image of $LiYbF_4$: Tm^{3+} and (b) emission spectrum of $LiYbF_4$: Tm^{3+}/$LiYF_4$ UCNPs.

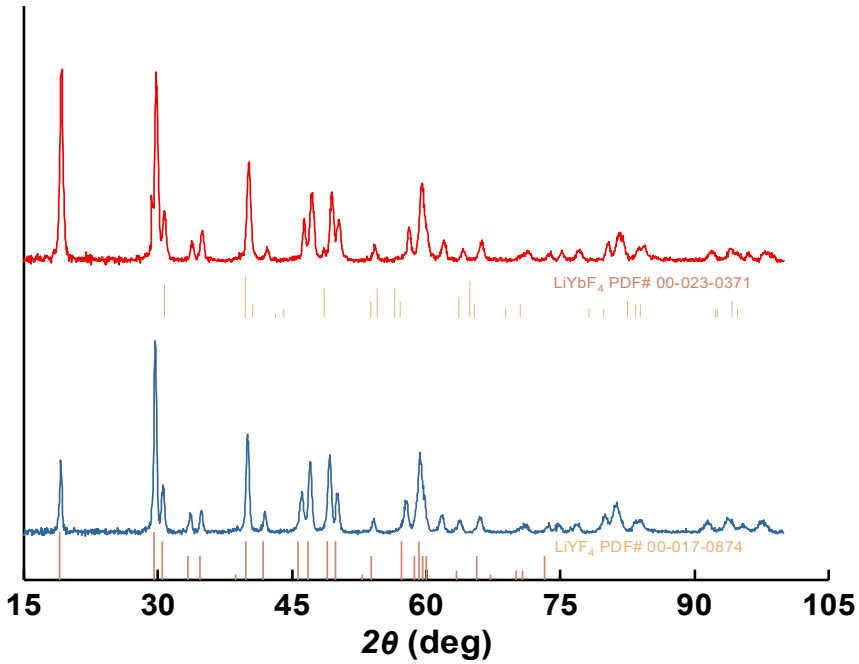

Figure 18. XRD of $LiYbF_4:Tm^{3+}$and $LiYbF_4:Tm^{3+}$/ $LiYF_4$ UCNPs.

The purified OA-UCNPs were coated with PMAO, yielding colloidally-stable PMAO-crosslinked UCNP colloids (PMAO-x/UCNPs) in aqueous solution. Figure 16a illustrates the two-step procedure, including: (1) the intercalation of long alkyl chains of OA bound to the UCNP surfaces with hydrophobic pendant octadecane chains of PMAO and (2) the subsequent crosslinking of the PMAO carboxylic acid groups with BHMT through an EDC coupling reaction. The detailed synthesis and structural characterization of the same nanoparticles by fourier-transform infrared spectroscopy (FT-IR), X-ray photoelectron spectroscopy (XPS), and thermogravimetric analysis (TGA) are reported eleswhere.[116] From the TGA analysis, the organic coating was estimated to be *ca.* 6% for the PMAO-x/UCNP colloids. The formed PMAO-x/UCNP colloids had an average diameter for the UCNP core of 40.4 ± 2.2 nm, which is similar to that determined for the OA-UCNPs by TEM analysis (Figure 15d). As expected, the hydrodynamic diameter by DLS was larger (89.0 nm) (Figure 15e).

4.2 Synthesis and photo-responsive properties of a photo-cleavable levofloxacin-conjugated PEG (hvL-PEG).

The scheme shown in Figure 19 to synthesize levofloxacin-PEG-ethyl 4-(4-hydroxyl-2-methoxy-5-nitrophenoxy)butanoic acid (hvL-PEG) involves six-steps and is based on three literature procedures with modifications.[22, 70, 78] Starting from acetovanillone, alkylation was performed to introduce an ester group on the molecule (A1). Nitration occurred at the *ortho* position because of the -OCH_3 *para*-directing group and the bulky alkyl chain preventing nitration at the *meta* position (A2). Reduction (A3) and hydrolysis were subsequently performed to obtain ethyl 4-(4-hydroxyl-2-methoxy-5-nitrophenoxy)butanoic acid (A4). A4 was then EDC coupled with PEG-diamine to impart hydrophilicity to the molecule. Levofloxacin was conjugated to the this precursor (A5) through another facile EDC coupling reaction in the last step to synthesize hvL-PEG (A6). All intermediates were characterized by ^{1}H-NMR spectroscopy (Figure 20-25).

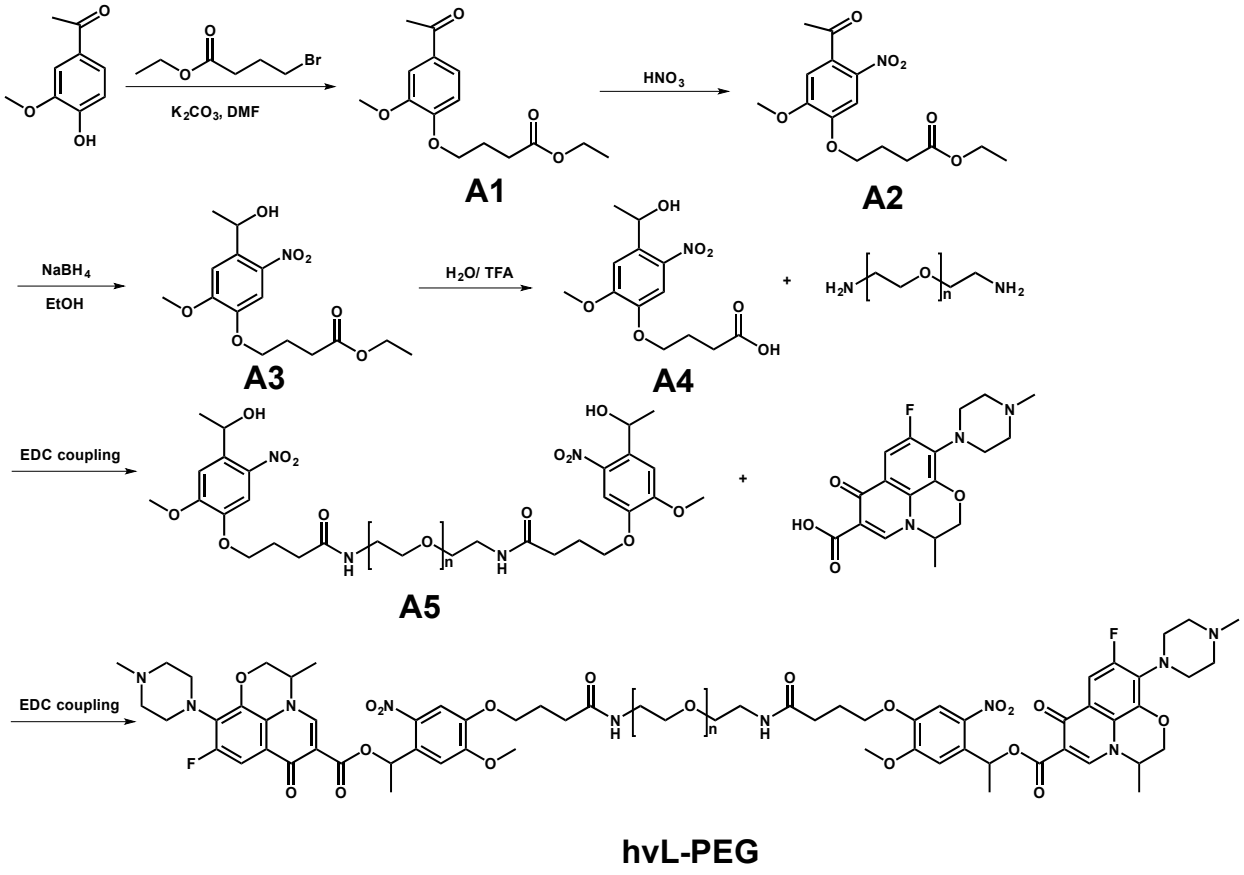

Figure 19. Overall reaction scheme to synthesize hvL-PEG.[22, 70, 78]

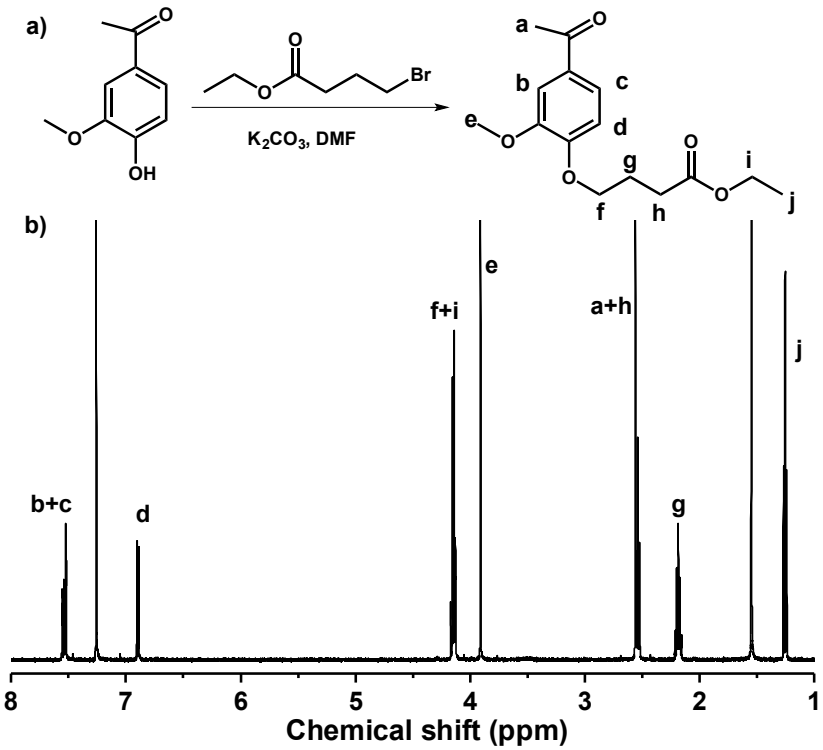

Figure 20. (a) Reaction scheme and (b) ^{1}H-NMR in $CDCl_3$ of A1.

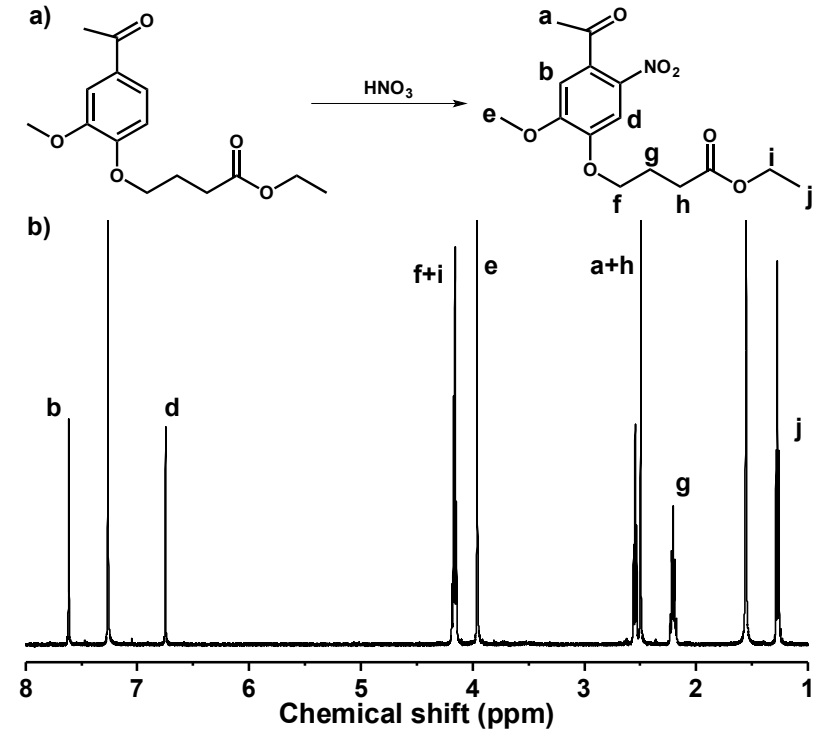

Figure 21. (a) Reaction scheme and (b) ^{1}H-NMR in $CDCl_3$ of A2.

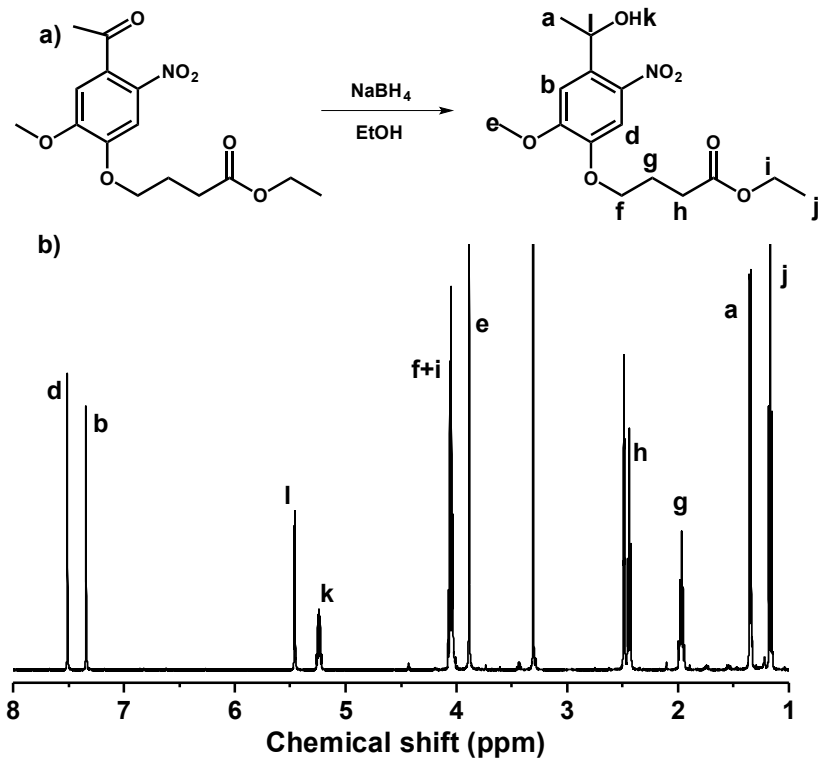

Figure 22. (a) Reaction scheme and (b) ^{1}H-NMR in $CDCl_3$ of A3.

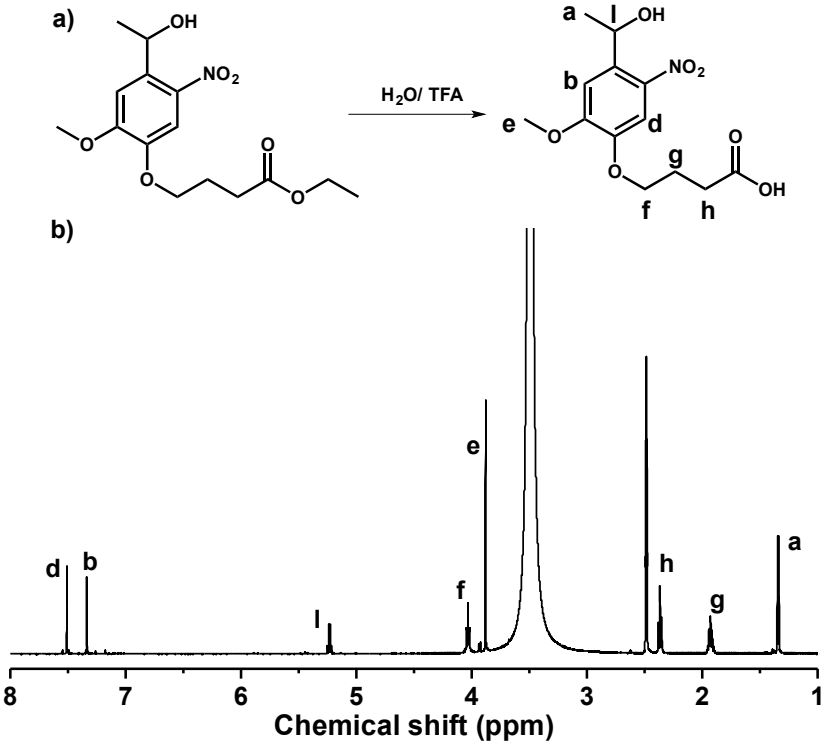

Figure 23. (a) Reaction scheme and (b) ^{1}H-NMR in $CDCl_3$ of A4.

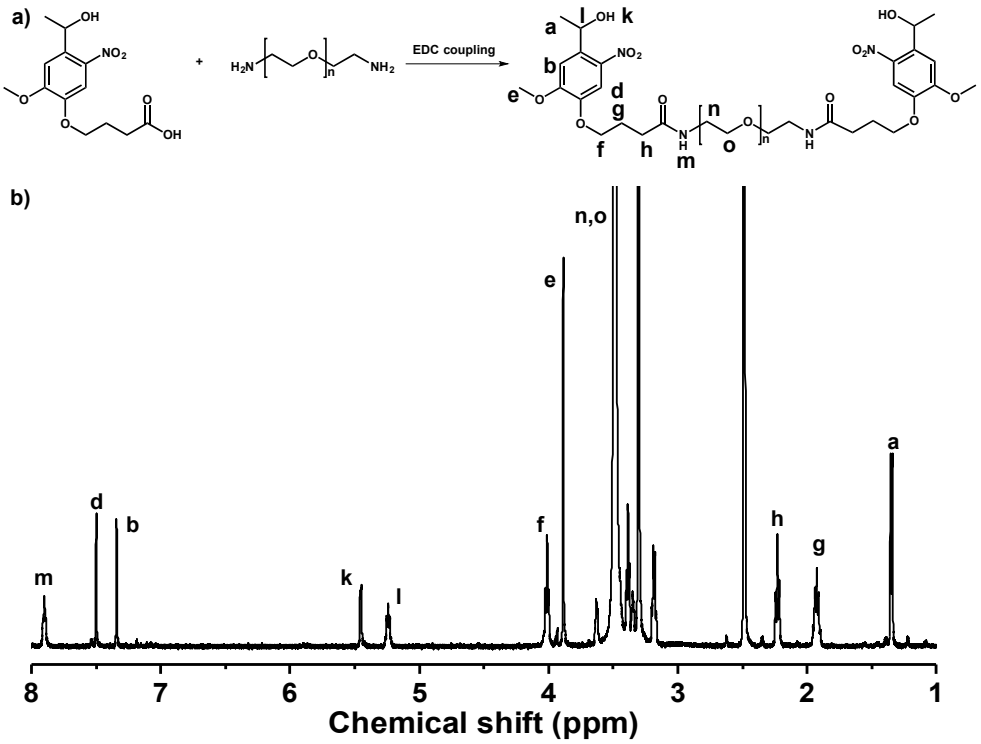

Figure 24. (a) Reaction scheme and (b) ^{1}H-NMR in $CDCl_3$ of A5.

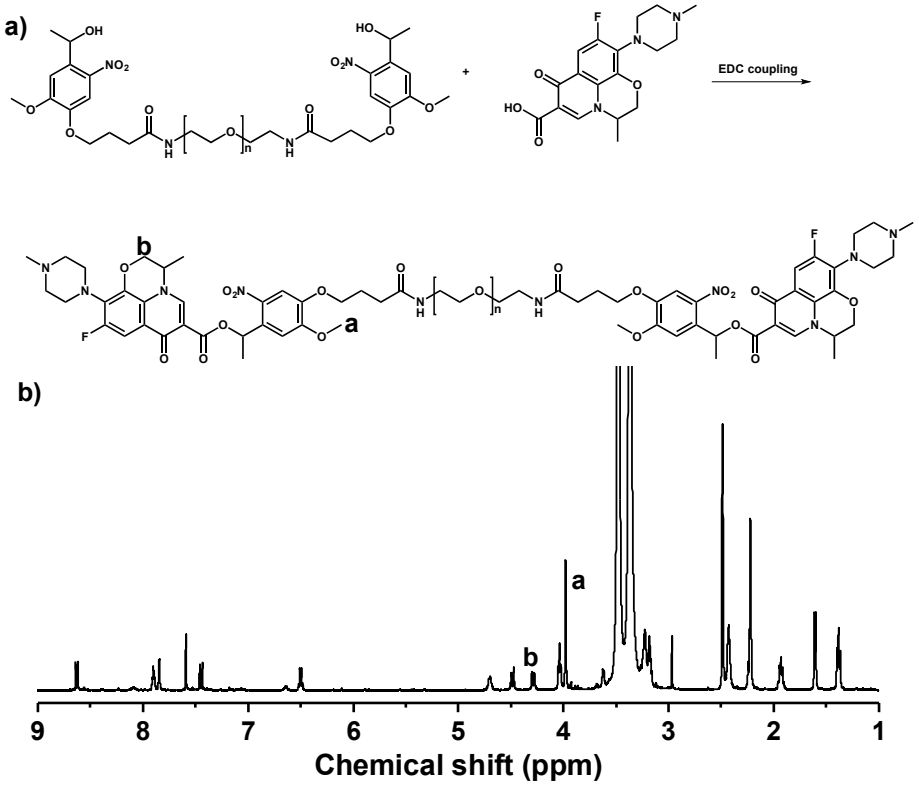

Figure 25. (a) Reaction scheme and (b) ^{1}H-NMR in $CDCl_3$ of A6.

The ^{1}H-NMR spectrum of A6 in Figure 16a shows the peaks at δ 4.25 ppm, 4.5 ppm and 4.75 ppm which correspond to levofloxacin, confirming its conjugation to PEG. Furthermore, the peak at δ 5.25 ppm corresponding to the methylene protons adjacent to the terminal OH group (A5) prior to conjugation is virtually absent, confirming the high conjugation efficiency. While the peak at δ 6.5 ppm corresponds to the methylene group adjacent to the ester groups after conjugation. Using the integration ratio of peak a (3.00) to peak b (0.91) (Figure 25), the conjugation efficiency of levofloxacin was determined to be *ca.* 45%, which is much greater than that reported in the literature (4%).[104] All reaction conditions were the same as the literature procedure except for the amount of levofloxacin. The literature procedure used 3.5 times excess of levofloxacin. It is believed that the use of excess molar equivalents of levofloxacin (30 times) herein likely contributed to the significant increase in conjugation. The product was further characterized with UV-vis absorption spectroscopy, where the maximum absorption at 289 nm confirms the conjugation of levofloxacin to the PEG derivative (Figure 26).

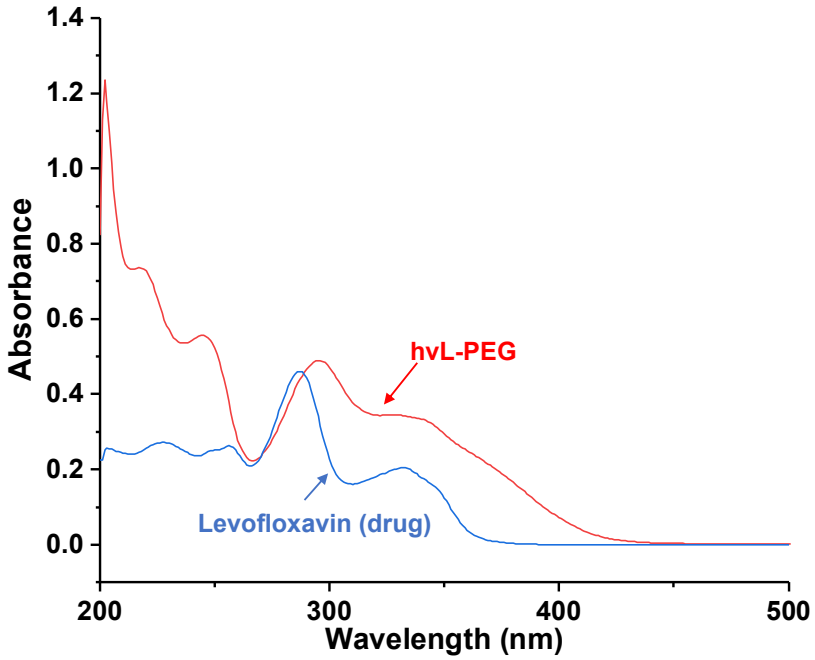

Figure 26. UV/Vis spectra of hvL-PEG (A6; red), compared with levofloxacin (blue) in PBS buffer.

Upon our successful synthesis of hvL-PEG with high conjugation efficiency, the cleavage of the ONB linkage upon UV irradiation was examined. An aqueous solution of hvL-PEG dissolved

in PBS solution (pH = 7.4) was placed in dialysis tubing (MWCO = 1000 Da). Figure 27b shows an overlay of UV spectra of outer PBS solution sampled at specified times. As expected, the absorbance at 289 nm increased with irradiation time, which is attributed to the increasing amount of free levofloxacin that diffused through the dialysis membrane upon cleavage of ONB linkages.

The spectroscopic overlap of the UV absorption spectrum of hvL-PEG with the emission spectrum of the UCNPs was confirmed (Figure 27c). It shows significant overlap in the 300-400 nm range, which favors the cleavage of the ONB linkages by the absorption of light emitted from the UCNPs in this range. This absorption ultimately leads to the release of levofloxacin from hvL-PEG.

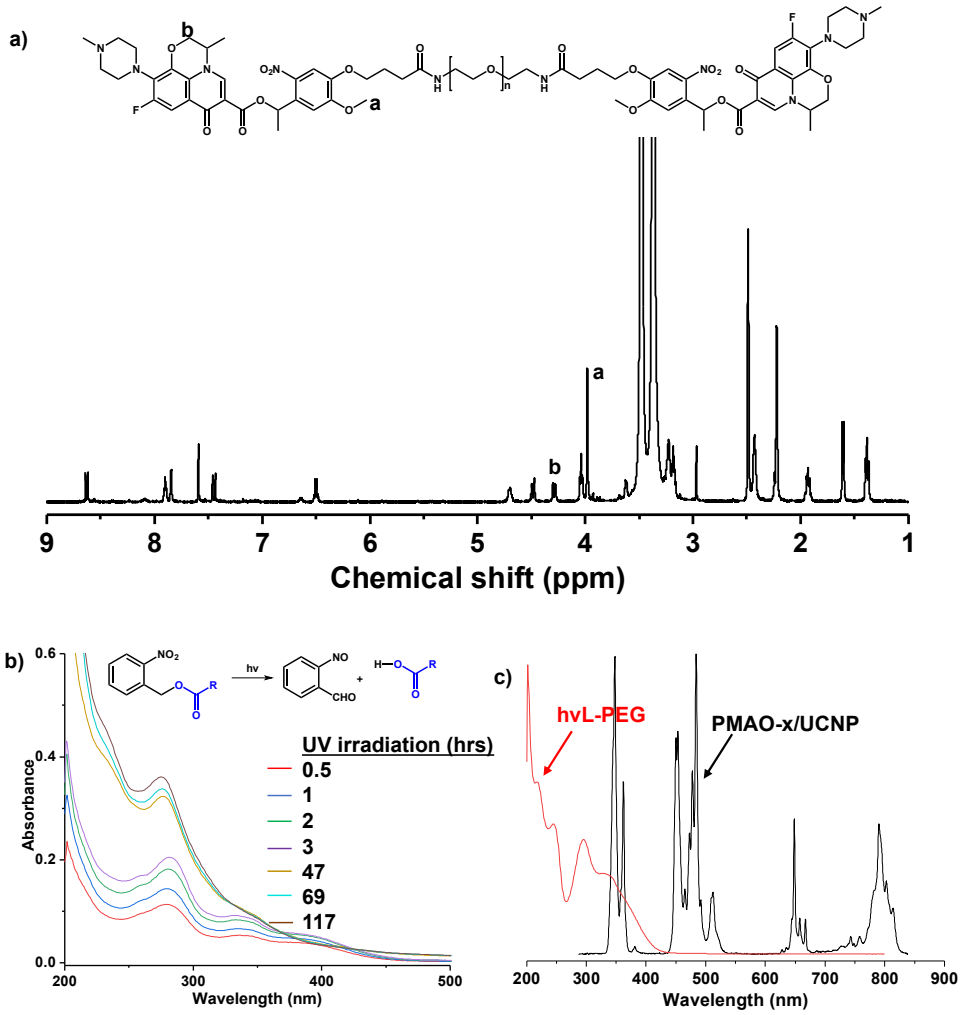

Figure 27. (a) Chemical structure and ^{1}H-NMR spectrum of hvL-PEG, (b) overlaid UV/vis spectra of levofloxacin drug molecules diffused through dialysis tubing upon the cleavage of ONB linkages in hvL-PEG in PBS, and (c) overlap of UV absorption spectrum of hv-L-PEG (red) with emission spectrum of UCNPs (black).

4.3 Investigation of electrospinning to fabricate UCNP-embedded electro-spun PVA fibers.

We constructed a home-made electrospinning setup shown in Figure 15 and optimized its instrumental parameters (*i.e.* voltage, injection rate and distance between the syringe tip and collector plate) to produce high-quality fibrous mats (see inset in Figure 28a to 28c). With the optimized conditions, the concentration of PVA solution was varied at 10, 12, and 14 wt%. SEM images in Figure 28 shows the formation of bead-free and uniform PVA fibers. Using image J, their diameters were estimated to be 124 ± 20 nm for 10 wt% PVA, 150 ± 21 nm for 12 wt% PVA, and 171 ± 28 nm for 14 wt% PVA. The diameter linearly increased with increasing weight %, which is likely due to the increasing viscosity of the aqueous PVA solution (Figure 28d).

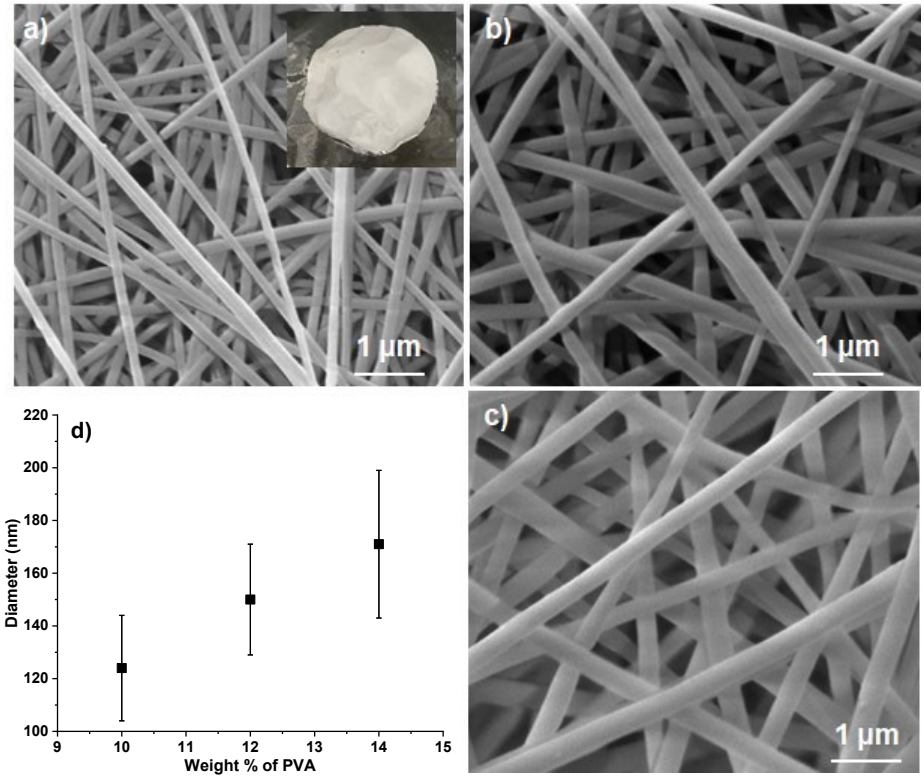

Figure 28. The SEM images of (a) 10 wt% PVA fibers with the appearance of PVA fibers in the inset with diameter of 4 cm, (b) 12 wt% PVA fibers, (c) 14 wt% PVA fibers as well as (d) linear relationship of average diameter of fibers over PVA concentration.

An integration of UCNP colloids into PVA fibers was investigated to fabricate PMAO-x/UCNP embedded fibers from a clear solution consisting of PVA and PMAO-x/UCNP colloids in water. To prevent the PVA fibers from dissolving in water, they were crosslinked with GA in

acidic solution. Using a literature procedure,[108] the amount of GA was set with a mole equivalent ratio of CHO/OH = 2/1 in the presence of a trace amount of HCl as an acid catalyst. The resulting crosslinked fibers did not dissolve but swell in water with a swell ratio of 3.5 ± 0.2 in PBS buffer (pH = 7.4). TGA analysis confirmed the amount of UCNPs in the fibers to be 10.9 (wt%) (Figure 29).

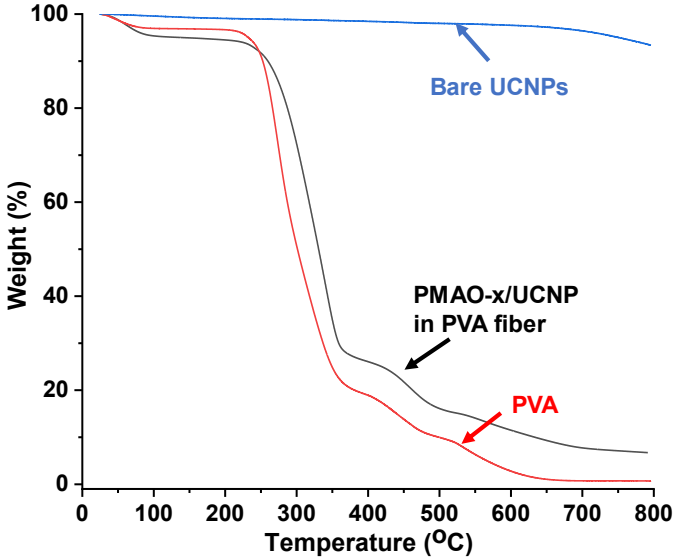

Figure 29. TGA of bare UCNPs, PVA and PMAO-x/UCNP in PVA fiber.

4.4 NIR-responsive drug release studies

The release of the drug from wound dressing materials is usually based on passive diffusion in traditional drug-loaded wound dressings, which cannot achieve on-demand and controllable release when required. The electrospun nanofibers embedded with UCNPs and hvL-PEG (a drug conjugates) were designed to release levofloxacin drug upon cleavage of the ONB linkages in response to NIR radiation. To ensure that the drug release is due to NIR radiation, several control experiments were performed. hvL-PEG conjugate was first put into a dialysis tube with MWCO = 1kDa. Because the MW of hvL-PEG is greater than 5 kDa, one can expect that only drug would be allowed to diffuse out of the tubing. As shown in Figure 30a, no drug came out of the dialysis tubing when there was no UV radiation. However, upon UV radiation, the release of drug molecules was rapid, reaching to > 90% within 1 day, as a consequence of the cleavage of ONB linkages between drug and the PEG precursor. Promisingly, this release rate is comparable with that of free drug from the dialysis tubing in the same period of time. Given this encouraging

observation of drug release from aqueous solution, we next investigated light-responsive drug release from PVA fiber systems.

The next control experiment prior to using NIR irradiation was to test the release of levofloxacin from hvL-PEG/PVA fibers upon UV irradiation. For quantative analysis, the extinction coefficient of levofloxacin in PBS at 289 nm was first determined to be 32056 L mol^{-1} cm^{-1} (Figure 31) and used to calculate the amount of levofloxacin released from fibers at given times with its absorbance obtained of levofloxacin using the Beer-Lambert equation. As seen in Figure 30b, no release of levofloxacin was observed until exposure to UV irradiation. Upon UV radiation, levofloxacin molecules abruptly released, reaching 65% in the first 30 mins, and then gradually increased with time. In another set of control experiments, free levofloxacin embedded PVA fibers were used for comparison (Figure 30c). Similar to the hvL-PEG-embedded fibers upon UV irradiation, an abrupt release of free levofloxacin molecules was observed, and the accumulative release of levofloxacin reached to 70%; however, this system also showed incomplete release. These results from two fiber systems show that levofloxacin molecules can be released from hvL-PEG after cleavage of the ONB linkage upon UV irradiation. Compared with the accumulative drug release in the same time period, the release of levofloxacin from fibers appears to be slower than that for the system of free hvL-PEG in solution. This suggests that the release could be delayed due to several barriers such as crosslinking density of the fibers and diffusion of levofloxacin molecules from the crosslinked fiber network.

Give these positive results, the release of levofloxacin from UCNP/hvL-PEG fibers was next examined (Figure 30d). Similar to hvL-PEG PVA fibers, no release was observed until exposure to NIR radiation. Upon NIR radiation, levofloxacin molecules were released abruptly and the accumulative release reached approximately 70%. As seen in Figure 27c, cleavage of the ONB linkage in the fibers could be a consequence of the spectral overlap of the ONB UV/vis absorption spectrum with the emission spectrum of the UCNPs at 289 nm. Furthermore, these fibers had comparable release rates and accumulative levofloxacin release with the hvL-PEG/PVA fibers upon UV irradiation. This is extremely promising in that the PMAO-x/UCNP colloids and hvL-PEG could be confined in suitable proximity to allow for energy transfer from the UCNP emission to the ONB absorption within the fibrous mesh.

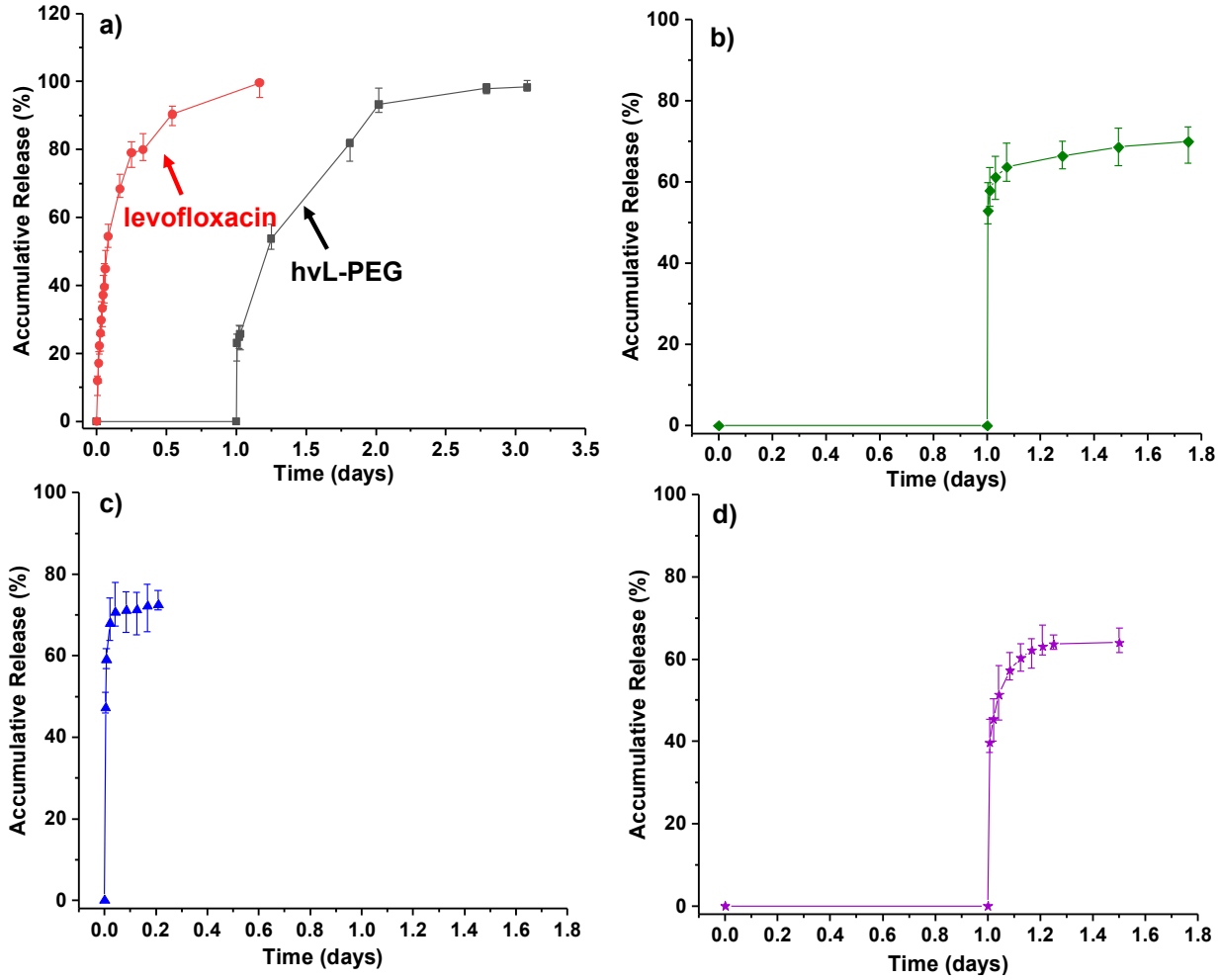

Figure 30. The release profile for (a) aqueous solutions of levofloxacin and hvL-PEG as well as (b) fibers of hvL-PEG upon UV irradiation after 1 day, (c) free Lev (c), and (d) both PMAO-x/UCNP and hvL-PEG upon NIR irradiation after 1 day.

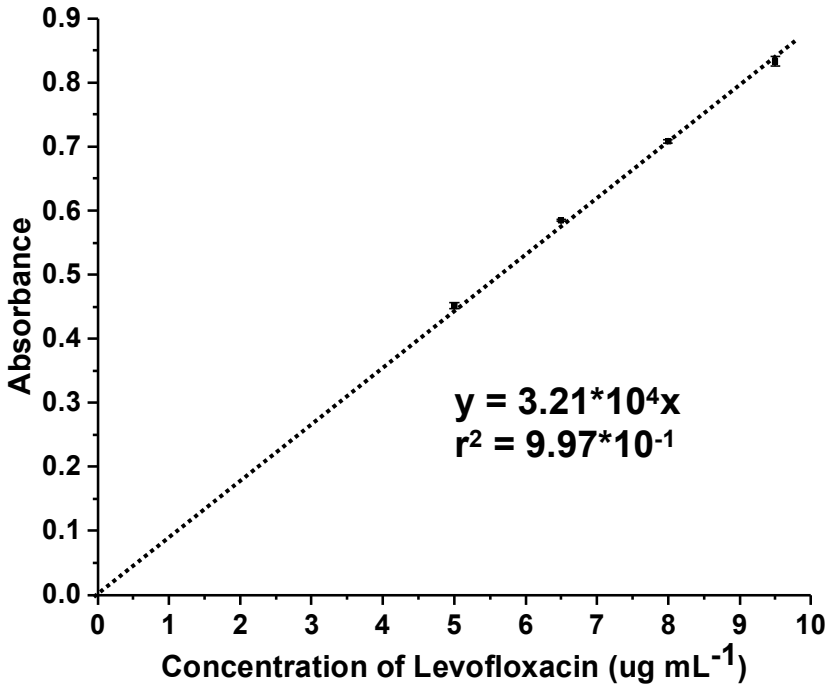

Figure 31. Calibration curve of levofloxacin in PBS solution.

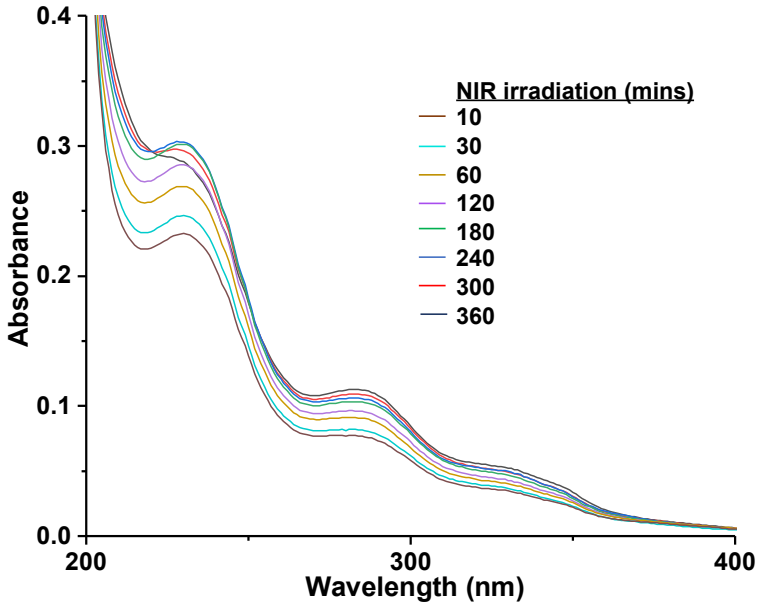

Figure 32. UV-vis absorption spectrum of drug release under NIR irradiation (980 nm, 1 W).

4.5 MIC determinations

The Gram-positive bacteria *Staphylococcus aureus* (*S. aureus*) and Gram-negative bacteria *Escherichia coli* (*E. coli*) are common pathogenic bacteria, with *S. Aureus* especially prevalent in skin infections.[111, 117] Here, they were examined as model organisms to evaluate the antimicrobial properties of our nanofibers. Figure 33 shows the digital images of *S. aureus* (a) and *E. coli* (b), 16-20 hrs after being cultured with various PVA fibers. This assay allows the determination of the zone of inhibition (ZOI) diameter as a measure of antibacterial activity. For *S. aureus*, the ZOI was close to zero with crosslinked, uncrosslinked PVA embedded without and with hvL-PEG conjugate (sampes 1-3).

As the bacteria grew on the agar plate, the cleaved drug released from the fiber samples 5 and 6 inhibited the growth of both bacterial strains (Figure 33b). Once the samples are pre-irradiated with NIR radiation (980 nm, 1W), as seen in samples 5 and 6, ZOIs are clearly seen (Table 2 and 3). Both of the samples have a similar ZOI, in line with similar levels of drug released following 1 hr and 2 hrs of irradiation. In the case of *E. coli*, sample 1 has a ZOI of 14 mm, suggesting PVA itself is toxic to *E. coli*. Sample 2 and 3 exhibited similar ZOIs of 19 mm and 18 mm respectively, higher in comparison to sample 1. But for sample 4, a larger ZOI of 21 nm was observed which can be attributed to the presence of UCNPs. To the best of our knowledge the anti-microbial properties of UCNPs has not been extensively studied, but this result suggests that they exhibit mild antimicrobial properties. In samples 5 and 6 the ZOIs were much larger (40 to 44 mm), suggesting effective hvL-PEG cleavage. These results offer evidence that the NIR irradiated samples will be useful antimicrobial fibers.

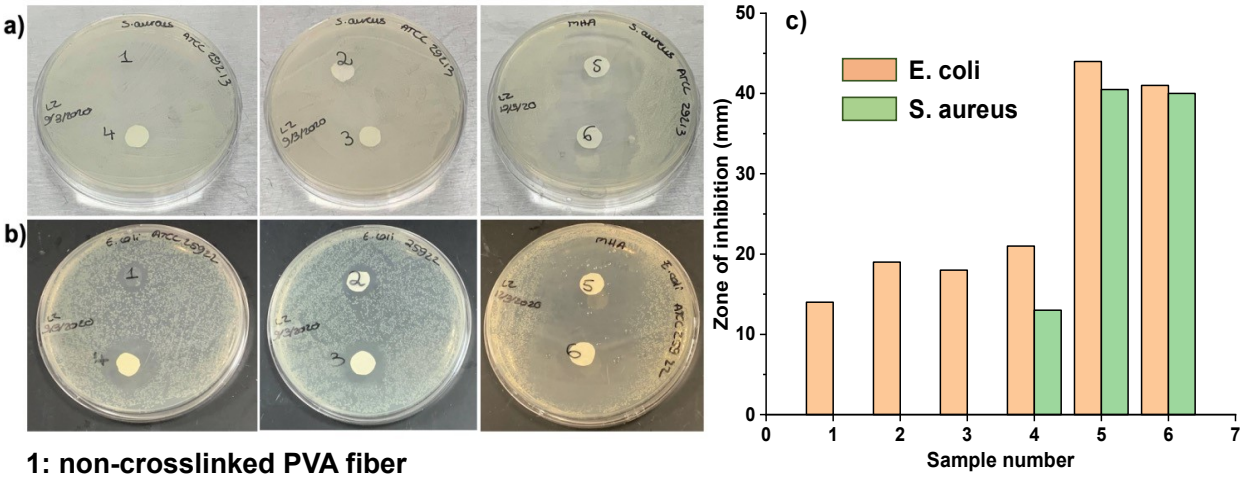

1: non-crosslinked PVA fiber
2: crosslinked PVA fiber
3: crosslinked drug conjugates in PVA fiber
4: crosslinked UCNP and drug conjugates in PVA fiber
5: crosslinked UCNP drug conjugates in PVA fiber pre-irradiated with 980 nm NIR for 1 hr
6: crosslinked UCNP drug conjugates in PVA fiber pre-irradiated with 980 nm NIR for 2 hrs

Figure 33. The digital images of a) *s. aureus* incubation disks with samples 1-6, (b) *e. coli* incubation disks with samples 1-6 and (c) the graph of ZOI *vs.* sample number.

Table 2. Disc diameter (nm) and ZOI (nm) of samples incubated with gram-negative *E-coli*.

Assay Number	Disc Diameter (mm)	Zone of Inhibition diameter (mm)
1	9	14
2	10	19
3	10	18
4	10	21
5	10	44
6	10	41

Table 3. Disc diameter (nm) and ZOI (nm) of samples incubated with gram-positive *S. Aureus*.

Assay Number	Disc Diameter (mm)	Zone of Inhibition diameter (mm)
1	9	0
2	10	0
3	10	0
4	10	13
5	10	40.5
6	10	40

Chapter 5 Conclusion and future possible directions

5.1 Summary

In this work, a NIR initiated drug delivery system based on electrospun nanofibers was developed using embedded light-sensitive polymer prodrugs and UCNPs. Polymer prodrugs were successfully synthesized and tested for drug release. The model antibiotic – levofloxacin, can be cleaved from the ONB group under the UV emission of UCNPs at 365 nm. The light-triggered release was monitored and there was no release on exposure to ambient light. The disk diffusion test demonstrated anti-microbial properties of the composite electrospun fiber mats against gram-positive and gram-negative bacteria. The controlled drug release, actualized through NIR irradiation, can potentially be extended to other drugs for controlled release and to prevent unfavorable side effects of using UV radiation.

Although this project is a proof-of-concept which set out to test the feasibility of this kind of drug delivery, there are some limitations of this system. The protocol described herein can only be used for drugs bearing -OH groups, which is required for conjugation to the photosensitive ONB polymer. Also, the system, as tested, displayed an abrupt drug release once it was irradiated with NIR light, which indicates that prolonged and sustained drug release was not achieved.

In future, first of all, ‘on’ and ‘off’ NIR radiation can be tried to probe if drug release can be toggled ‘on’ and ‘off’ – which would create an on-demand drug release system. Second, more investigations can be performed by varying the ratio of PMAO-UCNP colloids and hvL-PEG, for example, to see their effects on the drug release profile. Third, the intensity of NIR radiation can be varied to see if the rate of drug release can be modulated. Finally, cell viability tests should be performed since the effect of the sample on healthy cells is still an unknown.

5.2 Suggested direction 1 - Incorporation of sensors

Upconverting nanoparticles can be coupled to chemically sensitive dyes and quenchers.[118] This kind of coupling enables nanoscale measurements to prevent lysosomal degradation of the drug prior to reaching the desired site. The pH-sensitive molecules can absorb energy from the UV emissions of the UCNPs, they have negligible background fluorescence and high signal-to-noise

ratios. In our case, pH is a biomarker for chronic wounds as chronic wounds typically have an alkaline pH 8-9.[14] Tsai *et al.* found that in $NaYF_4:Yb^{3+}$, Er^{3+} nanocrystals change their luminescent wavelength when exposed to different pH (Figure 34).[118] UV-emitting nanocrystals may also have the ability to change luminescent wavelength when exposed to different pH conditions,[90] to regulate the intensity of UV emission and hence control the drug release profile, finally establishing an automated drug release system.

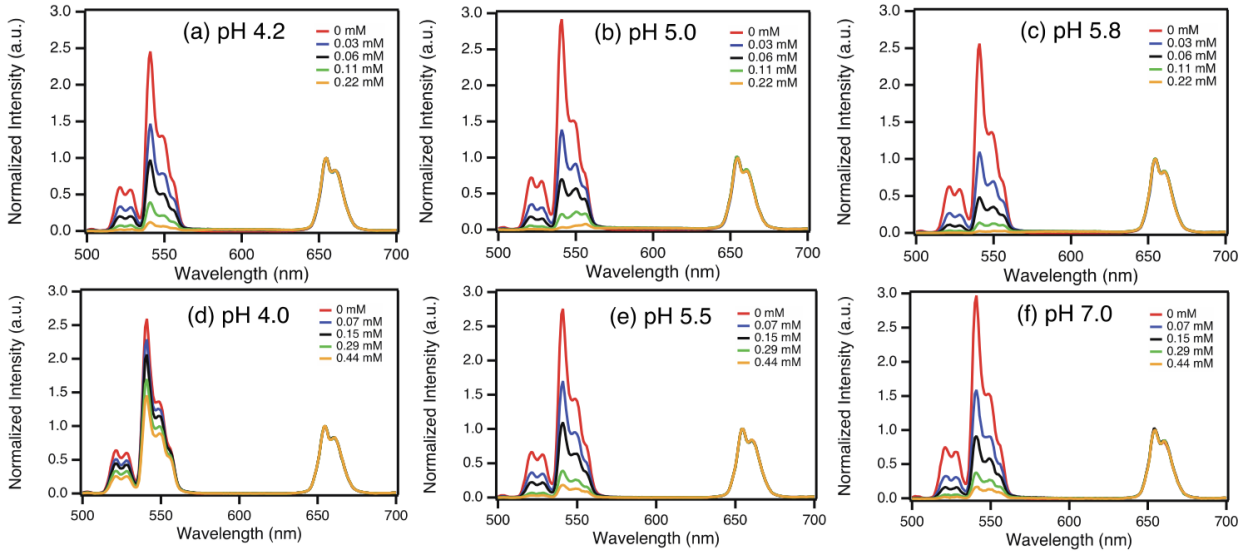

Figure 34. Effect of different amounts of calcium red on the emission spectra of UCNPs in phosphate/citrate buffer of different pH values.[118]

5.3 Suggested direction 2 - Other stimuli-responsive strategies for wound healing

Chronic wounds have complex microenvironments, where a single stimulus may not be enough to determine the proper time of drug delivery. In view of this, a more effective strategy, a dual or multi-stimuli responsive drug delivery system, can be envisioned.[119] A dual oxidation/pH trigger system for treating inflammations has been reported.[120] Nanoparticles made up of N-palmitoyl chitosan and poly-(1,4-phenyleneactone dimethylene thioketal) have been fabricated (Figure 35).[120] Curcumin was subsequently loaded onto the nanoparticles for treating inflammatory status. Upon the stimuli of oxidative stress and reduced pH, the thioketal linkages can be cleaved and the curcumin can then be released to counteract the overproduction of reactive oxygen species and reactive nitrogen species. Negligible chemiluminescence was identified at the

healthy tissues. This type of nanoparticles can be incorporated into advanced wound dressings that have excellent swelling properties to enhance healing.

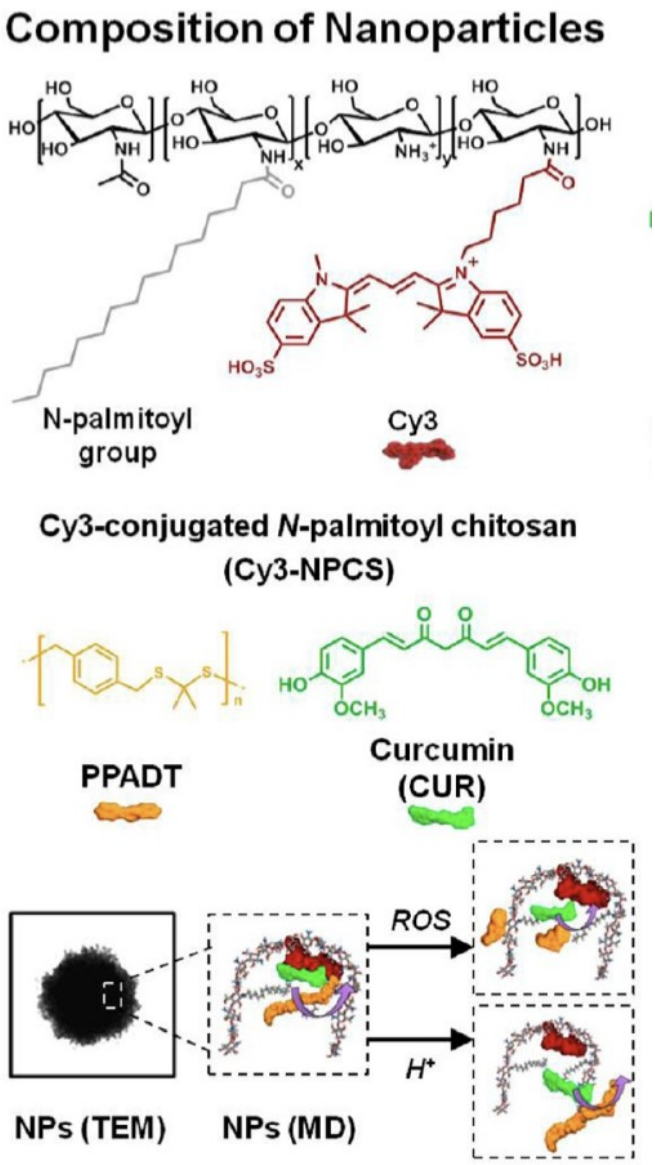

Figure 35. Schematic illustration showing the composition/structure of the dual-responsive nanoparticles developed.[120]

Focus on stimuli responsive materials is crucial for the development of a sustainable drug release system. Therefore, the pathology of chronic wounds needs to be better investigated to design enhanced therapeutic strategies. The technologies that have been developed in the last

decade, including the one described within this thesis, are expected to provide significant health benefits in the near future.

References

1. Gianino, E.; Miller, C.; Gilmore, J., Smart wound dressings for diabetic chronic wounds. *Bioengineering (Basel)* **2018,** *5* (3).
2. Abrigo, M.; McArthur, S. L.; Kingshott, P., Electrospun nanofibers as dressings for chronic wound care: advances, challenges, and future prospects. *Macromol. Biosci.* **2014,** *14* (6), 772-92.
3. Dhivya, S.; Padma, V. V.; Santhini, E., Wound dressings - a review. *Biomedicine* **2015,** *5* (4), 22.
4. Martinez, P. R.; Goyanes, A.; Basit, A. W.; Gaisford, S., Fabrication of drug-loaded hydrogels with stereolithographic 3D printing. *Int. J. Pharm.* **2017,** *532* (1), 313-317.
5. Smith, D. J., Use of biobrane in wound management. *J. Burn Care Res.* **1995,** *16* (3), 317-320.
6. Liu, Y.; Zhou, S.; Gao, Y.; Zhai, Y., Electrospun nanofibers as a wound dressing for treating diabetic foot ulcer. *Asian J. Pharm. Sci.* **2019,** *14* (2), 130-143.
7. Marin, S.; Albu Kaya, M. G.; Ghica, M. V.; Dinu-Pirvu, C.; Popa, L.; Udeanu, D. I.; Mihai, G.; Enachescu, M., Collagen-polyvinyl alcohol-indomethacin biohybrid matrices as wound dressings. *Pharmaceutics* **2018,** *10* (4).
8. Agarwal, S.; Greiner, A.; Wendorff, J. H., Functional materials by electrospinning of polymers. *Prog. Polym. Sci.* **2013,** *38* (6), 963-991.
9. Cui, Z.; Zheng, Z.; Lin, L.; Si, J.; Wang, Q.; Peng, X.; Chen, W., Electrospinning and crosslinking of polyvinyl alcohol/chitosan composite nanofiber for transdermal drug delivery. *Adv. Polym. Tech.* **2018,** *37* (6), 1917-1928.
10. Ko, S. W.; Lee, J. Y.; Lee, J.; Son, B. C.; Jang, S. R.; Aguilar, L. E.; Oh, Y. M.; Park, C. H.; Kim, C. S., Analysis of Drug Release Behavior Utilizing the Swelling Characteristics of Cellulosic Nanofibers. *Polymers* **2019,** *11* (9).
11. Sun, Y.; Cheng, S.; Lu, W.; Wang, Y.; Zhang, P.; Yao, Q., Electrospun fibers and their application in drug controlled release, biological dressings, tissue repair, and enzyme immobilization. *RSC Adv.* **2019,** *9* (44), 25712-25729.
12. Nasikhudin, M. D., A. Kusumaatmaja and K. Triyana, Stabilization of PVA:Chitosan:TiO2 nanofiber membrane with heat treatment and glutaraldehyde crosslink. *IOP Conf. Ser.: Mater. Sci. Eng. 367*
13. Li, C.; Fu, R.; Yu, C.; Li, Z.; Guan, H.; Hu, D.; Zhao, D.; Lu, L., Silver nanoparticle/chitosan oligosaccharide/poly(vinyl alcohol) nanofibers as wound dressings: a preclinical study. *Int. J. Nanomedicine* **2013,** *8*, 4131-45.
14. Derakhshandeh, H.; Kashaf, S. S.; Aghabaglou, F.; Ghanavati, I. O.; Tamayol, A., Smart bandages: the future of wound care. *Trends Biotechnol.* **2018,** *36* (12), 1259-1274.
15. Mura, S.; Nicolas, J.; Couvreur, P., Stimuli-responsive nanocarriers for drug delivery. *Nat. Mater.* **2013,** *12* (11), 991-1003.
16. Zhang, Y.; Riduan, S. N., Functional porous organic polymers for heterogeneous catalysis. *Chem. Soc. Rev.* **2012,** *41* (6), 2083-94.
17. Oh, J. K., Disassembly and tumor-targeting drug delivery of reduction-responsive degradable block copolymer nanoassemblies. *Polym. Chem.* **2019,** *10* (13), 1554-1568.
18. Sun, L.; Zhu, B.; Su, Y.; Dong, C.-M., Light-responsive linear-dendritic amphiphiles and their nanomedicines for NIR-triggered drug release. *Polym. Chem.* **2014,** *5* (5), 1605-1613.

19. Bertrand, O.; Gohy, J.-F., Photo-responsive polymers: synthesis and applications. *Polym. Chem.* **2017,** *8* (1), 52-73.
20. Zhao, Y., Light-responsive block copolymer micelles. *Macromolecules* **2012,** *45* (9), 3647-3657.
21. Liu, G.; Liu, W.; Dong, C.-M., UV- and NIR-responsive polymeric nanomedicines for on-demand drug delivery. *Polym. Chem.* **2013,** *4* (12).
22. Pang, Q.; Zheng, X.; Luo, Y.; Ma, L.; Gao, C., A photo-cleavable polyprodrug-loaded wound dressing with UV-responsive antibacterial property. *J. of Mater. Chem. B* **2017,** *5* (45), 8975-8982.
23. Zhao, H.; Sterner, E. S.; Coughlin, E. B.; Theato, P., O-nitrobenzyl alcohol derivatives: opprtunities in polymer and materials science. *Macromolecules* **2012,** *45* (4), 1723-1736.
24. Haase, M.; Schafer, H., Upconverting nanoparticles. *Angew Chem Int. Ed. Engl.* **2011,** *50* (26), 5808-29.
25. Chen, Z.; Chen, Z.; Zhang, A.; Hu, J.; Wang, X.; Yang, Z., Electrospun nanofibers for cancer diagnosis and therapy. *Biomater. Sci.* **2016,** *4* (6), 922-32.
26. Jiang, S.; Chen, Y.; Duan, G.; Mei, C.; Greiner, A.; Agarwal, S., Electrospun nanofiber reinforced composites: a review. *Polym. Chem.* **2018,** *9* (20), 2685-2720.
27. Cleeton, C.; Keirouz, A.; Chen, X.; Radacsi, N., Electrospun nanofibers for drug delivery and biosensing. *ACS Biomater. Sci. Eng.* **2019,** *5* (9), 4183-4205.
28. Shang, L.; Yu, Y.; Liu, Y.; Chen, Z.; Kong, T.; Zhao, Y., Spinning and applications of bioinspired fiber systems. *ACS Nano.* **2019,** *13* (3), 2749-2772.
29. V. Jones, J. E. G., K. G Harding, Wound dressings. *Br. Med.* **2006,** *332*, 777-780.
30. Guang Yang, J. W., Yi Wang, Long Li, Xing Guo, and Shaobing Zhou, An implantable active-targeting micelle-in-nanofiber device for efficient and safe cancer therapy. *ACS Nano.* **2015,** *9* (2), 1161-1174.
31. C. Weller, G. S., Wound dressings update. *Journal Pharm. Pract. Res.* **2006,** *36* (4), 318-324.
32. Skorkowska-Telichowska, K.; Czemplik, M.; Kulma, A.; Szopa, J., The local treatment and available dressings designed for chronic wounds. *J. Am. Acad. Dermatol.* **2013,** *68* (4), e117-e126.
33. Lionelli, G. T.; Lawrence, W. T., Wound dressings. *Surg. Clin. of North Am.* **2003,** *83* (3), 617-638.
34. Chen, J.; Zhang, S.; Sun, F.; Li, N.; Cui, K.; He, J.; Niu, D.; Li, Y., Multi-stimuli responsive supramolecular polymers and their electrospun nanofibers. *Polym. Chem.* **2016,** *7* (17), 2947-2954.
35. Osama Bshena, T. D. H., Leon MT Dicks & Bert Klumperman, Antimicrobial fibers-therapeutic possibilities and recent advances. *Future Med. Chem.* **2011,** *3* (14), 1821-1847.
36. Rajendran, N. K.; Kumar, S. S. D.; Houreld, N. N.; Abrahamse, H., A review on nanoparticle based treatment for wound healing. *J. Drug Deliv. Sci.Tec.* **2018,** *44*, 421-430.
37. Rujitanaroj, P.-O.; Pimpha, N.; Supaphol, P., Wound-dressing materials with antibacterial activity from electrospun gelatin fiber mats containing silver nanoparticles. *Polymer* **2008,** *49* (21), 4723-4732.
38. Kang, M.; Jung, R.; Kim, H. S.; Youk, J. H.; Jin, H. J., Silver nanoparticles incorporated electrospun silk fibers. *J. Nanosci. Nanotechnol.* **2007,** *7* (11), 3888-91.

39. Zhang, Y.; He, H.; Gao, W.-J.; Lu, S.-Y.; Liu, Y.; Gu, H.-Y., Rapid adhesion and proliferation of keratinocytes on the gold colloid/chitosan film scaffold. *Mat. Sci. Eng. C-Mater* **2009,** *29* (3), 908-912.
40. R. Sean Norman, J. W. S., Anand Gole, Catherine J. Murphy, and Tara L. Sabo-Attwood, Targeted photothermal lysis of the pathogenic bacteria, Pseudomonas aeruginosa, with gold nanorods. *Nano. Lett.* **2007,** *8* (1), 302-306.
41. Huang, Y.; Dan, N.; Dan, W.; Zhao, W.; Bai, Z.; Chen, Y.; Yang, C., Bilayered antimicrobial nanofiber membranes for wound dressings via in situ cross-linking polymerization and electrospinning. *Ind. Eng. Chem. Res.* **2018,** *57* (50), 17048-17057.
42. El-Refaie Kenawy, Y. R. A.-F., Antimicrobial properties of modified and electrospun poly(vinyl phenol). *Macromol. Biosci.* **2002,** *2*, 261-266.
43. Xu Li, Q.; Yao, F.; Yin, S.; Fu, G.-D.; Shen, L.; Nie, S.; Zhu, M., Antibacterial nanofibers of self-quaternized block copolymers of 4-vinyl pyridine and pentachlorophenyl acrylate. *High Perform. Polym.* **2009,** *22* (3), 359-376.
44. Guo, J.; Qin, J.; Ren, Y.; Wang, B.; Cui, H.; Ding, Y.; Mao, H.; Yan, F., Antibacterial activity of cationic polymers: side-chain or main-chain type? *Polym. Chem.* **2018,** *9* (37), 4611-4616.
45. Pascual, A.; Tan, J. P.; Yuen, A.; Chan, J. M.; Coady, D. J.; Mecerreyes, D.; Hedrick, J. L.; Yang, Y. Y.; Sardon, H., Broad-spectrum antimicrobial polycarbonate hydrogels with fast degradability. *Biomacromolecules* **2015,** *16* (4), 1169-78.
46. Li, P.; Li, X.; Saravanan, R.; Li, C. M.; Leong, S. S. J., Antimicrobial macromolecules: synthesis methods and future applications. *RSC Adv.* **2012,** *2* (10).
47. Song, Z.; Han, Z.; Lv, S.; Chen, C.; Chen, L.; Yin, L.; Cheng, J., Synthetic polypeptides: from polymer design to supramolecular assembly and biomedical application. *Chem. Soc. Rev.* **2017,** *46* (21), 6570-6599.
48. Kazemi Pilehrood, M.; Dilamian, M.; Mirian, M.; Sadeghi-Aliabadi, H.; Maleknia, L.; Nousiainen, P.; Harlin, A., Nanofibrous chitosan-polyethylene oxide engineered scaffolds: a comparative study between simulated structural characteristics and cells viability. *Biomed. Res. Int.* **2014,** *2014*, 438065.
49. Greiner, A.; Wendorff, J. H., Electrospinning: a fascinating method for the preparation of ultrathin fibers. *Angew Chem. Int. Ed.Engl.* **2007,** *46* (30), 5670-703.
50. S. Ramakrishna, K. F., W. Teo, T. Lim and Z. Ma An introduction to electrospinning and nanofibers. *World Scientific Publishing Co. Pte. Ltd.* **2005**.
51. Yang, G. Z.; Li, H. P.; Yang, J. H.; Wan, J.; Yu, D. G., Influence of working temperature on the formation of electrospun polymer nanofibers. *Nanoscale Res. Lett.* **2017,** *12* (1), 55.
52. Beachley, V.; Wen, X., Effect of electrospinning parameters on the nanofiber diameter and length. *Mater. Sci. Eng. C. Mater. Biol. Appl.* **2009,** *29* (3), 663-668.
53. Li, Z.; Wang, C., Effects of Working Parameters on Electrospinning. In *One-Dim. nanostructures*, 2013; pp 15-28.
54. Mit-uppatham, C.; Nithitanakul, M.; Supaphol, P., Ultrafine electrospun polyamide-6 fibers: effect of solution conditions on morphology and average fiber diameter. *Macromol. Chem. Phys.* **2004,** *205* (17), 2327-2338.
55. Hu, X.; Liu, S.; Zhou, G.; Huang, Y.; Xie, Z.; Jing, X., Electrospinning of polymeric nanofibers for drug delivery applications. *J. Control Release* **2014,** *185*, 12-21.

56. Yang, S.; Zhang, X.; Zhang, D., Electrospun chitosan/poly (vinyl alcohol)/graphene oxide nanofibrous membrane with ciprofloxacin antibiotic drug for potential wound dressing application. *Int. J. Mol. Sci.* **2019,** *20* (18).
57. Augustine, R.; Hasan, A.; Patan, N. K.; Dalvi, Y. B.; Varghese, R.; Antony, A.; Unni, R. N.; Sandhyarani, N.; Moustafa, A.-E. A., Cerium oxide nanoparticle incorporated rlectrospun poly(3-hydroxybutyrate-co-3-hydroxyvalerate) membranes for diabetic wound healing applications. *ACS Biomater. Sci. Eng.* **2019,** *6* (1), 58-70.
58. Z. Yuan, X. Z., X. Wang, W. Qiu, X. Chen, Q. Zheng, W. Cui, Promotion of initial anti-tumor effect via polydopamine modified doxorubicin-loaded electrospun fibrous membranes. *Int. J. Clin. Exp. Pathol.* **2014,** *7* (9), 5436-5449.
59. Salehi, R.; Irani, M.; Rashidi, M.-R.; Aroujalian, A.; Raisi, A.; Eskandani, M.; Haririan, I.; Davaran, S., Stimuli-responsive nanofibers prepared from poly(N-isopropylacrylamide-acrylamide-vinylpyrrolidone) by electrospinning as an anticancer drug delivery. *Des. Monomers Polym.* **2013,** *16* (6), 515-527.
60. Huang, Z.-M.; Zhang, Y. Z.; Kotaki, M.; Ramakrishna, S., A review on polymer nanofibers by electrospinning and their applications in nanocomposites. *Compo. Sci. Techno.* **2003,** *63* (15), 2223-2253.
61. Heidi Schreuder-Gibson, P. G., Kris Senecal, Michael Sennett, John Walker, Walter Yeomans, and David Ziegler, Protective Textile Materials Based on Electrospun Nanofibers. *J. Adv. Mater.* **2002,** *34* (3), 44-55.
62. Rachel A. Caruso, J. H. S., and Andreas Greiner, Titanium dioxide tubes from sol gel coating of electrospun Polymer fibers. *J. Adv. Mater.* **2001,** *13* (20), 1577-1579.
63. J. K. Li, N. W., X. S. Wu, Poly(vinyl alcohol) nanoparticles prepared by freezing–thawing process for protein:peptide drug delivery. *J. Control. Release* **1998,** *56*, 117-126.
64. Dong-Hwang Chen, J.-C. L., Ting-Chia; and; Huang, W., Transport and hydrolysis of urea in a reactor-separator combining an anion-exchange membrane immobilized urease. *J. Chem. Tech. Biotechnol.* **1994,** *61*, 351-357.
65. Hyon, S. H.; Cha, W. I.; Ikada, Y.; Kita, M.; Ogura, Y.; Honda, Y., Poly(vinyl alcohol) hydrogels as soft contact lens material. *J. Biomater.Sci. Polym. Ed.* **1994,** *5* (5), 397-406.
66. Jayakumar, R.; Prabaharan, M.; Sudheesh Kumar, P. T.; Nair, S. V.; Tamura, H., Biomaterials based on chitin and chitosan in wound dressing applications. *Biotechnol. Adv.* **2011,** *29* (3), 322-37.
67. Zhang, D.; Zhou, W.; Wei, B.; Wang, X.; Tang, R.; Nie, J.; Wang, J., Carboxyl-modified poly(vinyl alcohol)-crosslinked chitosan hydrogel films for potential wound dressing. *Carbohydr. Polym.* **2015,** *125*, 189-99.
68. Ignatova, M.; Manolova, N.; Rashkov, I., Novel antibacterial fibers of quaternized chitosan and poly(vinyl pyrrolidone) prepared by electrospinning. *Eur. Polym.* **2007,** *43* (4), 1112-1122.
69. Chase S. Linsley; Wu, B. M., Recent advances in light-responsive on demand drug-delivery systems. *Ther. Deliv.* **2017,** *8* (2), 89-107.
70. Badeau, B. A.; Comerford, M. P.; Arakawa, C. K.; Shadish, J. A.; DeForest, C. A., Engineered modular biomaterial logic gates for environmentally triggered therapeutic delivery. *Nat. Chem.* **2018,** *10* (3), 251-258.
71. Yuri V. Il'ichev, M. A. S. r., and Jakob Wirz, Photochemical reaction mechanisms of 2-nitrobenzyl compounds- methyl ethers and caged ATP. *J. Am. Chem. Soc.* **2004,** *126*, 4581-4595.

72. Pelliccioli, A. P.; Wirz, J., Photoremovable protecting groups: reaction mechanisms and applications. *Photochem. Photobiol. Sci.* **2002,** *1* (7), 441-58.
73. Wang, H.; Zhang, W.; Gao, C., Shape transformation of light-responsive pyrene-containing micelles and their influence on cytoviability. *Biomacromolecules* **2015,** *16* (8), 2276-81.
74. Timko, B. P.; Dvir, T.; Kohane, D. S., Remotely triggerable drug delivery systems. *Adv. Mater.* **2010,** *22* (44), 4925-43.
75. Yao, C.; Wang, P.; Li, X.; Hu, X.; Hou, J.; Wang, L.; Zhang, F., Near-infrared-triggered azobenzene-liposome/upconversion nanoparticle hybrid vesicles forremotely controlled drug delivery to overcome cancer multidrug resistance. *Adv. Mater.* **2016,** *28* (42), 9341-9348.
76. Alkilany, A. M.; Murphy, C. J., Toxicity and cellular uptake of gold nanoparticles: what we have learned so far? *J. Nanopart. Res.* **2010,** *12* (7), 2313-2333.
77. El-Sayed, S. L. M. A., Shape and size dependence of radiative, non-radiative and photothermal properties of gold nanocrystals. *Rev. Phys. Chem.* **2000,** *19* (3), 109-453.
78. Griffin, D. R.; Kasko, A. M., Photodegradable macromers and hydrogels for live cell encapsulation and release. *J. Am. Chem. Soc.* **2012,** *134* (31), 13103-7.
79. Choi, S. K.; Verma, M.; Silpe, J.; Moody, R. E.; Tang, K.; Hanson, J. J.; Baker, J. R., Jr., A photochemical approach for controlled drug release in targeted drug delivery. *Bioorg. Med. Chem.* **2012,** *20* (3), 1281-90.
80. Gwon, K.; Jo, E. J.; Sahu, A.; Lee, J. Y.; Kim, M. G.; Tae, G., Improved near infrared-mediated hydrogel formation using diacrylated Pluronic F127-coated upconversion nanoparticles. *Mater. Sci. Eng. C. Mater. Biol .Appl.* **2018,** *90*, 77-84.
81. Dong, H.; Du, S. R.; Zheng, X. Y.; Lyu, G. M.; Sun, L. D.; Li, L. D.; Zhang, P. Z.; Zhang, C.; Yan, C. H., Lanthanide nanoparticles: from design toward bioimaging and therapy. *Chem. Rev.* **2015,** *115* (19), 10725-815.
82. Wen, S.; Zhou, J.; Zheng, K.; Bednarkiewicz, A.; Liu, X.; Jin, D., Advances in highly doped upconversion nanoparticles. *Nat. Commun.* **2018,** *9* (1), 2415.
83. Joubert, M.-F., Photon avalanche upconversion in rare earth laser materials. *Opt.* **1999,** *11*, 181-203.
84. F., Z., Photon upconversion nanomaterial. *Springer* **2015**.
85. Naccache, R.; Yu, Q.; Capobianco, J. A., The fluoride host: nucleation, growth, and upconversion of lanthanide-doped nanoparticles. *Adv. Opt. Mater.* **2015,** *3* (4), 482-509.
86. Schladt, T. D.; Schneider, K.; Schild, H.; Tremel, W., Synthesis and bio-functionalization of magnetic nanoparticles for medical diagnosis and treatment. *Dalton. Trans.* **2011,** *40* (24), 6315-43.
87. D. V. Talapin, A. L. R., E. V. Shevchenko, A. Kornowski, M. Haase, and H. Weller, Dynamic distribution of growth rates within the ensembles of colloidal II-VI and III-V semiconductor nanocrystals as a factor governing their photoluminescence efficiency. *J. Am. Chem. Soc.* **2002,** *124*, 5782-5790.
88. Yin, Y.; Alivisatos, A. P., Colloidal nanocrystal synthesis and the organic-inorganic interface. *Nature* **2005,** *437* (7059), 664-70.
89. C. B. Murray, C. R. K. a. M. G. B., Synthesis and characterization of monodisperse nanocrystals and close-packed nanocrystal assemblies. *Annu. Rev. Mater. Sci.* **2000,** *30*, 545-610.
90. Park, Y. I.; Lee, K. T.; Suh, Y. D.; Hyeon, T., Upconverting nanoparticles: a versatile platform for wide-field two-photon microscopy and multi-modal in vivo imaging. *Chem. Soc. Rev.* **2015,** *44* (6), 1302-17.

91. Klier, D. T.; Kumke, M. U., Analysing the effect of the crystal structure on upconversion luminescence in Yb3+,Er3+-co-doped NaYF4 nanomaterials. *J. Mater. Chem. C* **2015,** *3* (42), 11228-11238.
92. Johnson, N. J.; He, S.; Diao, S.; Chan, E. M.; Dai, H.; Almutairi, A., Direct evidence for coupled surface and concentration quenching dynamics in lanthanide-doped nanocrystals. *J. Am. Chem. Soc.* **2017,** *139* (8), 3275-3282.
93. Auzel, F., Upconversion and Anti-Stokes Processes with f and d Ions in Solids. *Chem. Rev.* **2004,** *104*, 139-173.
94. Qian, H. S.; Zhang, Y., Synthesis of hexagonal-phase core-shell NaYF4 nanocrystals with tunable upconversion fluorescence. *Langmuir* **2008,** *24* (21), 12123-5.
95. Wang, Y.; Bao, L.; Liu, Z.; Pang, D. W., Aptamer biosensor based on fluorescence resonance energy transfer from upconverting phosphors to carbon nanoparticles for thrombin detection in human plasma. *Anal. Chem.* **2011,** *83* (21), 8130-7.
96. Wang, L.; Zhang, Y.; Zhu, Y., One-pot synthesis and strong near-infrared upconversion luminescence of poly(acrylic acid)-functionalized YF3:Yb3+/Er3+ nanocrystals. *Nano Res.* **2010,** *3* (5), 317-325.
97. Wilhelm, S.; Kaiser, M.; Wurth, C.; Heiland, J.; Carrillo-Carrion, C.; Muhr, V.; Wolfbeis, O. S.; Parak, W. J.; Resch-Genger, U.; Hirsch, T., Water dispersible upconverting nanoparticles: effects of surface modification on their luminescence and colloidal stability. *Nanoscale* **2015,** *7* (4), 1403-10.
98. Sedlmeier, A.; Gorris, H. H., Surface modification and characterization of photon-upconverting nanoparticles for bioanalytical applications. *Chem. Soc. Rev.* **2015,** *44* (6), 1526-60.
99. Dong, A.; Ye, X.; Chen, J.; Kang, Y.; Gordon, T.; Kikkawa, J. M.; Murray, C. B., A generalized ligand-exchange strategy enabling sequential surface functionalization of colloidal nanocrystals. *J. Am. Chem. Soc.* **2011,** *133* (4), 998-1006.
100. Zhang, Q.; Song, K.; Zhao, J.; Kong, X.; Sun, Y.; Liu, X.; Zhang, Y.; Zeng, Q.; Zhang, H., Hexanedioic acid mediated surface-ligand-exchange process for transferring NaYF4:Yb/Er (or Yb/Tm) up-converting nanoparticles from hydrophobic to hydrophilic. *J. Colloid Interface Sci.* **2009,** *336* (1), 171-5.
101. Wang, F.; Deng, R.; Wang, J.; Wang, Q.; Han, Y.; Zhu, H.; Chen, X.; Liu, X., Tuning upconversion through energy migration in core-shell nanoparticles. *Nat. Mater.* **2011,** *10* (12), 968-73.
102. Bogdan, N.; Vetrone, F.; Ozin, G. A.; Capobianco, J. A., Synthesis of ligand-free colloidally stable water dispersible brightly luminescent lanthanide-doped upconverting nanoparticles. *Nano. Lett.* **2011,** *11* (2), 835-40.
103. Xiang, J.; Ge, F.; Yu, B.; Yan, Q.; Shi, F.; Zhao, Y., Nanocomplexes of Photolabile Polyelectrolyte and Upconversion Nanoparticles for Near-Infrared Light-Triggered Payload Release. *ACS Appl. Mater. Interfaces* **2018,** *10* (24), 20790-20800.
104. Jalani, G.; Naccache, R.; Rosenzweig, D. H.; Haglund, L.; Vetrone, F.; Cerruti, M., Photocleavable hydrogel-coated upconverting nanoparticles: a multifunctional theranostic platform for NIR imaging and on-demand macromolecular delivery. *J. Am. Chem. Soc.* **2016,** *138* (3), 1078-83.
105. M., D.; Yu, Q.; Capobianco, J. A.; Hartman, M. C., Near infrared light mediated release of doxorubicin using upconversion nanoparticles. *Chem. Commun. (Camb.)* **2015,** *51* (40), 8477-9.

106. Schneider, C. A.; Rasband, W. S.; Eliceiri, K. W., NIH Image to ImageJ: 25 years of image analysis. *Nat. Methods* **2012,** *9* (7), 671-5.
107. Skripka, A.; Karabanovas, V.; Jarockyte, G.; Marin, R.; Tam, V.; Cerruti, M.; Rotomskis, R.; Vetrone, F., Decoupling Theranostics with Rare Earth Doped Nanoparticles. *Adv. Funct. Mater.* **2019,** *29* (12).
108. Destaye, A. G.; Lin, C. K.; Lee, C. K., Glutaraldehyde vapor cross-linked nanofibrous PVA mat with in situ formed silver nanoparticles. *ACS Appl. Mater. Interfaces* **2013,** *5* (11), 4745-52.
109. Li, Y.; Yao, S., High stability under extreme condition of the poly(vinyl alcohol) nanofibers crosslinked by glutaraldehyde in organic medium. *Polym. Degrad. Stabil.* **2017,** *137*, 229-237.
110. Wright, M. E.; Parrag, I. C.; Yang, M.; Santerre, J. P., Electrospun polyurethane nanofiber scaffolds with ciprofloxacin oligomer versus free ciprofloxacin: Effect on drug release and cell attachment. *J Control Release* **2017,** *250*, 107-115.
111. Chaney, S. B.; Ganesh, K.; Mathew-Steiner, S.; Stromberg, P.; Roy, S.; Sen, C. K.; Wozniak, D. J., Histopathological comparisons of Staphylococcus aureus and Pseudomonas aeruginosa experimental infected porcine burn wounds. *Wound Repair Regen* **2017,** *25* (3), 541-549.
112. Franklin R. Cockerill, M. A. W., Jeff Alder, Michael N. Dudley, George M. Eliopoulos, Mary Jane Ferraro, Dwight J. Hardy, David W. Hecht, Janet A. Hindler, Jean B. Patel, Mair Powell, ath Jana M. Swenson, Richard B. Thomson Jr., Maria M. Traczewski, John D. Turnidge, Melvin P. Weinstein, Barbara L. Zimmer, , Performance standards for antimicrobial disk susceptibility tests; approved standard—eleventh edition. *Clinical and Laboratory Standards Institute (CLSI).* **2012,** *32* (1).
113. Mahalingam, V.; Vetrone, F.; Naccache, R.; Speghini, A.; Capobianco, J. A., Colloidal Tm3+/Yb3+-doped LiYF4 nanocrystals: multiple luminescence spanning the UV to NIR regions via low-energy excitation. *Adv. Mater.* **2009,** *21* (40), 4025-4028.
114. Huang, W.; Lu, C.; Jiang, C.; Jin, J.; Ding, M.; Ni, Y.; Xu, Z., Rare earth doped LiYbF4 phosphors with controlled morphologies: Hydrothermal synthesis and luminescent properties. *Mater. Res. Bull.* **2012,** *47* (6), 1310-1315.
115. A. Braud, S. G., J. L. Doualan, M. Thuau, and R. Moncorge, Energy-transfer processes in Yb-Tm-doped KY3F10, LiYF4, and BaY2F8 single crystals for laser operation at 1.5 and 2.3 mm.pdf. *Am. Phys. Soc.* **2000,** *61* (8), 5280-5292.
116. Jiang, G.; Pichaandi, J.; Johnson, N. J.; Burke, R. D.; van Veggel, F. C., An effective polymer cross-linking strategy to obtain stable dispersions of upconverting NaYF4 nanoparticles in buffers and biological growth media for biolabeling applications. *Langmuir* **2012,** *28* (6), 3239-47.
117. Petkovsek, Z.; Elersic, K.; Gubina, M.; Zgur-Bertok, D.; Starcic Erjavec, M., Virulence potential of Escherichia coli isolates from skin and soft tissue infections. *J. Clin. Microbiol.* **2009,** *47* (6), 1811-7.
118. Tsai, E. S.; Himmelstoss, S. F.; Wiesholler, L. M.; Hirsch, T.; Hall, E. A. H., Upconversion nanoparticles for sensing pH. *Analyst* **2019,** *144* (18), 5547-5557.
119. Morey, M.; Pandit, A., Responsive triggering systems for delivery in chronic wound healing. *Adv. Drug Deliv. Rev.* **2018,** *129*, 169-193.

120. H. Pu, W. C., B. Maiti, Z. Liao, Y. Ho, M. S. Shim, E. Chuang, Y. Xia, and H. Sung, Nanoparticles with dual responses to oxidative stress and reduced pH for drug release and anti-inflammatory applications. *ACS Nano* **2014,** *8* (2), 1213-1221.
121. Jazani, A. M.; Arezi, N.; Maruya-Li, K.; Jung, S.; Oh, J. K., Facile Strategies to Synthesize Dual Location Dual Acidic pH/Reduction-Responsive Degradable Block Copolymers Bearing Acetal/Disulfide Block Junctions and Disulfide Pendants. *ACS Omega* **2018,** *3* (8), 8980-8991.
122. Jazani, A. M.; Oh, J. K., Dual Location, Dual Acidic pH/Reduction-Responsive Degradable Block Copolymer: Synthesis and Investigation of Ketal Linkage Instability under ATRP Conditions. *Macromolecules* **2017,** *50* (23), 9427-9436.

Appendix 1 Exploration of RAFT polymerization to synthesize block copolymers

A1.1. Introduction

Reversible addition fragmentation chain-transfer (RAFT) polymerization is a successful technique for controlled radical polymerization (CRP) that allows for the synthesis of well-controlled (co)polymers with various architectures, pre-determined molecular weight, and narrow molecular weight distribution. Furthermore, RAFT polymerization has been demonstrated to be a robust mean to synthesize block copolymers bearing multifunctionalities. My MSc research aimed to explore RAFT polymerization for several methacrylate monomers, including commercially-available 2-hydroxyethyl methacrylate (HEMA) and oligo(ethylene oxide) monomethyl ether methacrylate (OEOMA) as well as a synthesized HEMA conjugated with lipoic acid (HEMA-LA). As illustrated in Figure A1.1, a poly(ethylene glycol) (PEG)-based RAFT agent was synthesized and used for RAFT polymerization of three methacrylate monomers in an attempt to synthesize well-defined PEG-based block copolymers.

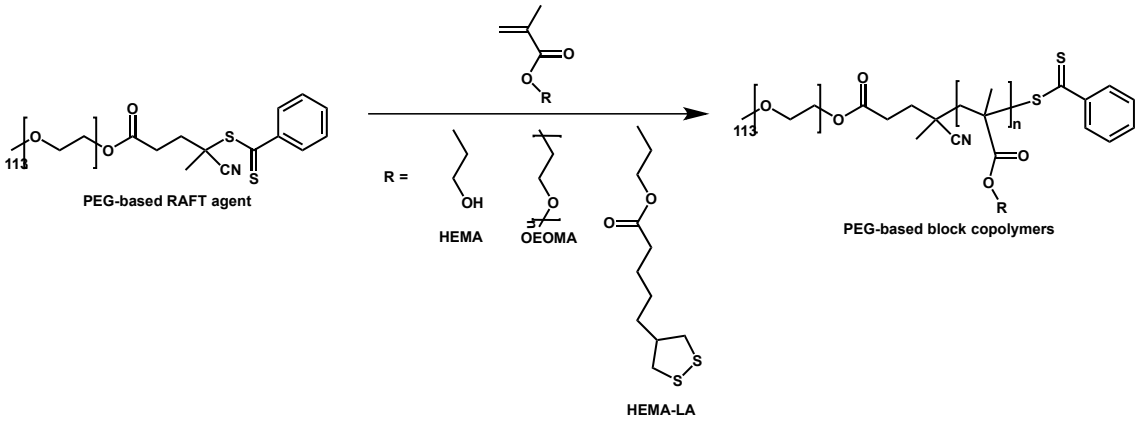

Figure A1.1. The reaction scheme of PEG-based RAFT agent reacting with the three methacrylate monomers to produce PEG-based block copolymers.

A1.2 Synthesis

Synthesis of HEMA-LA. An organic solution of lipoic acid (LA, 2.5 g, 12 mmol), HEMA (1.6 g, 12 mmol) and DMAP (0.7 g, 5.8 mmol) dissolved in chloroform (20 mL) was mixed with a solution of EDC (3.5 g, 18 mmol) in chloroform (10 mL) under stirring for 10 min in an ice-bath.

After being stirred 16 hrs at room temperature, the reaction mixture was washed with distilled water three times, and then dried over magnesium sulfate. After solvents were evaporated under vacuum by rotary evaporation, the product was precipitated from hexane (600 mL) and further dried in a vacuum oven set as room temperature for 16 hrs. ^{1}H NMR spectroscopy was used to confirm the structure of HEMA-LA (Figure A1.2).

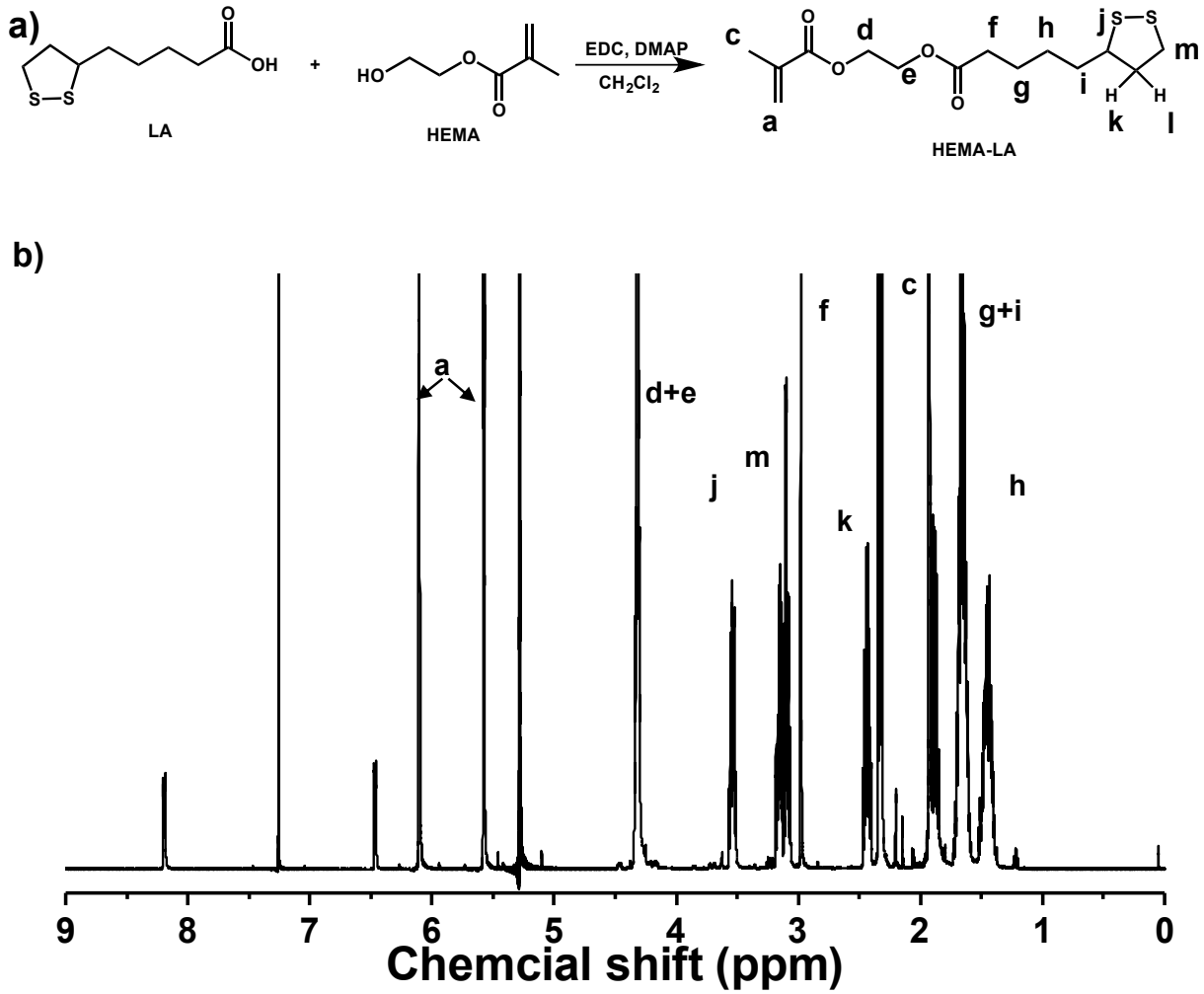

Figure A1.2. (a) Synthesis and (b) ^{1}H NMR spectrum in $CDCl_3$ of HEMA-LA.

Synthesis of a PEG-RAFT agent. An organic solution of PEG-OH (5 g, 1 mmol), DMAP (37 mg, 0.3 μmol), and 4-cyano-4-(phenylcarbonothioylthio)pentanoic acid (CPTP, 1.1 g, 4.0 mmol) dissolved in dichloromethane was mixed with EDC (0.8 g, 4.2 mmol) under stirring for 10 min in an ice-bath. After stirring for 16 hrs at room temperature, the reaction mixture was washed with deionized water three times, and then dried over magnesium sulfate. Solvents were

evaporated under vacuum by rotary evaporation. The product was precipitated from diethyl ether (600 mL) and further dried in a vacuum oven set at room temperature for 16 hrs. ^{1}H NMR spectroscopy was used to confirm the structure of PEG-RAFT (Figure A1.3).

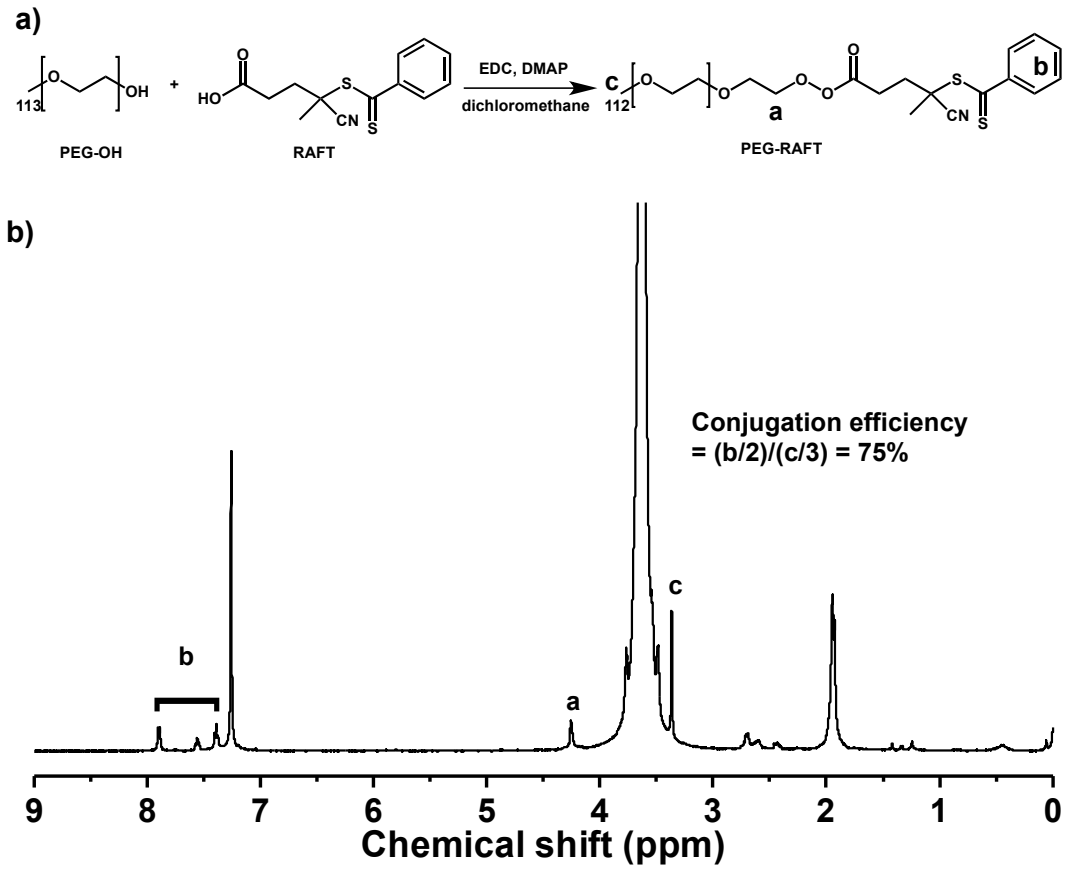

Figure A1.3. (a) Synthesis and (b) ^{1}H NMR spectroscopy in $CDCl_3$ of PEG-RAFT.

General procedure for RAFT block copolymerization of PEG-b-P(HEMA-LA). PEG-RAFT (0.3 g, 0.06 mmol), HEMA-LA (0.4 g, 3.7 mmol) and azobisisobutyronitrile (AIBN, 1.4 mg, 7.3 µmol) were dissolved in anisole (2 mL). The reaction mixture was heated at 70 °C in an oil-bath. The polymerization was stopped at two hrs. For purification, as-synthesized polymers were precipitated from hexane (600 mL) and dried in a vacuum oven set at room temperature for 16 hrs.[121]

A1.3 Results and discussion

Table A1.1 summarizes the characteristics and results of a series of block copolymers synthesized by RAFT polymerizations of HEMA as well as OEOMA and HEMA-LA.

Table A1.1. Characteristics and results of a series of block copolymers synthesized by RAFT polymerizations of HEMA as well as OEOMA and HEMA-LA.[a]

Monomer	HEMA-LA	OEOMA	HEMA
Polym time (day)	5	2	1
M_n (kg/mol)	No polymer	26.4	Gel
M_w/M_n		1.3	

a. Conditions for RAFT polymerization: $[M]_0/[PEG\text{-}RAFT]_0/[AMBN]_0 = 50/1/0.12$; M/anisole = 0.5/1 wt/wt, 70 °C.

Our experiment began with RAFT polymerization of HEMA-LA with initial mole ratio of $[HEMA\text{-}LA]_0/[PEG\text{-}RAFT]_0 = 50/1$ such that the degree of polymerization would be 50 at complete conversion. Under the conditions of $[AMBN]_0/[PEG\text{-}RAFT]_0 = 0.12/1$ and $[HEMA\text{-}LA]_0$/anisole = 0.5 wt/wt at 70°C, no polymerization was observed by the analysis of ^{1}H-NMR analysis. For HEMA, under the similar conditions, RAFT polymerization yielded a gel after 1 day. In contrast, the RAFT polymerization of OEOMA under similar conditions yielded well-defined PEG-b-POEOMA. Monomer conversion was determined to be 86% by ^{1}H-NMR and the molecular weight as the number average molecular weight (M_n) of the formed block copolymer was 26.4 kg/mol with a narrow molecular weight distribution as M_w/M_n of 1.3 by GPC analysis (Figure A1.4).

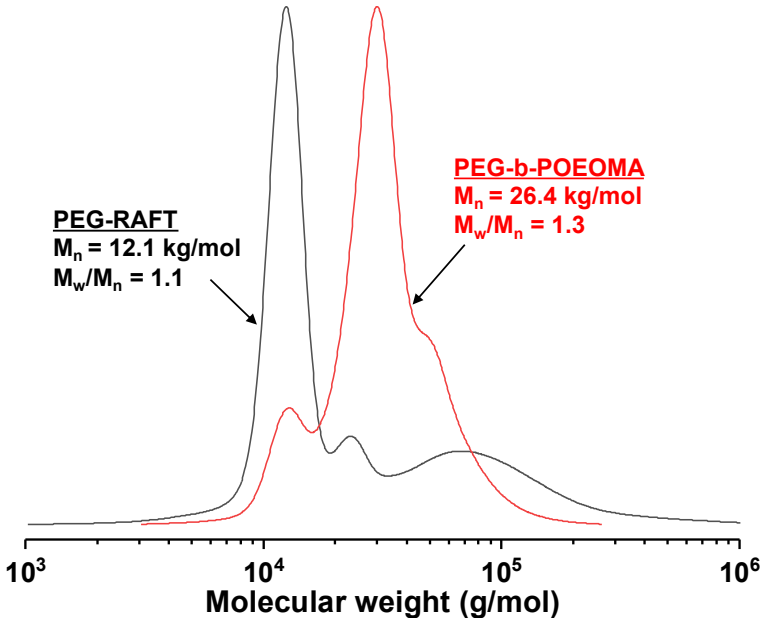

Figure A1.4. GPC plots of PEG-b-POEOMA compared with PEG-RAFT.

Appendix 2 Synthesis of multidentate block copolymer by ATRP

A2.1 Introduction

Atom transfer radical polymerization (ATRP) was examined to synthesize a double hydrophilic multidentate block copolymer (MDBC) consisting of PEG and poly(methacrylic acid) blocks, thus forming PEG-b-PMAA. Figure A2.1 depicts our synthetic approach.

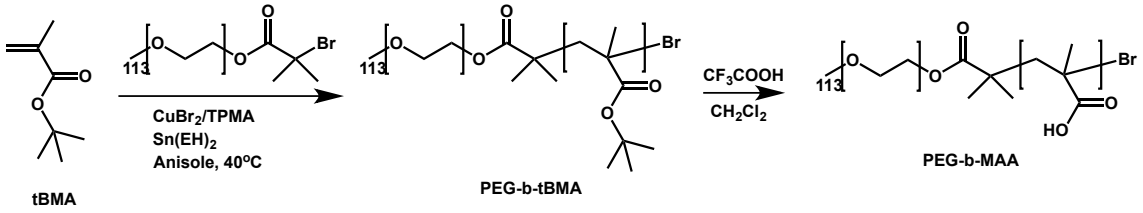

Figure A2.1. Our approach to synthesize well-defined PEG-b-PMMA, utilizing ATRP of tBMA in the presence of PEG-Br, followed by hydrolytic cleavage of the t-butyl group in the presence of trifluoroacetic acid.

A2.2 Synthesis of PEG-b-PMAA MDBC

For the synthesis of PEG-b-PtBMA, PEG-Br (2.5 g, 0.5 mmol), t-butyl methacrylate (tBMA) (3.4 g, 24 mmol), tris(2-pyridylmethyl)amine (TPMA, 21 mg, 72 μmol), [Cu(II)/TPMA-Br]Br (12 mg, 24 μmol) and anisole (1 mL) were mixed in an oil-bath at 45 °C and purged under nitrogen for 40 mins. A nitrogen-purged tin(II) ethylhexanoate ($Sn(II)(EH)_2$, 78 mg, 0.19 mmol) was then added to start the polymerization. After 2 hrs, the polymerization was stopped by exposing it to air. For purification, as-synthesized polymers were precipitated from hexane (600 mL) and dried in a vacuum oven set at room temperature for 16 hrs. In the next step, PEG-b-tBMA (1.9 g, 0.23 mmol) was mixed with trifluoroacetic acid (CF_3COOH, 5.4 g, 47 mmol) under stirring for 24 hrs. The polymer was precipitated from hexane (600 mL).[122]

A2.3 Results and discussion

ATRP of tBMA was conducted with an oxidatively-stable Cu(II)Br/TPMA complex under the initial mole ratio of $[tBMA]_o/[PEG\text{-}Br]_o/[CuBr_2\text{-}TPMA]_o/[TPMA]_o/[Sn(EH)_2]_o$ = 50/1/0.05/0.15. The polymerization was initiated with a PEG-Br macroinitiator to synthesize a

well-defined PEG-b-PtBMA block copolymer. After being purified by our standard methods[17], ^{1}H-NMR analysis showed the presence of PEG and PtBMA. The integral ratio with a DP = 113 of PEG block allowed for the determination of the DP of PtBMA block to be 29 (Figure A2.2). The purified block copolymer had a M_n = 11.6 kg/mol with M_w/M_n = 1.1 by GPC (Figure A2.3).

Next, the purified PEG-b-PtBMA was subjected to hydrolytic cleavage of the t-butoxy group in the presence of CF_3COOH. The complete cleavage was confirmed by ^{1}H NMR spectrometry (Figure A2.2.). The purified and dried PEG-b-PMAA was used for our investigation on surface modification of colloidal UCNPs in the next section.

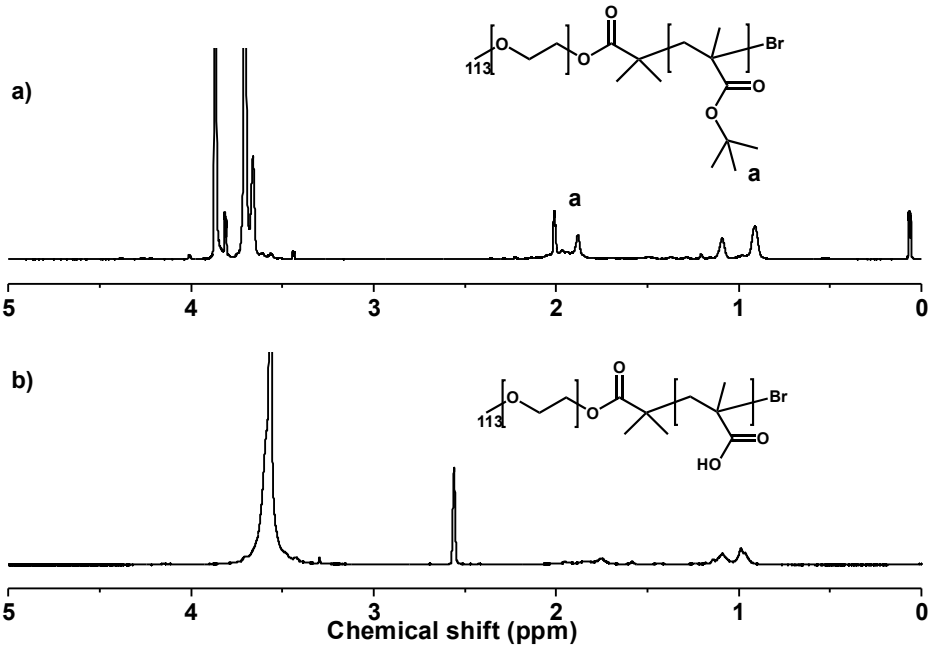

Figure A2.2. (a) ^{1}H-NMR spectra of PEG-PtBMA in $CDCl_3$ and (b) PEG-b-PMAA in DMSO-d_8.

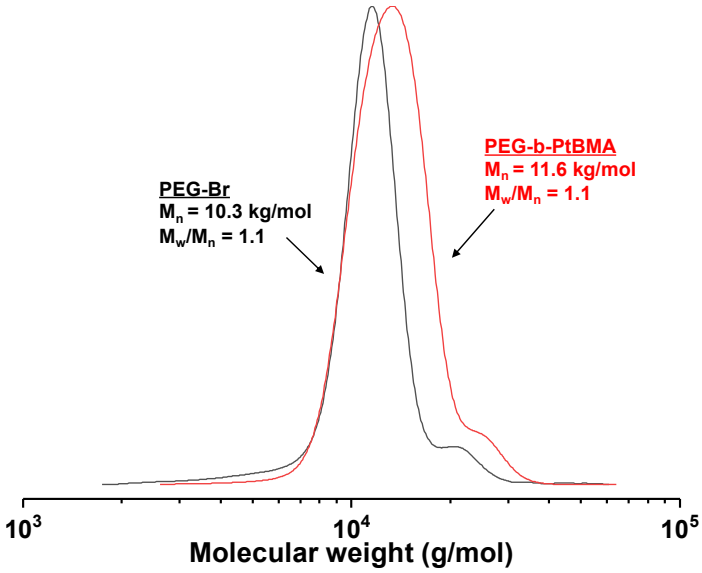

Figure A2.3. GPC diagram of PEG-PtBMA (red) compared with that of PEG-Br (black).

Appendix 3 Studies of ligand exchange of UCNPs

A3.1 Introduction

Colloidal UCNPs were synthesized in the presence of OA by the thermal decomposition method. The resultant OA-stabilized UCNPs (OA-UCNPs) have a hydrophobic surface, which is not compatible with an aqueous environment. The hydrophobic UCNP surface needs to be modified for the UCNPs to become water dispersible. Ligand exchange processes were investigated with a multidentate PEG-b-PMAA block copolymer and small molecule citric acid (Figure A3.1).

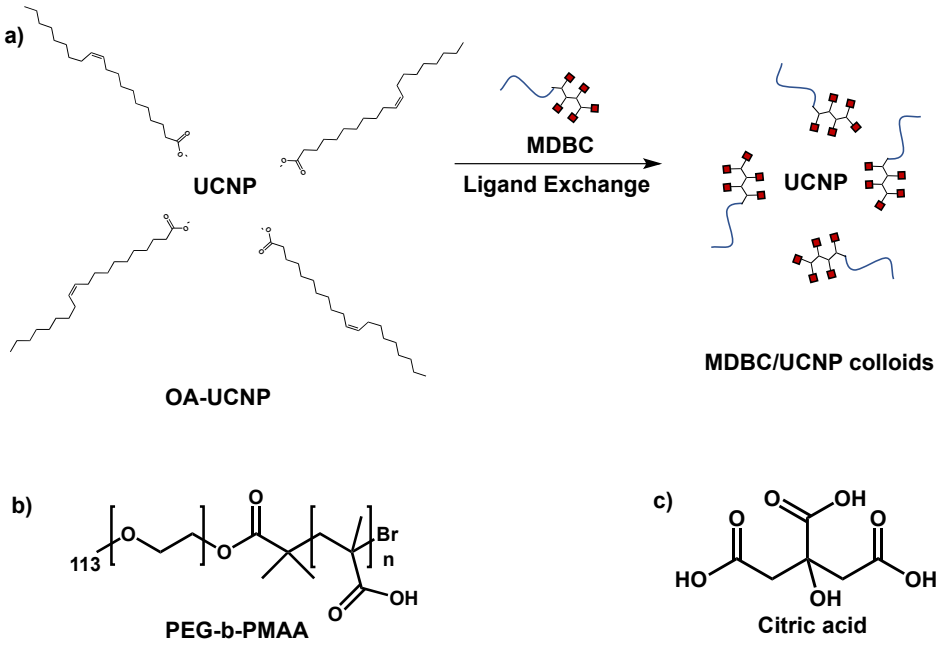

Figure A3.1. (a) Schematic illustration of ligand exchange of an OA-UCNP with MDBC to fabricate aqueous MDBC/UCNP colloids, (b) chemical structures of PEG-b-PMAA and (c) citric acid tridentate ligand.

A3.2 Experimental

A.3.2.1 Conventional ligand exchange with PEG-b-PMAA. An organic solution of OA-UCNPs (31.6 mg) in chloroform (2 mL) was mixed with the purified, dried PEG-b-PMAA (0.1 g) in a mixture of chloroform (4 mL) and ethanol (3 mL) under stirring for 16 hrs at room temperature. The resulting mixture was precipitated from hexane (600 mL). The precipitates were then

dispersed in chloroform and precipitated from hexane again. The procedure was repeated three times and the final precipitates were dispersed in water (5 mL) to form aqueous MDBC/UCNP colloidal solution at 5 mg/mL.

A.3.2.2 Biphasic ligand exchange with citric acid. An organic solution of OA-UCNP (50 mg) in hexane (25 mL) was mixed with an aqueous 0.2 M sodium citrate buffer solution (25 mL, pH = 3-4) under stirring for 3 hrs at room temperature. The aqueous bottom layer was separated, and the organic layer was washed with water. The aqueous solution was mixed with acetone (30 mL) and the resulting mixture was subjected to centrifuge (7000 rpm, 25 min, room temperature). The precipitate was dispersed in 0.2 M sodium citrate buffer solution (25 mL, pH 3-4) again and the purification process was repeated two more times. The final precipitates were dispersed in water to form aqueous citrate-stabilized UCNP colloids at 5 mg/mL.

A3.3 Results and discussion

Aqueous UCNP colloids stabilized with PEG-b-PMAA MDBC (MDBC/UCNP colloids) and small molecule citrate acid (citrate/UCNP colloids) were fabricated through ligand exchange processes with an organic OA-UCNP solution. They were characterized for size and morphology by TEM (Figure A3.2a-2b) and DLS (A3.2c-2d). For aqueous MDBC/UCNP colloids, TEM images showed that the colloidal nanoparticles appeared to be distinct with an average core size of 30 ± 2 nm. The DLS plots showed monomodal distribution with an average diameter of 118 nm, which is close to that of the original OA-UCNP colloids dispersed in hexane (136 nm). This result suggests no significant occurrence of aggregation during the conventional ligand exchange process with the MDBC. However, the DLS diameter was much larger than the TEM diameter, which could be attributed to undesired aggregation of OA-UCNPs during storage. Note that precipitates of MDBC/UCNP colloids were observed in a vial one day after fabrication.

In contrast, TEM images of citrate/UCNP colloids showed their existence as clusters. This could be due to the drying effect during TEM sample preparing. The DLS plots showed a monomodal distribution with an average diameter of 242 nm, which is close to that for OA-UCNP colloids dispersed in hexane (183 nm).

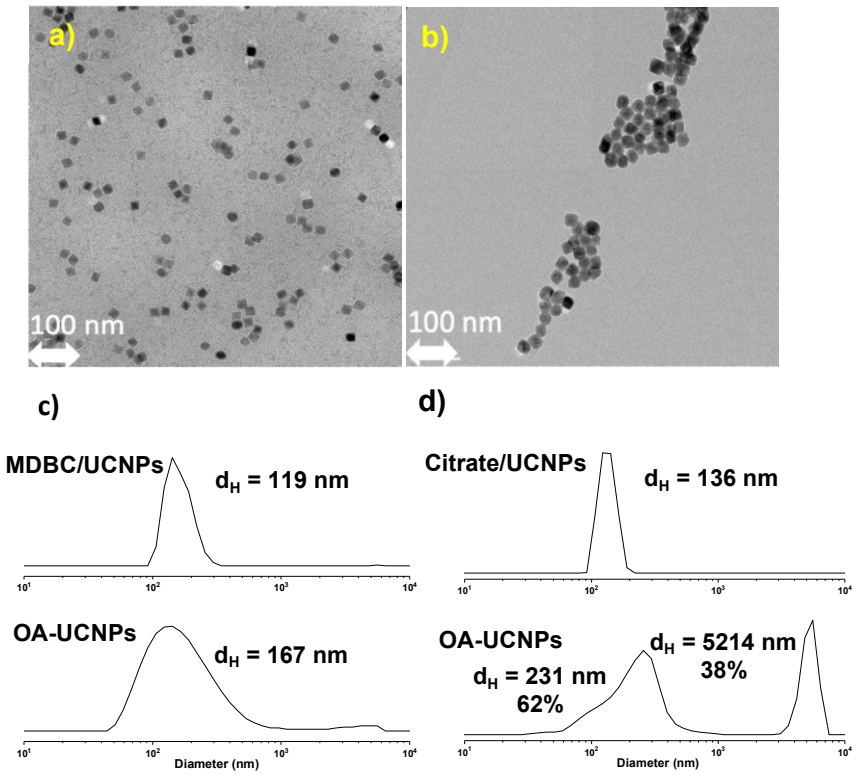

Figure A3.2. TEM images of aqueous (a) MDBC/USNP colloids and (b) citrate/UCNP colloids; (c & d) their DLS diagrams by volume compared with OA-UCNPs.